TIME-STABLE HIGH-ORDER FINITE DIFFERENCE METHODS FOR OVERSET GRIDS

BY

NEK SHARAN

DISSERTATION

Submitted in partial fulfillment of the requirements
for the degree of Doctor of Philosophy in Aerospace Engineering
in the Graduate College of the
University of Illinois at Urbana-Champaign, 2016

Urbana, Illinois

Doctoral Committee:

Associate Professor Daniel J. Bodony, Chair and Director of Research
Associate Professor Carlos A. Pantano-Rubino, Co-Chair and Co-Director of Research
Professor Paul F. Fischer
Assistant Professor Vincent Le Chenadec

Abstract

Overset grids provide an efficient and flexible framework for implementing high-order finite difference methods to simulate compressible viscous flows over complex geometries. Although overset methods have been widely used to solve time-dependent partial differential equations, very few proofs of stability exist for them. In practice, the interface treatments for overset grids are stabilized by adding numerical dissipation without any underlying theoretical analysis, impacting the accuracy and the conservation properties of the original method. In this work we discuss the construction of a provably time-stable and conservative method for solving hyperbolic problems on overset grids as well as their extension to solve the compressible Navier-Stokes equations. The proposed method uses interface treatments based on the simultaneous approximation term penalty method, and derivative approximations that satisfy the summation-by-parts property. Two cases of the method are analyzed. In the first case, no artificial dissipation is used and an eigenvalue analysis of the system matrix is performed to establish time-stability. The eigenvalue analysis approach for proving stability fails when the system matrix is not of a block triangular structure; therefore, we investigate the second case of the method where a localized numerical dissipation term is added to allow the use of energy method for stability proof. A framework for examining the conservation properties of the proposed method is discussed. Error analyses are performed to determine the order of interpolation that retains the accuracy of spatial finite difference operator.

The performance of the proposed method is assessed against the commonly used approach of injecting the interpolated data onto each grid. Several one-, two- and three-dimensional, linear and non-linear numerical examples are presented to confirm the stability and the accuracy of the methods. The extension of the method to solve the three-dimensional compressible Navier-Stokes equations on curvilinear grids is examined by performing a large-eddy simulation of flow over a cosine-shaped hill.

Acknowledgements

I must begin by thanking my advisors, Professor Daniel Bodony and Professor Carlos Pantano, for their support and patience in guiding me over the years. In addition to their advice on research, the multiple courses I took from them were extremely helpful at the beginning of my graduate studies. Their comments and feedback were pivotal to this work as well as my overall growth as a researcher. I am grateful to Professor Vincent Le Chenadec for an insightful course on Multiphase CFD and his interest in my work. I also thank Professor Paul Fischer for his comments on my thesis and presentation.

A special thanks to all my colleagues, Mahesh Natarajan, Qi Zhang, Wentao Zhang, Shakti Saurabh, Jaeseung Byun, Fabian Dettenrieder, Cory Mikida, Ramanathan Vishnampet, Nishanth Lingala, Sushil Koundinyan, Amal Sahai and Mohammad Mehrabadi, who were like family to me and have taught me a lot. Thanks are also due to Amit, Alok, Ankit and Purushotam for taking me on several trips around the US.

This work was supported by NASA through the Revolutionary Computational Aerosciences program within the Subsonic Fixed Wing project.

Last, but by no means least, I thank my parents for their unconditional love and support in any and everything I do. This thesis is dedicated to them.

Table of Contents

List of Figures

List of Abbreviations

IBVP	Initial Boundary Value Problem
ODE	Ordinary Differential Equation
PDE	Partial Differential Equation
SBP	Summation-by-Parts
SAT	Simultaneous Approximation Term
GKS	Gustafsson-Kreiss-Sundström
LES	Large-eddy Simulation
BC	Boundary Condition

Chapter 1

Introduction

The application of high-order finite difference methods for fluid flow computation over complex geometries usually requires a body-conforming curvilinear grid. It is, in general, difficult to create a single optimally-clustered grid with smooth variation and low cell skewness around a complicated shape. Multiblock grids, Figure 1.1 for example, offer an useful tool for mesh generation in such a case (see Flores & Chaderjian, 1990; Rizzi *et al.*, 1993). In the multiblock approach, the computational domain for a complex configuration is subdivided into several simple sub-domains or blocks on which mesh generation is straight-forward. The adjacent blocks in a multiblock grid share a common boundary, referred to as the interface, and the grid lines at the interface may or may not join together or have a common slope. A more flexible approach than using multiblock grids for mesh generation around complex geometries is the overset grid approach (see Benek *et al.*, 1985; Steger & Benek, 1987). Overset methods allow the individual grids to overlap as shown in Figure 1.2 and, unlike the multiblock methods, do not require the interfaces of the sub-domains to align with each other. It further simplifies the block shapes and potentially allows for a smoother body-fitted grid. Another advantage associated with the overset and the multiblock methods is that their block structure provides a default parallelism where each block could be assigned to a separate set of processors with data communication needed only to update the interface grid points.

Overset grids have been used for a variety of time-dependent fluid flow problems (see Prewitt *et al.*, 2000; Magnus & Yoshihara, 1970; Rai, 1987; Sengupta *et al.*, 2010) and aeroacoustic problems (see Bodony *et al.*, 2011; Kim *et al.*, 2010; Tam & Hu, 2004), among other applications. Several codes, for e.g. PEGSUS (see Suhs & Tramel, 1991; Rogers *et al.*, 2003), CMPGRD (see Brown *et al.*, 1989; Chesshire & Henshaw, 1990), DCF3D (see Meakin, 1991) etc. are available for assembling overset grids. Improvements with regards to hole-cutting, donor search algorithms, higher-order implementations have also received wide attention (see (see Petersson, 1999*a*,*b*; Sherer & Scott, 2005; Wang *et al.*, 2000) but the theoretical analysis for these methods still remain limited. Computational schemes for partial differential equations, in order to converge, should be consistent and stable. Moreover, for flows with discontinuous solutions, like shocks and slip surfaces, the method must be conservative in order to capture the correct strength and speed of propagation

of the discontinuities (Lax & Wendroff (1960)). Considerable literature exists on conservative interface treatments for overset grids (see Berger, 1987; Rai, 1986; Chesshire & Henshaw, 1994; Wang, 1995) but no such results exist for the stability of the methods. In most cases, the numerical instabilities due to the interface treatment are dealt with by adding artificial dissipation or using numerical filters in an *ad hoc* manner.

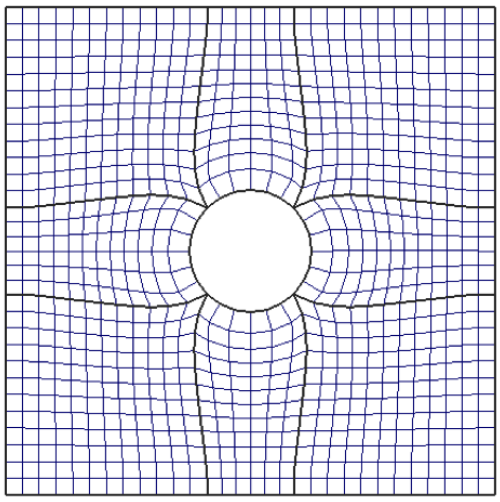

Figure 1.1: An example of multiblock grid (source: www.pointwise.com)

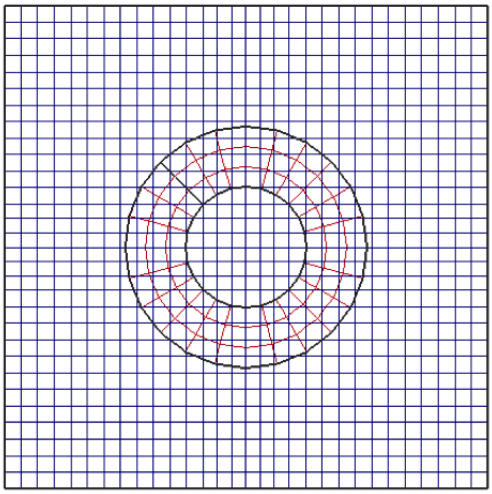

Figure 1.2: An example of overset grid (source: www.pointwise.com)

A common source of instability for the overset methods are the dispersive numerical waves that get trapped due to repeated reflections from one interface to another (Trefethen, 1985). If not dissipated, these waves grow with time and eventually corrupt the solution on the entire computational domain. It makes these methods unsuitable for simulations over long time durations, a common need in fluid dynamics. It also indicates the importance of assessing long-time behavior of the methods for overset grids. The classical definition of stability (Lax stability) allows a non-physical growth of solution in time as long as the growth diminishes with grid refinement (Trefethen, 1985) and, therefore, does not guarantee the desired long-time behavior. Time-stability, on the other hand, ensures a non-growing solution and provides a suitable criterion to evaluate the robustness of the overset methods.

The typical methods for studying stability of difference methods for initial boundary value problems (IBVPs) are the normal mode analysis, using the Laplace transform, and the energy method (see Gustafsson *et al.*, 1995). Each of the approaches have their advantages and limitations. We provide an overview of these methods in chapter 2. Normal mode analysis is a general method applicable to difference approximations but it can be algebraically challenging to show if the Godunov-Ryabenkii or the Kreiss condition is satisfied.

Several convenient stability criterions have been developed over the years (see for e.g. Goldberg & Tadmor, 1978, 1981, 1985, 1987) to simplify the analysis but still the application of these methods to analyze problems with complex grid configurations, such as the one dealt with in this thesis, remains challenging.

The energy method, on the other hand, is simpler to apply if one is able to construct a suitable scalar product and a norm that does not grow in time for the given problem. But the lack of a systematic procedure for finding the norm restricts the application of the method. The energy method is based on integration by parts and, therefore, only works for the problems with Hermitian (symmetric, if real) coefficient matrices. Fortunately, the coefficients of the Euler and the Navier-Stokes equations are simultaneously symmetrizable by a similarity transformation (see Abarbanel & Gottlieb, 1981), which makes them amenable to the energy method. We discuss in chapter 3 the summation by parts-simultaneous approximation term (SBP-SAT) methodology, which has been used to develop time-stable discretizations of IBVPs for the Euler and the Navier-Stokes equations (see Carpenter *et al.*, 1994; Svärd *et al.*, 2007).

As an example of using the Godunov-Ryabenkii condition for proving stability, Henshaw (2006) analyzed the interface conditions of a model problem for Maxwell's equation. Henshaw & Chand (2009) analyzed the interface conditions for the diffusion equation to model the fluid flow coupled with heat transfer in solids. Both references considered an overset grid with collocated grid points in the overlapping region. The Godunov-Ryabenkii condition provides a necessary but not sufficient condition of stability (see section 2.1.1). Moreover, the stability results for the simplified case of collocated grid points at the interface do not extend to the more general overset configuration with an arbitrary overlap. Reichert *et al.* (2012) used the SBP-SAT formalism with generalized SBP operators (Abarbanel & Chertock, 2000; Abarbanel *et al.*, 2000) to develop time-stable methods for hyperbolic problems on overset grids. Their proof of stability required the grid configurations to have interpolation donor points located at the end of the donor grid which restricts the amount of overlap and requires the length of the grid to be readjusted if the grid is refined. It becomes even more restrictive for solving a system of equations where multiple grids could act as donor grids. Moreover, the use of generalized SBP operator complicates the extension of the analysis to problems with diffusion. The present work tries to eliminate most of the limitations of the method in Reichert *et al.* (2012) by using SBP operators and a different approach to proving stability.

In this thesis we treat the difference approximations in semidiscrete form, also called as the method of lines, where the spatial derivatives are discretized to obtain a system of ODEs which are then advanced in time using a standard ODE integration method. Strikwerda (1980) outlined the necessary and sufficient conditions for stability of the semidiscrete approximation of IBVP analogous to the GKS theory for fully discrete case (Gustafsson *et al.*, 1972). Levy & Tadmor (1998) showed that for a well-posed spatially discretized system

of ODEs, $\mathbf{u}_t = M\mathbf{u}$ with $Re(M\mathbf{u}, \mathbf{u}) \leq 0$, the third and the fourth order Runge-Kutta methods for time integration retain the stability of the semidiscrete approximation if $Re(M\mathbf{u}, \mathbf{u}) \leq -\eta \|M\mathbf{u}\|^2$ for a fixed $\eta > 0$, where $(\cdot, \cdot)$ denotes an appropriate discrete inner product and $\|\cdot\|$ denotes the corresponding norm. Therefore, the semidiscrete analysis with the third or fourth order R-K method for the time integration can be used to study the stability of the fully discrete system. Numerical results in this thesis use the standard fourth-order Runge-Kutta method (RK4) for time integration (Butcher, 2008).

1.1 Thesis Structure

The thesis is organized as follows:

- *Chapter 2* describes different approaches of analyzing the numerical stability of difference methods and highlights the advantages and limitations of each. It also discusses the different definitions of stability.

- *Chapter 3* provides the basics of the SBP-SAT approach, the theoretical tool used to develop stable methods for overset grids. 1D and 2D single grid examples are presented to illustrate the method and how the proof of stability works for them. The sufficient conditions for time stability of a semidiscrete approximation are then discussed.

- *Chapter 4* presents the first case of the SBP-SAT-based overset method investigated. It is proven stable using an eigenvalue analysis. The shortcomings of the approach of eigenvalue analysis for stability proofs are highlighted. Numerical results are discussed for linear and non-linear problems. Error comparisons with the commonly used "injection method" of overset interface treatment are made to evaluate the performance of the SBP-SAT based method.

- *Chapter 5* examines the stability of the second case of the method where a localized numerical dissipation is introduced. The energy method is used to establish time-stability for all problems that have a bounded energy norm. The performance of the method is then evaluated against the first case of the method as well as the "injection method".

- *Chapter 6* discusses conservation for overset methods. The approach of imposing the interpolated data in SBP-SAT based method differs from the "injection method" in that only the downwind domain receives information from the other grid(s), based on the characteristic direction, as compared to a both-way exchange in the "injection method". It influences the quantity that ought to be conserved by the full computational domain. This chapter will derive the parameter values that make the method discussed in *Chapter 5* conservative.

- *Chapter 7* analyzes the stability of a SBP-SAT method for parabolic problems and provides the extension of the approach discussed in *Chapters 4-6* to solve the compressible Navier-Stokes equations on overlapping grids.

- *Chapter 8* provides the conclusions and suggestions for future work.

1.2 Accomplishments

Proving stability for overset methods offers a challenging problem and theoretical results on it are, therefore, scarce. To the best of our knowledge, none of the existing works address time-stability on overset grids with arbitrarily overlap. Moreover, stability with conservation for an overset method has not been previously analyzed. In light of this, the accomplishments of the dissertation could be summarized by the following:

1. High-order, provably time-stable overset grid methods have been developed for hyperbolic problems using the SBP-SAT approach. The proof of stability is provided for 1-D scalar and system of equations. The proof is general in that it poses no restrictions on the amount of overlap between the grids. The method is logically extended to two- and three-dimensions for overset grids with arbitrary overlap.

2. Long-time simulations were performed using the developed method to assess its behavior. It shows significantly better performance than the commonly used "injection method" of interface treatment. Inviscid simulations that require using numerical filters or artificial dissipation with "injection method" to run, can run indefinitely in a stable manner with the SBP-SAT based method.

3. A conservation analysis of the overlapping grids were performed to determine the values of the free parameters in the proposed method that ensure both time-stability and conservation. Closed form expressions of the parameters could be obtained for the second-order scheme but higher-order schemes require a case-by-case analysis for different grid overlaps due to algebraic complexity.

4. For application to the Navier-Stokes equation, the developed method for hyperbolic equations is supplemented with a viscous interface treatment analogous to that of the SBP-SAT based multiblock method discussed in Nordström *et al.* (2009). The combined method has been implemented in a parallel, three-dimensional compressible Navier-Stokes solver which was used to perform a large-eddy simulation of the flow over a hill, with a Reynolds number based on hill height of $500,000$.

Chapter 2

Analysis of Difference Methods

A numerical scheme for solving a partial differential equation (PDE) is useful only if its solution converges to the solution of the corresponding PDE in the limit of grid spacing and time step tending to zero. It is generally difficult to show convergence directly, therefore, the Lax-Richtmeyer equivalence theorem (Lax & Richtmyer, 1956) is used to show convergence from the consistency and stability of the method. We formally define these concepts below.

Consider the Cauchy problem for a linear scalar partial differential equation in one dimension

$$\begin{aligned} &\frac{\partial u}{\partial t} = A\left(x, t, \frac{\partial}{\partial x}\right) u, \qquad -\infty < x < \infty, \quad t \geq 0, \\ &u(x, 0) = f(x). \end{aligned} \tag{2.1}$$

$A\left(x, t, \dfrac{\partial}{\partial x}\right)$ is a differential operator of order q given by

$$A\left(x, t, \frac{\partial}{\partial x}\right) = \sum_{i \leq q} a_i(x, t) \frac{\partial^i}{\partial x^i}, \tag{2.2}$$

where i is a non-negative integer. We assume that the coefficient $a_i(x,t) \in C^\infty(x,t)$ and that the initial data $f(x)$ satisfies $\|f\|^2 = \int_{-\infty}^{\infty} |f|^2 \, dx < \infty$ and completely determines a unique solution. Let us define a discrete spatial domain $x_j = jh$ (where j is an arbitrary integer and grid spacing $h = \triangle x$) and temporal domain $t_n = n\triangle t$ (where n is a non-negative integer). We denote the approximate solution of problem (2.1) on the discrete domain by the grid function

$$\mathbf{v}(t_n) = [\ldots, v_{j-1}(t_n), v_j(t_n), v_{j+1}(t_n), \ldots]^T.$$

Using the method of lines (see Heath, 2001), the semidiscrete approximation to Eq. (2.1) is given by

$$\begin{aligned} &\frac{d\mathbf{v}}{dt} = M\mathbf{v}, \\ &\mathbf{v}(0) = \mathbf{f}(x), \end{aligned} \tag{2.3}$$

where M is a difference operator approximating $A\left(x, t, \frac{\partial}{\partial x}\right)$ and $\|\mathbf{f}\|_h = \sum_{j=-\infty}^{\infty} |f_j|^2 h < \infty$.

Definition 2.1 *The difference approximation in Eq. (2.3) is consistent with the differential equation (2.1) if there exists a constant K, independent of h, and $p > 0$ such that for all smooth functions $u(x,t)$,*

$$\|Au - Mu\|_h \leq Kh^p,$$

where $\|\,.\,\|_h$ denotes the discrete norm and p is the order of accuracy of difference operator M.

The definition of Lax stability is given by:

Definition 2.2 ***(Lax stability)*** *The approximation (2.3) is called stable (or Lax stable) if there are constants K and α, independent of h and f, such that*

$$\|\mathbf{v}\|_h \leq Ke^{\alpha t} \|\mathbf{f}\|_h . \tag{2.4}$$

The above definitions are important in the study of finite difference methods for initial value problems because of the Lax-Richtmeyer equivalence theorem, stated below without proof. The proof can be found in Lax & Richtmyer (1956) or Strikwerda (2004).

Theorem 2.1 (**The Lax-Richtmeyer Equivalence Theorem**) *A consistent finite difference scheme for a partial differential equation for which the initial value problem is well-posed is convergent if and only if it is stable.*

2.1 Stability of Finite Difference Methods for IBVPs

The first stability result in the form of Courant–Friedrichs–Lewy (CFL) condition was discussed in Courant *et al.* (1928), which stated that the domain of dependence of the difference method must contain the domain of dependence of the differential equation. It provides a necessary condition for stability. A few years later the von Neumann theory was developed based on Fourier analysis for periodic problems. Stability theories on difference methods for IBVPs started appearing in 1960s by the pioneering mathematicians at Moscow University and Uppsala University. We discuss, briefly, the relevant results from those theories below.

2.1.1 The Godunov-Ryabenkii Condition

First presented in Godunov & Ryabenkii (1963), the methodology treated the difference methods for an IBVP in a fully discrete form. Let us consider an IBVP for the partial differential equation in Eq. (2.1) with

constant coefficients, on the half line $\{0 \leq x < \infty\}$ with boundary condition at $x = 0$,

$$\begin{aligned} &\frac{\partial u}{\partial t} = A\left(\frac{\partial}{\partial x}\right) u, \qquad 0 \leq x < \infty, \quad t \geq 0, \\ &u(x,0) = f(x), \\ &B\left(\frac{\partial}{\partial x}\right) u(0,t) = g(t), \end{aligned} \tag{2.5}$$

where B is a differential operator of order $p < q$. Assuming a homogeneous boundary condition ($g(t) = 0$), the discretization using an explicit one-step method can be written as,

$$\mathbf{v}^{n+1} = Q_h \mathbf{v}^n, \qquad n = 0, 1, ... \tag{2.6}$$

where $\mathbf{v} = [v_0,\, v_1,\, v_2,\, \ldots]^T$. Godunov & Ryabenkii (1963) observed that the spectrum of the operator lying in the disk

$$|\lambda(Q_h)| < 1 + c\triangle t,$$

where c is a positive constant independent of h and $\triangle t$, provides a necessary condition for stability but not a sufficient condition. A series of observations led the authors to introduce a new concept of the spectrum of a family of operators $\{Q_h\}$ to determine a stricter stability criterion.

Definition 2.3 *A point λ is a spectral point of $\{Q_h\}$ if for any $\epsilon > 0$ and $h_0 > 0$, there exists a $h < h_0$ such that the inequality $\|Q_h u - \lambda u\| < \epsilon \|u\|$ has a solution u. The aggregate of all spectral points is called the spectrum of $\{Q_h\}$.*

The stability criterion, now called as the Godunov-Ryabenkii condition, was given by:

Theorem 2.2 *For the stability of a problem of the form (2.6) it is necessary that the spectrum of $\{Q_h\}$ should lie in the unit disc.*

The spectrum is usually determined from a normal mode analysis, based on the Laplace transform (see Gustafsson *et al.*, 1995). In engineering applications, it is common to first discretize the spatial derivatives to obtain a semidiscrete problem, also called as the method of lines, and then use standard ODE integration methods to advance in time. The semidiscrete approximation of the initial boundary value problem (2.5) is given by

$$\begin{aligned} &\frac{d\mathbf{v}}{dt} = M\mathbf{v}, \\ &\mathbf{v}(0) = \mathbf{f}(x), \\ &B_0\mathbf{v} = g(t), \end{aligned} \tag{2.7}$$

where M is a difference operator that approximates $A\left(\frac{\partial}{\partial x}\right)$, B_0 approximates $B\left(\frac{\partial}{\partial x}\right)$ and $\|\mathbf{f}\|_h < \infty$. Note that the first equation in (2.7) is used to advance the solution at all grid points except v_0, which is advanced using $B_0\mathbf{v} = g(t)$. Assuming $\mathbf{f} = \mathbf{0}$, the Laplace transformation of Eq. (2.7), with $\tilde{s} = sh$, yields the eigenvalue problem

$$\begin{aligned} \tilde{s}\hat{\mathbf{v}} &= hM\hat{\mathbf{v}}, \\ B_0\hat{\mathbf{v}} &= \hat{g}, \\ \|\hat{\mathbf{v}}\|_h &< \infty. \end{aligned} \tag{2.8}$$

For the homogeneous problem (Eq. (2.8) with $\hat{g} = 0$), the Godunov-Ryabenkii condition is satisfied if the problem has no eigenvalue $\tilde{s}$ with $Re\,\tilde{s} > 0$. For the non-homogeneous problem (2.8), the Godunov-Ryabenkii condition is satisfied if there is a unique solution for every fixed j that satisfies

$$|\hat{v}_j| \leq K(\tilde{s})|\hat{g}|, \tag{2.9}$$

for all $\tilde{s}$ with $Re\,\tilde{s} > 0$. The Godunov-Ryabenkii condition provides a necessary, but not sufficient, condition for stability since the constant K, in Eq. (2.9), is a function of $\tilde{s}$ and to ensure stability it must be shown to be bounded for all $\tilde{s}$ with $Re\,\tilde{s} \geq 0$. The Kreiss condition, given below, provides the sufficient conditions for stability.

2.1.2 The Kreiss Condition

The Kreiss condition is satisfied if there is a unique solution to problem (2.8) that for every fixed j satisfies

$$|\hat{v}_j| \leq K|\hat{g}|, \tag{2.10}$$

for all $\tilde{s}$ with $Re\,\tilde{s} > 0$, where K is independent of $\tilde{s}$. Using Parseval's relation, Eq. (2.10) leads to the estimate

$$\int_0^T |v_j(t)|^2\,dt \leq K_1 \int_0^T |g(t)|^2\,dt,$$

for any fixed j for a finite time T by integrating along the line $Re\,s = 0$. The Kreiss condition is satisfied for the homogeneous problem (Eq. (2.8) with $\hat{g} = 0$), if the problem has no eigenvalue or generalized eigenvalue $\tilde{s}$ with $Re\,\tilde{s} \geq 0$.

Definition 2.4 *If there exists a non-trivial solution* $\hat{\mathbf{v}}$*, for* $\tilde{s}_0$ *with* $Re(\tilde{s}_0) = 0$*, of problem (2.8) such that* $\|\hat{\mathbf{v}}\|_h = \infty$ *then* $\tilde{s}_0$ *is called the generalized eigenvalue of the problem.*

A connection between the Godunov-Ryabenkii condition and the Kreiss condition is discussed in Gustafsson (2001). The equivalent conditions that satisfy the Kreiss condition can be found in Gustafsson (2007). A numerical scheme that satisfies the Kreiss condition is, popularly, referred to as a G-K-S stable scheme.

2.1.3 The Energy Method

The energy method is based on constructing a norm, for the given problem, that does not grow in time (Kreiss, 1963; Richtmyer & Morton, 1994). We illustrate the method for the simple advection problem,

$$\begin{aligned} &\frac{\partial u}{\partial t} = \frac{\partial u}{\partial x}, \qquad 0 \le x \le 1, \quad t \ge 0, \\ &u(x,0) = f(x), \\ &u(1,t) = g(t). \end{aligned} \tag{2.11}$$

Assume a discrete domain $x_j = jh$, $j = 0, 1, \ldots, N$, with grid spacing $h = 1/N$. Let the semidiscrete approximation to (2.11) be given by

$$\begin{aligned} &\frac{dv_j}{dt} = \frac{v_{j+1} - v_{j-1}}{2h}, \qquad j = 1, 2, \ldots, N-1, \\ &\frac{dv_0}{dt} = \frac{v_1 - v_0}{h}, \\ &v_N(t) = g(t), \\ &v_j(0) = f_j, \qquad j = 0, 1, \ldots, N. \end{aligned} \tag{2.12}$$

Assuming $g = 0$ and denoting the solution vector as $\mathbf{v}(t) = [v_0(t), \ldots, v_{N-1}(t)]^T$, we get

$$\frac{d}{dt}\|\mathbf{v}\|_h^2 = \left(\mathbf{v}, \frac{d\mathbf{v}}{dt}\right)_h + \left(\frac{d\mathbf{v}}{dt}, \mathbf{v}\right)_h = v_0(v_1 - v_0) + \sum_{j=1}^{N-1} v_j(v_{j+1} - v_{j-1}) = -v_0^2 \le 0, \tag{2.13}$$

where the discrete scalar product and norm for the real-valued grid functions $\mathbf{v}$ and $\mathbf{w}$ are defined by

$$(\mathbf{v}, \mathbf{w})_h = \frac{h}{2} v_0 w_0 + \sum_{j=1}^{N-1} v_j w_j h, \qquad \|\mathbf{v}\|_h^2 = (\mathbf{v}, \mathbf{v})_h.$$

On integration (2.13) yields

$$\|\mathbf{v}(t)\|_h^2 \le \|\mathbf{f}\|_h^2, \tag{2.14}$$

which implies (2.12) is a stable approximation as discussed below.

Let us consider an IBVP for a linear system of partial differential equations given by

$$\begin{aligned} &\frac{\partial u}{\partial t} = A\left(\frac{\partial}{\partial x}\right) u + F(x,t), \qquad a \le x < b, \quad t \ge 0, \\ &u(x,0) = f(x), \\ &B\left(\frac{\partial}{\partial x}\right) u_B = g(t), \end{aligned} \tag{2.15}$$

where $u = [u^1(x,t),\ .....,\ u^r(x,t)]^T$, A is a $r \times r$ matrix of linear differential operators with constant coefficients and $B(\partial/\partial x)u_B = g(t)$ denotes the complete set of boundary conditions required for the PDE system to determine a unique solution. For example, if $A(\dfrac{\partial}{\partial x}) = \Lambda\dfrac{\partial}{\partial x}$ where $\Lambda = \text{diag}(\lambda_1,\ \lambda_2,\ ...,\ \lambda_k,\ \lambda_{k+1},\ .....,\ \lambda_r)$ such that

$$\lambda_1 < \lambda_2 < \ ... \ < \lambda_k < 0 < \lambda_{k+1} < \ ..... \ < \lambda_r,$$

then $B = I$, $u_B = [u^1(a,t),\ .....,\ u^k(a,t),\ u^{k+1}(b,t),\ .....,\ u^r(b,t)]^T$ and $g(t) = [g_1(t),\ .....,\ g_r(t)]^T$ provides a set of well-posed boundary conditions based on the characteristic direction. The norm of g, used in the following discussion, is then defined as

$$|g|^2 = \sum_{i=1}^{r} |g_i|^2 . \tag{2.16}$$

Consider a semidiscrete approximation to problem (2.15) of the form

$$\begin{aligned} &\frac{d\mathbf{v}}{dt} = M\mathbf{v} + \mathbf{F}(t), \\ &\mathbf{v}(0) = \mathbf{f}(x), \\ &B\mathbf{v}_B = \mathbf{g}(t). \end{aligned} \tag{2.17}$$

Definition 2.5 *The approximation (2.17) is stable (or Lax stable) if for* $\mathbf{F} = \mathbf{g} = \mathbf{0}$ *the solution* $\mathbf{v}(t)$ *satisfies*

$$\|\mathbf{v}\|_h \le Ke^{\alpha t} \|\mathbf{f}\|_h . \tag{2.18}$$

Since the estimate (2.14) satisfies (2.4), (2.12) is a stable approximation of (2.11).

Definition 2.6 *The approximation (2.17) is strongly stable if the solution* $\mathbf{v}(t)$ *satisfies*

$$\|\mathbf{v}(t)\|_h^2 \le Ke^{\alpha t}(\|\mathbf{f}\|_h^2 + \int_0^t (\|\mathbf{F}(\tau)\|_h^2 + |\mathbf{g}(\tau)|^2)d\tau), \tag{2.19}$$

where K and α are constants independent of h, $\mathbf{f}$, $\mathbf{g}$ and $\mathbf{F}$.

2.2 Time Stability

Attempts at developing stable boundary treatments for high-order finite difference schemes (Carpenter *et al.*, 1993), led to the observation that many of the schemes that were G-K-S stable showed exponential growth in error for long time integrations. It was also noted that although a G-K-S stable scheme ensures convergence to the exact solution in the limit $\triangle x \to 0$ for a fixed time, it does not exclude growth in time for a given grid size. This motivated the concept of time stability (also referred to as strict or asymptotic stability).

Definition 2.7 *The approximation (2.17) is time-stable if for $F = 0$ and $g = 0$ the solution $\mathbf{v}(t)$ satisfies*

$$\|\mathbf{v}\|_h \leq K \|\mathbf{f}\|_h , \tag{2.20}$$

where K is independent of h, $\mathbf{f}$ and t.

In contrast to Definition 2.5, the above definition bounds the solution uniformly in time. Analogous to Definition 2.6, strong stability in the context of time stability can defined as follows.

Definition 2.8 *The approximation (2.17) is strongly time-stable if the solution $\mathbf{v}(t)$ satisfies*

$$\|\mathbf{v}(t)\|_h^2 \leq K(\|\mathbf{f}\|_h^2 + \int_0^t (\|\mathbf{F}(\tau)\|_h^2 + |\mathbf{g}(\tau)|^2) d\tau), \tag{2.21}$$

where K is a constant independent of h, $\mathbf{f}$, $\mathbf{g}$, $\mathbf{F}$ and t.

Definition 2.9 *The approximation (2.17) is exponentially time-stable if for $F = 0$ and $g = 0$ there exist constants $\alpha > 0$ and K, independent of h, $\mathbf{f}$ and t, such that the solution $\mathbf{v}(t)$ satisfies*

$$\|\mathbf{v}\|_h \leq K e^{-\alpha t} \|\mathbf{f}\|_h . \tag{2.22}$$

In section 3.3, we discuss the sufficient conditions for time stability of a semidiscrete approximation.

Chapter 3

Derivative Approximation and Boundary Conditions

In this thesis, we use the summation-by-parts (SBP) approximation for $\frac{\partial}{\partial x}$. Kreiss & Scherer (1974) presented the method which was later used by Strand (1994) to construct the high-order spatial derivative approximations that satisfy the summation-by-parts property.

3.1 Summation-by-Parts (SBP)

Consider the problem (2.1) on $a \leq x \leq b$. The L_2-scalar product and norm are defined by

$$(u, v) = \int_a^b u^* v \, dx, \qquad (u, u) = \|u\|^2 . \tag{3.1}$$

The notation u^* denotes the complex conjugate of u. Using the above with integration by parts yields

$$\left(u, \frac{\partial u}{\partial x}\right) + \left(\frac{\partial u}{\partial x}, u\right) = u^2 \mid_a^b . \tag{3.2}$$

Let us consider a discrete domain $x_j = a + nh$, $h = (b-a)/N$, $n = \{0, 1, \ldots, N\}$. The discrete scalar product and norm for real-valued grid functions is given by

$$(\mathbf{u}, \mathbf{v})_h = \sum_{j=0}^{N} u_j v_j h, \qquad \|\mathbf{u}\|_h = \sqrt{(\mathbf{u}, \mathbf{u})_h}.$$

The SBP difference approximation D to $\partial/\partial x$ must satisfy

$$(\mathbf{u}, D\mathbf{u})_h + (D\mathbf{u}, \mathbf{u})_h = u_N^2 - u_0^2, \tag{3.3}$$

which is a discrete analogue to Eq. (3.2). Commonly the derivative operator is written as $D = P^{-1}Q$ so that

$$P\frac{\partial \mathbf{u}}{\partial x} = Q\mathbf{u},$$

denotes a compact approximation of the first spatial derivative. In this thesis, we work only with the explicit spatial derivative operators to ensure that the stability results are applicable to computation over curvilinear grids (see Svärd, 2004). For explicit operators, P is a diagonal positive definite matrix which allows the following definition of a discrete scalar product and norm,

$$(\mathbf{u}, \mathbf{v})_P = \mathbf{u}^T P \mathbf{v}, \qquad \|\mathbf{u}\|_P = \sqrt{(\mathbf{u}, \mathbf{u})_P}.$$

Using the above in Eq. (3.3) yields

$$(\mathbf{u}, P^{-1}Q\mathbf{u})_P + (P^{-1}Q\mathbf{u}, \mathbf{u})_P = \mathbf{u}^T(Q + Q^T)\mathbf{u}, \tag{3.4}$$

which requires $Q + Q^T = \text{diag}(-1, 0, \ldots., 1)$ to satisfy the SBP property (3.3).

3.2 Simultaneous Approximation Term (SAT)

For initial boundary value problems the SBP operators require a stable boundary treatment to ensure time stability. The SAT methodology has been widely used, with SBP operators, to prove time stability for problems on single grids (Carpenter *et al.*, 1994; Svärd *et al.*, 2007) as well as on multiblock grids (Carpenter *et al.*, 1999; Nordström & Carpenter, 1999; Nordström *et al.*, 2009; Kramer *et al.*, 2009). The SAT method imposes the physical boundary conditions weakly, as penalty terms added to the derivative operator. The penalty terms contain a free parameter whose value is adjusted to allow for a discrete energy estimate of the problem.

3.2.1 1D Example: The Advection Problem

Let us consider the right moving advection problem

$$\begin{aligned} &\frac{\partial u}{\partial t} + \frac{\partial u}{\partial x} = 0, \qquad 0 \le x \le 1, \quad t \ge 0, \\ &u(x, 0) = f(x), \\ &u(0, t) = g(t). \end{aligned} \tag{3.5}$$

The semidiscrete approximation using the SBP-SAT methodology, on a discrete domain $x_j = nh$, $h = 1/N$, $n = \{0, 1, \ldots, N\}$, is given by

$$\begin{aligned} &\frac{d\mathbf{u}}{dt} = -P^{-1}Q\mathbf{u} - \tau P^{-1}\mathbf{e}_0(u_0 - g(t)), \\ &\mathbf{u}(0) = \mathbf{f}(x), \\ &\mathbf{e}_0 = [1,\, 0,\, \ldots\, ,\, 0]^T, \end{aligned} \tag{3.6}$$

where $\mathbf{u}(t) = [u_0(t), \ldots, u_N(t)]^T$. The semi-discrete problem (3.6) has an energy estimate in the P-norm given by

$$\frac{d\|\mathbf{u}\|_P^2}{dt} = \left(\mathbf{u}, \frac{d\mathbf{u}}{dt}\right)_P + \left(\frac{d\mathbf{u}}{dt}, \mathbf{u}\right)_P = -\mathbf{u}^T(Q + Q^T)\mathbf{u} - 2\tau u_0^2 + 2\tau g(t)u_0 = (1 - 2\tau)u_0^2 - u_N^2 + 2\tau g(t)u_0.$$

If $g(t) = 0$ and $\tau \geq \frac{1}{2}$,

$$\frac{d\|\mathbf{u}\|_P^2}{dt} \leq 0 \Rightarrow \|\mathbf{u}\|_P \leq K\|\mathbf{f}\|_P,$$

which proves time stability (see Definition 2.5). For the case of non-zero boundary data we have

$$\frac{d\|\mathbf{u}\|_P^2}{dt} = (1 - 2\tau)u_0^2 - u_N^2 + 2\tau g(t)u_0 = \frac{\tau^2}{2\tau - 1}g(t)^2 - u_N^2 - (2\tau - 1)(u_0 - \frac{\tau}{2\tau - 1}g(t))^2.$$

If $\tau > \frac{1}{2}$,

$$\frac{d\|\mathbf{u}\|_P^2}{dt} \leq \frac{\tau^2}{2\tau - 1}g(t)^2,$$

which on integration yields

$$\|\mathbf{u}\|_P^2 \leq K\left(\|\mathbf{f}\|_P^2 + \int_0^t |g(\tau)|^2\, d\tau\right), \tag{3.7}$$

where $K = \max(1, \frac{\tau^2}{2\tau - 1})$. This proves that the method (3.6) is strongly time-stable (compare Eqs. (3.7) and (2.21)).

3.2.2 2D Example: The Euler Equations

The two-dimensional Euler equations, in conservative form, is given by

$$\frac{\partial Q}{\partial t} + \frac{\partial F}{\partial x} + \frac{\partial G}{\partial y} = 0, \tag{3.8}$$

where

$$Q = \begin{bmatrix} \rho \\ \rho u \\ \rho v \\ E \end{bmatrix}, \qquad F = \begin{bmatrix} \rho u \\ \rho u^2 + p \\ \rho uv \\ u(E+p) \end{bmatrix}, \qquad G = \begin{bmatrix} \rho v \\ \rho uv \\ \rho v^2 + P \\ v(E+p) \end{bmatrix},$$

$$E = \frac{p}{\gamma - 1} + \frac{1}{2}\rho(u^2 + v^2).$$

The proof of stability uses the result from Strang (1964) which shows that for a sufficiently smooth solution a consistent difference approximation for a non-linear partial differential equation converges if the linearized difference approximation is stable. Moreover, the use of energy method requires a set of linear equations with symmetric coefficient matrices. Therefore, we transform the Euler equations to primitive variables $V = [\rho, u, v, p]^T$, freeze the coefficient matrices (equivalent to linearizing about a uniform state) and then symmetrize them to obtain

$$\frac{\partial w}{\partial t} + A\frac{\partial w}{\partial x} + B\frac{\partial w}{\partial y} = 0. \tag{3.9}$$

w denotes the symmetrized variables given by

$$w = S_p^{-1} V = \begin{bmatrix} \frac{\bar{c}}{\bar{\rho}\sqrt{\bar{\gamma}}} & 0 & 0 & 0 \\ 0 & 1 & 0 & 0 \\ 0 & 0 & 1 & 0 \\ -\frac{\bar{c}}{\bar{\rho}\sqrt{\gamma(\gamma-1)}} & 0 & 0 & \sqrt{\frac{\gamma}{\gamma-1}}\frac{1}{\bar{\rho}\bar{c}} \end{bmatrix} \begin{bmatrix} \rho \\ u \\ v \\ p \end{bmatrix} = \begin{bmatrix} \frac{\bar{c}}{\bar{\rho}\sqrt{\bar{\gamma}}}\rho \\ u \\ v \\ -\frac{\bar{c}}{\bar{\rho}\sqrt{\gamma(\gamma-1)}}\rho + \sqrt{\frac{\gamma}{\gamma-1}}\frac{1}{\bar{\rho}\bar{c}}p \end{bmatrix},$$

where S_p is the "parabolic" symmetrizer matrix from Abarbanel & Gottlieb (1981), γ denotes the ratio of the specific heats (assumed to be a constant) and the quantities with overbar ($\bar{}$) indicate the frozen variables. A and B are real symmetric matrices, which can be diagonalized by orthogonal matrices. We denote the matrices T_x and T_y such that $A = T_x \Lambda_x T_x^{-1}$ and $B = T_y \Lambda_y T_y^{-1}$, and from the property of orthogonal matrices $T_x^{-1} = T_x^T$ and $T_y^{-1} = T_y^T$.

Let us consider an IBVP for the Euler equations (3.9) on the spatial domain $[0,1]\times[0,1]$ with initial condition $w(x,y,0) = f(x,y)$ and boundary conditions in terms of characteristic variables $C_x = T_x^T w$ and $C_y = T_y^T w$ given by

$$\frac{(|\Lambda_x| + \Lambda_x)}{2} C_x(x=0,y,t) = g_1(y,t), \qquad \frac{(|\Lambda_x| - \Lambda_x)}{2} C_x(x=1,y,t) = g_2(y,t), \tag{3.10}$$

$$\frac{(|\Lambda_y| + \Lambda_y)}{2} C_y(x,y=0,t) = g_3(x,t), \qquad \frac{(|\Lambda_y| - \Lambda_y)}{2} C_y(x,y=1,t) = g_4(x,t). \tag{3.11}$$

Numerical Discretization

Let us denote the solution field by w_{ijl} where the first two indices denote the x and y index of the grid point and the last index, ranging between 1 and 4, denotes the symmetrized variable. We assume $n_x + 1$ and $n_y + 1$ grid points in the x and y direction respectively therefore, the spatial indices i and j range from 0 to n_x and 0 to n_y, respectively. We define the vector $\mathbf{w} = (w_{001},\, w_{002},\, ...,\, w_{n_x n_y 4})^T$. The finite difference operators are given by

$$\mathbf{D_x} = D_x \otimes I_y \otimes I_4, \qquad \mathbf{D_y} = I_x \otimes D_y \otimes I_4,$$

where the matrix at the first position in the Kronecker product is of size $(n_x + 1) \times (n_x + 1)$, the one at the second position is of size $(n_y + 1) \times (n_y + 1)$ and the one at the third position is 4×4. I denotes an identity matrix with a size consistent with its position in the Kronecker product. D_x and D_y denote the first derivative approximation given by $P^{-1}Q$. We denote the norm matrices as

$$\mathbf{P}_x = P_x \otimes I_y \otimes I_4, \qquad \mathbf{P}_y = I_x \otimes P_y \otimes I_4, \qquad \mathbf{P} = \mathbf{P}_x\mathbf{P}_y,$$

and coefficient matrices as

$$\mathbf{A} = I_x \otimes I_y \otimes A, \qquad \mathbf{B} = I_x \otimes I_y \otimes B.$$

Moreover we define

$$\mathbf{E_{0x}} = E_0 \otimes I_y \otimes I_4, \qquad \mathbf{E_{nx}} = E_n \otimes I_y \otimes I_4,$$

$$\mathbf{E_{0y}} = I_x \otimes E_0 \otimes I_4, \qquad \mathbf{E_{ny}} = I_x \otimes E_n \otimes I_4,$$

where $E_0 = \mathrm{diag}(1,\, 0\,,\, ...\,,\, 0)$ and $E_n = \mathrm{diag}(0,\, ...\,,\, 0,\, 1)$ are of appropriate sizes based on their position in the Kronecker product.

The semidiscrete approximation to (3.9) using the SBP-SAT methodology, ignoring boundaries other than $x = 0$, is given by

$$\frac{d\mathbf{w}}{dt} = -\mathbf{A}\mathbf{D_x}\mathbf{w} - \mathbf{B}\mathbf{D_y}\mathbf{w} - \tau_1(\mathbf{P_x})^{-1}\mathbf{T_x}\mathbf{E_{0x}}(\mathbf{\Lambda_x^+}\mathbf{c_x} - \mathbf{g}_1), \tag{3.12}$$

where $\mathbf{c_x} = \mathbf{T_x^T}\mathbf{w}$ is the discrete analogue of C_x in Eq. (3.10) and

$$\mathbf{\Lambda_x^{\pm}} = \frac{|\mathbf{\Lambda_x}| \pm \mathbf{\Lambda_x}}{2}, \qquad \mathbf{\Lambda_x} = I_x \otimes I_y \otimes \Lambda_x, \qquad \mathbf{T_x} = I_x \otimes I_y \otimes T_x.$$

Assuming $\mathbf{g}_1 = 0$, pre-multiplying (3.12) by $\mathbf{w}^T\mathbf{P}$ and adding it to its transpose yields

$$\frac{d\left\|\mathbf{w}\right\|_{\mathbf{P}}^2}{dt} = -\mathbf{w}^T[\mathbf{PAD_x} + (\mathbf{PAD_x})^T]\mathbf{w} - \mathbf{w}^T[\mathbf{PBD_y} + (\mathbf{PBD_y})^T]\mathbf{w} - 2\tau_1\mathbf{w}^T\mathbf{P}_y\mathbf{T_x}\mathbf{E_{0x}}\mathbf{\Lambda}_\mathbf{x}^+\mathbf{c_x}. \tag{3.13}$$

Now,

$$\mathbf{PAD_x} = (P_x \otimes P_y \otimes I_4)(I_x \otimes I_y \otimes A)(P_x^{-1}Q_x \otimes I_y \otimes I_4) = (Q_x \otimes P_y \otimes A),$$

and since A and P_y are symmetric,

$$\mathbf{PAD_x} + (\mathbf{PAD_x})^T = (Q_x + Q_x^T) \otimes P_y \otimes A = -\mathbf{E_{0x}}\mathbf{P}_y\mathbf{A} + \mathbf{E_{nx}}\mathbf{P}_y\mathbf{A}, \tag{3.14}$$

and using $\mathbf{c_x} = \mathbf{T}_\mathbf{x}^T\mathbf{w}$,

$$2\tau_1\mathbf{w}^T\mathbf{P}_y\mathbf{T_x}\mathbf{E_{0x}}\mathbf{\Lambda}_\mathbf{x}^+\mathbf{c_x} = 2\tau_1\mathbf{w}^T\mathbf{E_{0x}}\mathbf{P}_y(\mathbf{T_x}\mathbf{\Lambda}_\mathbf{x}^+\mathbf{T}_\mathbf{x}^T)\mathbf{w}. \tag{3.15}$$

Substituting (3.14) and (3.15) in (3.13) after using $\mathbf{A} = \mathbf{T_x}\mathbf{\Lambda_x}\mathbf{T}_\mathbf{x}^T = \mathbf{T_x}(\mathbf{\Lambda}_\mathbf{x}^+ - \mathbf{\Lambda}_\mathbf{x}^-)\mathbf{T}_\mathbf{x}^T$ in (3.14) we get

$$\frac{d\left\|\mathbf{w}\right\|_{\mathbf{P}}^2}{dt} = (1-2\tau_1)\mathbf{w}^T\mathbf{E_{0x}}\mathbf{P}_y(\mathbf{T_x}\mathbf{\Lambda}_\mathbf{x}^+\mathbf{T}_\mathbf{x}^T)\mathbf{w} - \mathbf{w}^T\mathbf{E_{0x}}\mathbf{P}_y(\mathbf{T_x}\mathbf{\Lambda}_\mathbf{x}^-\mathbf{T}_\mathbf{x}^T)\mathbf{w} - \mathbf{w}^T\mathbf{E_{nx}}\mathbf{P}_y\mathbf{A}\mathbf{w} \tag{3.16}$$

$$-\mathbf{w}^T[\mathbf{PBD_y} + (\mathbf{PBD_y})^T]\mathbf{w},$$

which with the SAT implementation for other three boundaries yield $d\left\|\mathbf{w}\right\|_{\mathbf{P}}^2/dt \leq 0$ for the value of penalty parameter $\tau_1 \geq \frac{1}{2}$. Note that in Eq. (3.16), $\mathbf{w}^T\mathbf{E_{0x}}\mathbf{P}_y(\mathbf{T_x}\mathbf{\Lambda}_\mathbf{x}^-\mathbf{T}_\mathbf{x}^T)\mathbf{w} \geq 0$ so it has a non-positive contribution.

3.3 Proving Time Stability

The semidiscrete approximation to the general problem (2.15) can be written as

$$\begin{aligned} \frac{d\mathbf{v}}{dt} &= M\mathbf{v} + \mathbf{b}, \\ \mathbf{v}(0) &= \mathbf{f}(x), \end{aligned} \tag{3.17}$$

where $\mathbf{b}$ contains all the boundary data and the forcing function. With SAT boundary condition implementation, the solution vector $\mathbf{v}$ in Eq. (3.17) comprises solution values at all grid points (even the ones where physical boundary condition is imposed) as shown in the previous section. For methods, which impose the boundary condition strongly, Eq. (3.17) denotes the reduced set of equations obtained by substituting the physical boundary condition at the appropriate grid location.

We discuss below some sufficient conditions for time stability that will be used in chapters *4* and *5* to assess the stability of overset methods (see Antsaklis & Michel, 2006, 2007, for more details). For proving time stability of (3.17) it is sufficient to consider the case with $\mathbf{b} = \mathbf{0}$.

Lemma 3.1 *The approximation (3.17) is time-stable if there exists a real, symmetric and positive definite matrix H such that the matrix $L = M^T H + HM$ is negative semidefinite.*

Proof. Let the the solution of (3.17), with $\mathbf{b} = \mathbf{0}$, at time $t \geq 0$ be given by $\mathbf{v}(t)$, then

$$\int_0^t \frac{d}{d\tau}[\mathbf{v}(\tau)^T H \mathbf{v}(\tau)] d\tau = \mathbf{v}(t)^T H \mathbf{v}(t) - \mathbf{v}(0)^T H \mathbf{v}(0). \tag{3.18}$$

Using $\frac{d\mathbf{v}}{dt} = M\mathbf{v}$ and that the matrix L is negative semidefinite we have,

$$\frac{d}{d\tau}[\mathbf{v}(\tau)^T H \mathbf{v}(\tau)] = (\frac{d\mathbf{v}}{d\tau})^T H \mathbf{v} + \mathbf{v}^T H (\frac{d\mathbf{v}}{d\tau}) = \mathbf{v}^T (M^T H + HM)\mathbf{v} = \mathbf{v}^T L \mathbf{v} \leq 0. \tag{3.19}$$

Using (3.19) in (3.18) we get,

$$\mathbf{v}(t)^T H \mathbf{v}(t) \leq \mathbf{v}(0)^T H \mathbf{v}(0),$$

for all $t \geq 0$. Using the equivalence of norms and that H is positive definite we get

$$c_1 \|\mathbf{v}\|_h^2 \leq \|\mathbf{v}\|_H^2 = \mathbf{v}(t)^T H \mathbf{v}(t) \leq \mathbf{v}(0)^T H \mathbf{v}(0) = \|\mathbf{f}\|_H^2 \leq c_2 \|\mathbf{f}\|_h^2 , \tag{3.20}$$

where c_1 and c_2 are constants independent of h. Eq. (3.20) implies

$$\|\mathbf{v}\|_h \leq \sqrt{\frac{c_2}{c_1}} \|\mathbf{f}\|_h , \qquad \text{for all } t \geq 0.$$

Therefore, the approximation (3.17) is time-stable as per Definition 2.7.

Lemma 3.2 *Using a similarity transformation the matrix M could be taken to a Jordan canonical form $J = S^{-1}MS$, so that the change of variable $\mathbf{w} = S^{-1}\mathbf{v}$ transforms Eq. (3.17) to*

$$\begin{aligned} \frac{d\mathbf{w}}{dt} &= J\mathbf{w}, \\ \mathbf{w}(0) &= S^{-1}\mathbf{f}(x). \end{aligned} \tag{3.21}$$

The problem (3.17) is time-stable if and only if the problem (3.21) is time-stable.

Proof. If the problem (3.21) is time-stable then from Definition 2.7,

$$\|\mathbf{w}(t)\|_h \leq K_1 \|\mathbf{w}(0)\|_h ,$$

where K_1 is a constant independent of h, $\mathbf{w}(0)$ and t. For a given matrix M, S is a constant matrix therefore

$$\|S\|_h \|\mathbf{w}(t)\|_h \leq K_1 \|S\|_h \|\mathbf{w}(0)\|_h ,$$

where $\|S\|_h$ denotes a matrix norm defined as $\|S\|_h = sup\{\|S\mathbf{x}\|_h : \|\mathbf{x}\|_h = 1\}$. The inequality $\|S\mathbf{w}\|_h \leq \|S\|_h \|\mathbf{w}\|_h$, with $\mathbf{w} = S^{-1}\mathbf{v}$ yields,

$$\|\mathbf{v}(t)\|_h \leq K_1 \|S\|_h \left\|S^{-1}\right\|_h \|\mathbf{v}(0)\|_h .$$

Since S is a constant matrix we have

$$\|\mathbf{v}(t)\|_h \leq K \|\mathbf{f}(x)\|_h ,$$

where constant $K = K_1 \|S\|_h \left\|S^{-1}\right\|_h$ is independent of h, $\mathbf{f}$ and t. We have demonstrated that if problem (3.21) is time-stable then so is problem (3.17). A similar analysis can be used to show the opposite, i.e., the time stability of problem (3.17) implies the time stability of (3.21).

Lemma 3.3 *The approximation (3.17) is time-stable if and only if all eigenvalues of M have nonpositive real parts, and the geometric multiplicity of every eigenvalue with zero real part is equal to its algebraic multiplicity.*

Proof. Assume M in Eq. (3.17) is of size $m \times m$. The solution to Eq. (3.17) is given by $\mathbf{v}(t) = e^{Mt}\mathbf{v}(0)$ where

$$e^{Mt} = I + \sum_{k=1}^{\infty} \frac{t^k}{k!} M^k. \tag{3.22}$$

The solution to (3.21) is given by

$$\mathbf{w}(t) = e^{Jt}\mathbf{w}(0) \tag{3.23}$$

and therefore $\mathbf{v}(t) = Se^{Jt}S^{-1}\mathbf{v}(0)$. Two cases need to be evaluated to understand the stability of this solution:

Case I - M has m linearly independent eigenvectors: In this case the matrix J will be diagonal with eigenvalues of M as the diagonal elements i.e. $J = \text{diag}(\lambda_1, \ldots, \lambda_m)$. The eigenvectors of M will form the

columns of S. The matrix exponential, using (3.22), is given by

$$e^{Jt} = \begin{bmatrix} e^{\lambda_1 t} & & & \\ & \ddots & & \\ & & \ddots & \\ & & & e^{\lambda_m t} \end{bmatrix}. \tag{3.24}$$

If all the eigenvalues of M have non-positive real parts then, from (3.23) and (3.24), $w_i(t) \leq w_i(0)$ for all i, which implies $\|\mathbf{w}(t)\|_h \leq \|\mathbf{w}(0)\|_h$, and from Lemma 3.2,

$$\|\mathbf{v}(t)\|_h \leq K \|\mathbf{f}(x)\|_h .$$

Therefore, for this case, if all eigenvalues of M have non-positive real part then the approximation (3.17) is time-stable.

Case II - M does not have m linearly independent eigenvectors: In this case the matrix M cannot be diagonalized. However, it can still be transformed into the Jordan canonical form where J is a block diagonal matrix given by

$$J = \begin{bmatrix} J_0 & & & \\ & J_1 & & \\ & & \ddots & \\ & & & J_s \end{bmatrix}, \tag{3.25}$$

and S constitutes m linearly independent vectors (not all eigenvectors). J_0 is a diagonal matrix, $J_0 = \text{diag}(\lambda_1, \ldots, \lambda_k)$, whose diagonal elements are the eigenvalues with corresponding linearly independent eigenvectors. J_i is an $m_i \times m_i$ matrix of the form

$$J_i = \begin{bmatrix} \lambda_{k+i} & 1 & 0 & \cdots & 0 \\ 0 & \ddots & \ddots & \ddots & \vdots \\ \vdots & \ddots & \ddots & \ddots & 0 \\ \vdots & & \ddots & \ddots & 1 \\ 0 & \cdots & \cdots & 0 & \lambda_{k+i} \end{bmatrix}, \qquad i = 1, \ldots, s \tag{3.26}$$

such that $k + m_1 + \cdots + m_s = m$. Note that the eigenvalues λ_{k+i} may not be distinct for different Jordan blocks J_i. The matrix exponential for the diagonal matrix J_0 is $e^{J_0 t} = \text{diag}(e^{\lambda_1 t}, \ldots, e^{\lambda_k t})$, and for the Jordan blocks J_i using (3.22) is

$$e^{J_i t} = e^{\lambda_{k+i} t} \begin{bmatrix} 1 & t & \frac{t^2}{2} & \cdots & \frac{t^{n_i-1}}{(n_i-1)!} \\ 0 & 1 & t & \ddots & \frac{t^{n_i-2}}{(n_i-2)!} \\ \vdots & \ddots & \ddots & \ddots & \vdots \\ \vdots & & \ddots & \ddots & t \\ 0 & \cdots & \cdots & 0 & 1 \end{bmatrix}, \qquad i = 1, \ldots, s. \tag{3.27}$$

If $Re(\lambda_{k+i})=\alpha$, it can be shown that $\left\|e^{J_i t}\right\|_h \leq C \left\|e^{(\alpha+\epsilon)t}\right\|_h$ for any value of $\epsilon > 0$, where C is a constant independent of t. Therefore any eigenvalue λ_{k+i} (associated with J_i for $i \geq 1$) with non-negative real part, α, leads to an exponentially growing bound. But if all eigenvalues of M have non-positive real part and if the eigenvalues with zero real part only appear in J_0 (i.e. their geometric multiplicity is equal to their algebraic multiplicity) then $\left\|e^{Jt}\right\| \leq K_1$ which proves time stability.

Conversely assume that the approximation (3.17) is time-stable and has an eigenvalue with positive real part or has an eigenvalue with zero real part that does not belong to J_0, then either a term in $e^{J_0 t} = \text{diag}(e^{\lambda_1 t}, \ldots, e^{\lambda_k t})$ or in Eq. (3.27) is unbounded as $t \to \infty$, which is a contradiction if the approximation is time-stable. This proves the lemma. □

From Lemmas 3.1 and 3.3 we can state the following theorem.

Theorem 3.1 *The approximation (3.17) is time-stable if either of the following conditions are satisfied,*

1. *There exists a real symmetric positive definite matrix H such that $\mathbf{x}^T H M \mathbf{x} \leq 0$ for all $\mathbf{x}$, or that the symmetric matrix $M^T H + HM$ is negative semidefinite.*

2. *All eigenvalues of M have non-positive real part and the geometric multiplicity of every eigenvalue with zero real part is equal to its algebraic multiplicity.*

If all eigenvalues of M have negative real part then the approximation (3.17) is exponentially time-stable.

Chapter 4

Stable Overset Methods for Hyperbolic Problems-I

In this chapter, we present the first case of our SBP-SAT based overset method for hyperbolic problems. We provide the proof of time-stability for a one-dimensional scalar problem (Section 4.1) and a one-dimensional system of hyperbolic equations (Section 4.2). The proposed method uses the SAT approach, discussed in chapter 3, for the interface treatment, which is different from the commonly used strategy of imposing the interface conditions where the computed solution at the interface is overwritten by the interpolated value from the underlying grid (see Berger & Colella, 1989). We will refer to the latter approach as the "injection method".

The time-stable 1-D overset method is then extended to solve the 2-D Euler equations, and a comparative study against the injection method is conducted to assess the performance of the new method. Proving stability of the overset method for the constant coefficient 2-D Euler equations, while possible for simple overlapping grid configurations, is difficult for an arbitrary two-dimensional overlap. Therefore, we perform the analysis for the 1-D problems and then logically extend the method for a 2-D setup.

4.1 The Scalar Problem

We discuss the construction of a time-stable scheme for the one-dimensional advection equation,

$$\frac{\partial U}{\partial t} + \frac{\partial U}{\partial x} = 0, \quad \text{for} \quad -1 \leq x \leq 1,\ t \geq 0, \tag{4.1}$$

on an overlapping grid as shown in Figure 4.1. Initial condition and the boundary condition is given by

$$U(x,0) = f(x), \tag{4.2}$$

$$U(-1,t) = g(t). \tag{4.3}$$

4.1.1 Grid Configuration and Interpolation

The overlapping mesh configuration considered here is shown in Figure 4.1. The left and right domain contain equally spaced $m+1$ and $n+1$ grid points, respectively. Let the grid functions on the left and right domain be denoted by $\mathbf{u}(t) = [u_0(t), \ldots, u_m(t)]^T$ and $\mathbf{v}(t) = [v_0(t), \ldots, v_n(t)]^T$, respectively. We need to specify a numerical boundary condition (NBC) at the interface, which is imposed based on the characteristic direction at the first grid point of the right domain (x_0^R) by interpolation from k grid points of the left domain, as shown by the red arrow in Figure 4.1. The numerical boundary condition is given by

$$\hat{v}_0 = T_L^T \mathbf{u}, \tag{4.4}$$

$$T_L = [0 \ldots . 0 \; l_{j+1} \ldots . l_{j+k} \; 0 \ldots . \; 0]^T, \tag{4.5}$$

where T_L is a vector of size $m+1$ and $l_{j+1}, \cdots, l_{j+k}$ are the interpolation coefficients.

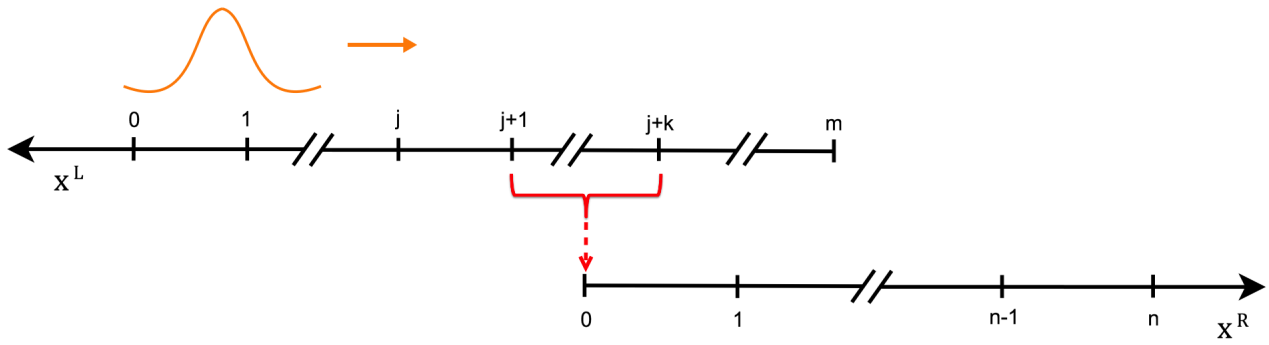

Figure 4.1: Schematic diagram of overlapping grids on which Eq. (4.1) is solved. Downward pointing red arrow denotes the interpolation.

4.1.2 Numerical Scheme

The semidiscrete approximation of Eq. (4.1) with the boundary and interface condition is given by

$$\frac{d\mathbf{u}}{dt} = -P_L^{-1} Q_L \mathbf{u} - \tau_L P_L^{-1} e_0^L (u_0 - g), \tag{4.6}$$

$$\frac{d\mathbf{v}}{dt} = -P_R^{-1} Q_R \mathbf{v} - \tau_R P_R^{-1} e_0^R (v_0 - \hat{v}_0), \tag{4.7}$$

$$e_0^{L,R} = [1\, 0 \ldots 0]^T,$$

where e_0^L and e_0^R are vectors of size $(m+1)$ and $(n+1)$ respectively. The subscripts L and R denote that

the operator corresponds to the left and the right domain respectively, and is appropriately sized. Whenever the group "L, R" appears as a subscript or a superscript in an expression it implies that the expression is valid for the L or R operators. Eqs. (4.6)–(4.7) could be rewritten as

$$\frac{d\mathbf{w}}{dt} = M\mathbf{w} + \mathbf{b}, \qquad \mathbf{w} = \begin{bmatrix} \mathbf{u} \\ \mathbf{v} \end{bmatrix}. \tag{4.8}$$

For time stability it is sufficient to consider the case with $g(t) = 0$ which yields

$$M = \begin{bmatrix} -P_L^{-1}Q_L - \tau_L P_L^{-1} E_0^L & 0 \\ \\ \tau_R P_R^{-1} e_0^R I_L^T & -P_R^{-1}Q_R - \tau_R P_R^{-1} E_0^R \end{bmatrix}, \qquad \mathbf{b} = \begin{bmatrix} \\ 0 \\ \\ \end{bmatrix}, \tag{4.9}$$

$$E_0^L = e_0^L (e_0^L)^T, \qquad E_0^R = e_0^R (e_0^R)^T.$$

As discussed in section 3.3, the above numerical scheme is time-stable if we can show that the real part of all eigenvalues of M are non-positive and the geometric multiplicity of every eigenvalue with zero real part is equal to its algebraic multiplicity.

4.1.3 Stability Analysis

The matrix M in Eq. (4.9) is block lower triangular therefore its eigenvalues are same as that of the matrix

$$\hat{M} = \begin{bmatrix} -P_L^{-1}Q_L - \tau_L P_L^{-1} E_0^L & 0 \\ \\ 0 & -P_R^{-1}Q_R - \tau_R P_R^{-1} E_0^R \end{bmatrix}. \tag{4.10}$$

If we assume a symmetric positive definite matrix

$$\hat{H} = \begin{bmatrix} P_L & \\ & P_R \end{bmatrix}, \tag{4.11}$$

we have

$$\hat{H}\hat{M} + \hat{M}^*\hat{H} = \begin{bmatrix} -(Q_L + Q_L^T) - 2\tau_L E_0^L & 0 \\ \\ 0 & -(Q_R + Q_R^T) - 2\tau_R E_0^R \end{bmatrix}, \tag{4.12}$$

where, * denotes the conjugate transpose of the matrix.

Using the SBP property $Q + Q^T = \text{diag}(-1, 0, \ldots., 1)$, Eq. (4.12) yields

$$\hat{H}\hat{M} + \hat{M}^*\hat{H} = \begin{bmatrix} 1-2\tau_L & & & & & & & & & & \\ & 0 & & & & & & & & & \\ & & \ddots & & & & & & & & \\ & & & 0 & & & & & & & \\ & & & & -1 & & & & & & \\ & & & & & 1-2\tau_R & & & & & \\ & & & & & & 0 & & & & \\ & & & & & & & \ddots & & & \\ & & & & & & & & 0 & & \\ & & & & & & & & & -1 \end{bmatrix}.$$

For $\tau_{L,R} \geq \frac{1}{2}$, the matrix $\hat{H}\hat{M} + \hat{M}^*\hat{H}$ is negative semidefinite. We use the following result from Corless & Frazho (2003):

Lemma 4.1 *If $\hat{H}\hat{M} + \hat{M}^*\hat{H}$ is negative semidefinite, then the real part of all eigenvalues of $\hat{M}$ must be non-positive.*

Proof. Suppose λ_i is an eigenvalue of $\hat{M}$ and let $\mathbf{v}_i$ be the corresponding eigenvector, then

$$\mathbf{v}_i^*(\hat{H}\hat{M} + \hat{M}^*\hat{H})\mathbf{v}_i = \mathbf{v}_i^*\hat{H}(\hat{M}\mathbf{v}_i) + (\hat{M}\mathbf{v}_i)^*\hat{H}\mathbf{v}_i = \mathbf{v}_i^*\hat{H}(\lambda_i\mathbf{v}_i) + (\lambda_i\mathbf{v}_i)^*\hat{H}\mathbf{v}_i = (\lambda_i + \lambda_i^*)\mathbf{v}_i^*\hat{H}\mathbf{v}_i.$$

Since $\hat{H}\hat{M} + \hat{M}^*\hat{H}$ is negative semidefinite,

$$\mathbf{v}_i^*(\hat{H}\hat{M} + \hat{M}^*\hat{H})\mathbf{v}_i \leq 0 \Rightarrow (\lambda_i + \lambda_i^*)\mathbf{v}_i^*\hat{H}\mathbf{v}_i \leq 0 \Rightarrow Re(\lambda_i) \leq 0.$$

The last inequality holds since $\hat{H}$ is positive definite. This proves the lemma. □

The eigenvalues of M are same as that of $\hat{M}$, therefore the real part of all of the eigenvalues of M are also non-positive. Next we show that there are no eigenvalues with zero real part. In order to prove that, we need the following lemma.

Lemma 4.2 *A matrix of size $p \times q$ (for $q < p$) of the form*

$$A = \begin{bmatrix} a_{1,1} & 0 & : & & & \\ a_{2,1} & a_{1,2} & 0 & & & \\ \vdots & a_{2,2} & a_{1,3} & & & \\ a_{k,1} & \vdots & a_{2,3} & \ddots & & \vdots \\ 0 & a_{k,2} & \vdots & \ddots & \ddots & 0 \\ \vdots & 0 & a_{k,3} & \ddots & \ddots & a_{1,q} \\ & \vdots & 0 & \ddots & \ddots & a_{2,q} \\ & & \vdots & \ddots & \ddots & \vdots \\ & & & & \ddots & a_{k,q} \end{bmatrix},$$

where $a_{i,j}$ are non-zero real or complex numbers, has linearly independent columns and therefore the null space of A contains only the zero vector.

Proof. The reduced row echelon form for the above matrix A is

$$R = \begin{bmatrix} 1 & 0 & : & & & \\ 0 & 1 & 0 & & & \\ \vdots & 0 & 1 & \ddots & & \\ & \vdots & 0 & \ddots & \ddots & \vdots \\ & & \vdots & \ddots & \ddots & 0 \\ & & & & \ddots & 1 \\ & & & & & 0 \\ & & & & & \vdots \\ & & & & & \end{bmatrix} = \begin{bmatrix} I \\ \\ 0 \end{bmatrix} \tag{4.13}$$

where I is an identity matrix of size $q \times q$. Therefore, $\text{rank}(A) = q$ and hence the solution of $Ax = 0$ is only the trivial solution $x = 0$. This proves the lemma. □

An alternative way of looking at Lemma 4.2 is that since each column vector, compared to other column vectors, has at least one component in a dimension in which the other vectors have zero component it must be linearly independent of the other vectors. In our subsequent analysis, we denote the first derivative SBP operators based on a diagonal norm as $p - 2p - p$, where p gives the order of accuracy at the boundary and $2p$ in the interior.

Lemma 4.3 *Real part of all eigenvalues of $M_L = -P_L^{-1}Q_L - \tau_L P_L^{-1}E_0^L$ is negative if $\tau_L \geq \frac{1}{2}$ and $P_L^{-1}Q_L$ is the $1 - 2 - 1$ SBP operator for the first derivative approximation (see Appendix A.1).*

Proof. We have

$$P_L M_L + M_L^* P_L = \begin{bmatrix} 1-2\tau_L & & & & \\ & 0 & & & \\ & & \ddots & & \\ & & & 0 & \\ & & & & -1 \end{bmatrix}. \tag{4.14}$$

Let $\mathbf{v}_i = [\mathbf{v}_{i,0}\,,\,\ldots\,,\,\mathbf{v}_{i,m}]^T$ be the eigenvector corresponding to an eigenvalue λ_i of M_L, then from Eq. (4.14) and Lemma ,

$$\mathbf{v}_i^*(P_L M_L + M_L^* P_L)\mathbf{v}_i = (1-2\tau_L)\mathbf{v^2}_{i,0} - \mathbf{v^2}_{i,m} = 2Re(\lambda_i)\mathbf{v}_i^* P_L \mathbf{v}_i. \tag{4.15}$$

P_L is positive-definite, and hence Eq. (4.15) gives

$$Re(\lambda_i) = \frac{(1-2\tau_L)\mathbf{v^2}_{i,0} - \mathbf{v^2}_{i,m}}{2\mathbf{v}_i^* P_L \mathbf{v}_i}.$$

$\tau_L \geq \frac{1}{2}$ implies $Re(\lambda_i) \leq 0$, where $Re(\lambda_i) = 0$ if and only if $\mathbf{v}_{i,0} = \mathbf{v}_{i,m} = 0$. This result implies that we should have $(M_L - \lambda_i I)\mathbf{v}_i = 0$ with $\mathbf{v}_i = [0\,,\,\mathbf{v}_{i,1}\,,\,\ldots\,,\,\mathbf{v}_{i,m-1}\,,\,0]^T$ or

$$(M_L - \lambda_i I)\mathbf{v}_i = \begin{bmatrix} -1 & & & & & & \\ -\lambda_i & -\frac{1}{2} & & & & & \\ \frac{1}{2} & -\lambda_i & -\frac{1}{2} & & & & \\ & \frac{1}{2} & -\lambda_i & & & & \\ & & \frac{1}{2} & \ddots & -\frac{1}{2} & & \\ & & & & -\lambda_i & -\frac{1}{2} & \\ & & & & \frac{1}{2} & -\lambda_i & \\ & & & & & 1 \end{bmatrix} \begin{bmatrix} \mathbf{v}_{i,1} \\ \mathbf{v}_{i,2} \\ \vdots \\ \vdots \\ \vdots \\ \mathbf{v}_{i,m-1} \end{bmatrix} = 0.$$

Using Lemma 4.2 the above implies $\mathbf{v}_{i,1} = \ldots = \mathbf{v}_{i,m-1} = 0$ i.e. the eigenvector corresponding to eigenvalue λ_i, with $Re(\lambda_i) = 0$, is a zero vector and hence $Re(\lambda_i) \neq 0$. Therefore the real part of all eigenvalues of M_L is negative. This completes the proof. □

Lemma 4.4 *Real part of all eigenvalues of $M_L = -P_L^{-1}Q_L - \tau_L P_L^{-1} E_0^L$ is negative if $\tau_L \geq \frac{1}{2}$ and $P_L^{-1}Q_L$ is the $2-4-2$ SBP operator for the first derivative approximation (see Appendix A.2).*

Proof. Using a similar approach as Lemma 4.3 for the $2-4-2$ SBP operator gives

$$Re(\lambda_i) = \frac{(1-2\tau_L)\mathbf{v^2}_{i,0} - \mathbf{v^2}_{i,m}}{2\mathbf{v}_i^* P_L \mathbf{v}_i},$$

where $\mathbf{v}_i$ is the eigenvector, corresponding to an eigenvalue λ_i of M_L. Similarly, $Re(\lambda_i) = 0$ if and only if $\mathbf{v}_{i,0} = \mathbf{v}_{i,m} = 0$, which implies $(M_L - \lambda_i I)\mathbf{v}_i = 0$ or,

$$\begin{bmatrix}
-\frac{59}{34} & \frac{4}{17} & \frac{3}{34} & 0 & & & & & & & & & \\
-\lambda_i & -\frac{1}{2} & 0 & 0 & & & & & & & & & \\
\frac{59}{86} & -\lambda_i & -\frac{59}{86} & \frac{4}{43} & & & & & & & & & \\
 & \frac{59}{98} & -\lambda_i & -\frac{32}{49} & \frac{4}{49} & & & & & & & & \\
 & -\frac{1}{12} & \frac{2}{3} & -\lambda_i & -\frac{2}{3} & \frac{1}{12} & & & & & & & \\
 & & -\frac{1}{12} & \frac{2}{3} & -\lambda_i & -\frac{2}{3} & \ddots & & & & & & \\
 & & & -\frac{1}{12} & \frac{2}{3} & -\lambda_i & \ddots & \frac{1}{12} & & & & & \\
 & & & & -\frac{1}{12} & \frac{2}{3} & \ddots & -\frac{2}{3} & \frac{1}{12} & & & & \\
 & & & & & -\frac{1}{12} & \ddots & -\lambda_i & -\frac{2}{3} & \frac{1}{12} & & & \\
 & & & & & & \ddots & \frac{2}{3} & -\lambda_i & -\frac{2}{3} & \frac{1}{12} & & \\
 & & & & & & & -\frac{1}{12} & \frac{2}{3} & -\lambda_i & -\frac{2}{3} & \frac{1}{12} & \\
 & & & & & & & & -\frac{4}{49} & \frac{32}{49} & -\lambda_i & -\frac{59}{98} & \\
 & & & & & & & & & -\frac{4}{43} & \frac{59}{86} & -\lambda_i & -\frac{59}{86} \\
 & & & & & & & & & & 0 & \frac{1}{2} & -\lambda_i \\
 & & & & & & & & & & -\frac{3}{34} & -\frac{4}{17} & \frac{59}{34}
\end{bmatrix}
\begin{bmatrix} \mathbf{v}_{i,1} \\ \mathbf{v}_{i,2} \\ \\ \vdots \\ \\ \vdots \\ \\ \vdots \\ \\ \mathbf{v}_{i,m-1} \end{bmatrix} = 0.$$

It can be shown, by computing the reduced row echelon form, that the columns of $M_L - \lambda_i I$ are linearly independent for any value of λ_i and therefore $\mathbf{v}_{i,1} = ... = \mathbf{v}_{i,m-1} = 0$ and hence $Re(\lambda_i) \neq 0$. This concludes the proof for the $2-4-2$ scheme. □

Theorem 4.1 *The numerical scheme given by Eq. (4.6)–(4.7) for the left and the right domain, respectively, to solve (4.1), is time-stable with the* $1-2-1$ *SBP operator and* $\tau_{L,R} \geq \frac{1}{2}$.

Proof. Analysis similar to Lemma 4.3 shows that the real part of all eigenvalues of $M_R = -P_R^{-1}Q_R - \tau_R P_R^{-1} E_0^R$ are negative for P_R and Q_R operators corresponding to $1-2-1$ SBP scheme with $\tau_R \geq \frac{1}{2}$. Therefore, the real part of all eigenvalues of $\hat{M}$, (see Eq. (4.10)), are negative and consequently the same holds for M. Use of theorem 3.1 then shows that the method (4.6) and (4.7) for the left and the right domain, respectively, is time-stable. □

Since in this case all eigenvalues of M have negative real part the method is exponentially time-stable and there exists a positive definite matrix H such that $HM + M^T H < 0$ (see Chapter 3 in Corless & Frazho,

2003, for proof) which implies

$$\frac{d}{dt}||\mathbf{w}||_H^2 = \mathbf{w}^T(HM + M^T H)\mathbf{w} < 0.$$

Theorem 4.2 *The numerical scheme given by Eq. (4.6)-(4.7) for the left and right domain respectively, to solve (4.1), is time-stable with* $2-4-2$ *SBP scheme and* $\tau_{L,R} \geq \frac{1}{2}$.

Proof. The proof follows from Lemma 4.3 in exactly the same manner as Theorem 4.1. □

The analysis also shows that the method could be extended to any number of overlapping 1D domains. If the domain contains k overset grids then the matrix M will have k diagonal blocks each having all eigenvalues with negative real part. M will be block upper triangular if the direction of propagation is right-to-left and block lower triangular if the propagation is left-to-right. Since the off-diagonal blocks, which contain the interpolation coefficients, do not influence the eigenvalues of the system, the above proof of stability holds regardless of the amount of overlap between domains and the interpolation method used. A similar approach could be used to analyze the stability of a scheme with, for example, $3-6-3$ and $4-8-4$ SBP operators.

4.2 Hyperbolic System in One Dimension

In this section, we discuss the extension of (4.6)–(4.7) to a system of hyperbolic equations and show that the resulting scheme is time-stable. Consider the same grid configuration as Section 4.1.1 and let the system of differential equations be given by

$$\frac{\partial u}{\partial t} = \Lambda \frac{\partial u}{\partial x}, \tag{4.16}$$

where

$$u = [u^1,\, u^2,\, \ldots,\, u^k,\, u^{k+1},\, \ldots..,\, u^r]^T, \qquad \Lambda = \mathrm{diag}(\lambda_1,\, \lambda_2,\, \ldots,\, \lambda_k,\, \lambda_{k+1},\, \ldots..,\, \lambda_r),$$

such that

$$\lambda_1 < \lambda_2 < \ldots < \lambda_k < 0 < \lambda_{k+1} < \ldots.. < \lambda_r.$$

Well-posed set of boundary conditions based on the characteristic direction is given by

$$u^i(a,\, t) = g_i(t), \qquad 1 \leq i \leq k \tag{4.17}$$

$$u^i(b,\, t) = g_i(t), \qquad k < i \leq r \tag{4.18}$$

The semidiscrete approximation of the system of equations (4.16) with the above boundary condition is

for $1 \le i \le k$:

$$\frac{d\mathbf{u}^i}{dt} = \lambda_i P_L^{-1} Q_L \mathbf{u}^i - |\lambda_i| \tau_L P_L^{-1} e_0^L (u_0^i - g_i), \tag{4.19}$$

$$\frac{d\mathbf{v}^i}{dt} = \lambda_i P_R^{-1} Q_R \mathbf{v}^i - |\lambda_i| \tau_R P_R^{-1} e_0^R (v_0^i - I_L^T u), \tag{4.20}$$

for $k < i \le r$:

$$\frac{d\mathbf{u}^i}{dt} = \lambda_i P_L^{-1} Q_L \mathbf{u}^i - |\lambda_i| \tau_L P_R^{-1} e_m^L (u_m^i - I_R^T u), \tag{4.21}$$

$$\frac{d\mathbf{v}^i}{dt} = \lambda_i P_R^{-1} Q_R \mathbf{v}^i - |\lambda_i| \tau_R P_R^{-1} e_n^R (v_n^i - g_i). \tag{4.22}$$

We can collectively write the above as

$$\frac{d\mathbf{u}^i}{dt} = \lambda_i P_L^{-1} Q_L \mathbf{u}^i - H[k-i] \, |\lambda_i| \tau_L P_L^{-1} e_0^L (u_0^i - g_i) - H[i-k-1] \, |\lambda_i| \tau_L P_L^{-1} e_m^L (u_m^i - I_R^T u), \tag{4.23}$$

$$\frac{d\mathbf{v}^i}{dt} = \lambda_i P_R^{-1} Q_R \mathbf{v}^i - H[k-i] \, |\lambda_i| \tau_R P_R^{-1} e_0^R (v_0^i - I_L^T u) - H[i-k-1] \, |\lambda_i| \tau_R P_R^{-1} e_n^R (v_n^i - g_i), \tag{4.24}$$

where $H[n]$ denotes the Heaviside step function,

$$H[n] = \begin{cases} 0, & n < 0 \\ 1, & n \ge 0 \end{cases}.$$

Eqs. (4.23) and (4.24) could be rewritten as

$$\frac{d\mathbf{w}^i}{dt} = M^i \mathbf{w}^i + B^i, \qquad \mathbf{w}^i = \begin{bmatrix} \mathbf{u}^i \\ \mathbf{v}^i \end{bmatrix}, \tag{4.25}$$

where

$$M^i = \begin{bmatrix} M_L^i & H[i-k-1] \, |\lambda_i| \tau_L P_L^{-1} e_m^L I_R^T \\ H[k-i] \, |\lambda_i| \tau_R P_R^{-1} e_0^R I_L^T & M_R^i \end{bmatrix}, \tag{4.26}$$

$$B^i = \begin{bmatrix} H[k-i] \, |\lambda_i| \tau_L P_L^{-1} e_0^L g_i \\ H[i-k-1] \, |\lambda_i| \tau_R P_R^{-1} e_n^R g_i \end{bmatrix},$$

$$M_L^i = \lambda_i P_L^{-1} Q_L - H[k-i] \, |\lambda_i| \tau_L P_L^{-1} E_0^L - H[i-k-1] \, |\lambda_i| \tau_L P_L^{-1} E_m^L,$$

$$M_R^i = \lambda_i P_R^{-1} Q_R - H[k-i]\,|\lambda_i|\,\tau_R P_R^{-1} E_0^R - H[i-k-1]\,|\lambda_i|\,\tau_R P_R^{-1} E_n^R,$$

$$E_0^{L,R} = e_0^{L,R}(e_0^{L,R})^T, \qquad E_{m,n}^{L,R} = e_{m,n}^{L,R}(e_{m,n}^{L,R})^T.$$

It must be noted that for a given i, M^i is either block upper or block lower triangular and hence the eigenvalues of M^i are determined only by the diagonal blocks. The numerical scheme, given by Eq. (4.25), for individual i's could be combined as follows

$$M = \begin{bmatrix} M^1 & & & \\ & M^2 & & \\ & & \ddots & \\ & & & M^r \end{bmatrix}, \qquad \mathbf{w} = \begin{bmatrix} \mathbf{w^1} \\ \vdots \\ \vdots \\ \mathbf{w}^r \end{bmatrix}, \qquad B = \begin{bmatrix} B^1 \\ \vdots \\ \vdots \\ B^r \end{bmatrix}, \tag{4.27}$$

to obtain the semidiscretized equation for Eq. (4.16) as

$$\frac{d\mathbf{w}}{dt} = M\mathbf{w} + B. \tag{4.28}$$

Theorem 4.3 *The numerical scheme defined by Eq. (4.28) is a time-stable approximation of hyperbolic system, Eq. (4.16), with boundary conditions Eq. (4.17) and (4.18).*

Proof. M, in Eq. (4.28), is a block diagonal matrix composed of M^i on the diagonal therefore the eigenvalues of M are the eigenvalues of individual M^i matrices. From Theorem 4.1 and Theorem 4.2 we know that real part of all eigenvalues of each M^i is negative for $1-2-1$ and $2-4-2$ SBP operator therefore the same should be true for M. Hence M is exponentially time-stable and there exists a positive definite matrix H such that $HM + M^T H < 0$ (see Corless & Frazho, 2003, for proof), which implies

$$\frac{d}{dt}||\mathbf{w}||_H^2 = \mathbf{w}^T(HM + M^T H)\mathbf{w} < 0. \qquad \square$$

4.3 Numerical Results

In this section, we discuss the numerical results for the overset method discussed above and the shortcomings of the above approach for proof of stability.

4.3.1 Scalar Advection Problem

Consider the problem

$$\frac{\partial u}{\partial t} + \frac{\partial u}{\partial x} = 0, \qquad -1 \leq x \leq 1, \qquad t \geq 0, \tag{4.29}$$

$$u(x,0) = f(x) = \begin{cases} e^{-\frac{1}{(x-a)(b-x)} + \frac{4}{(b-a)^2}} & a < x < b \\ 0 & x \leq a,\ x \geq b \end{cases}, \qquad -1 \leq x \leq 1, \tag{4.30}$$

$$u(-1,t) = 0, \qquad t \geq 0. \tag{4.31}$$

We choose $a = -0.95$ and $b = -0.05$, which ensures $f(x)$ goes to zero smoothly at the left boundary. The domain $x \in [-1,1]$ is split into the left and the right overlapping subdomains, $x_L \in [-1,0]$ and $x_R \in [-\frac{7}{2}h_L, 1]$, where h_L denotes the grid spacing on the left domain. Figure 4.2 shows the solution at different times to the above problem with the $1-2-1$ SBP first derivative approximation. There are 100 grid points on the left domain and 50 on the right. Figure 4.3 gives the eigenvalues of the system matrix M, see Eq. (4.9), for the $1-2-1$ SBP first derivative approximation. As proven earlier, all eigenvalues have negative real part. Figures 4.4, 4.5 and 4.6 show the convergence on the left and the right grid of the method with the $1-2-1$, $2-4-2$ and $3-6-3$ SBP first derivative approximation, respectively. Table 4.1 shows the L^2-error and the convergence rate for the full computational domain. Linear Lagrange interpolation was used with the $1-2-1$ operator and cubic Lagrange interpolation with the $2-4-2$ and $3-6-3$ operators. For all calculations the classical fourth-order Runge-Kutta (RK4) method was used for the temporal integration. In convergence plots, $\triangle x$ (on the x-axis) denotes the grid spacing of the respective domain i.e. for the blue line $\triangle x = h_L$ and for the red line $\triangle x = h_R$, and t_f denotes the time at which the error was computed for each refinement. The refinements carried out for the convergence analysis maintained a grid point ratio of $2N : N$ between the left and the right domain. The convergence rate in each case asymptotes to a value one order higher than the order of accuracy of the boundary stencils, consistent with the theory in Gustafsson (1975).

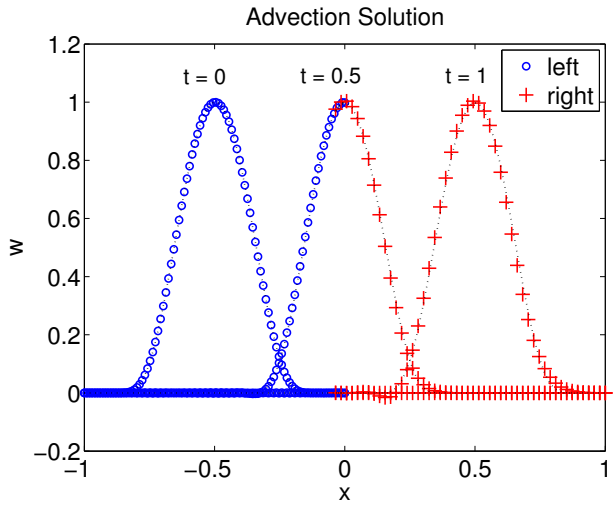

Figure 4.2: Solution to problem (4.29) using the method (4.6)-(4.7), with $1-2-1$ SBP operators. Blue circles mark the solution on the left subdomain and red pluses on the right.

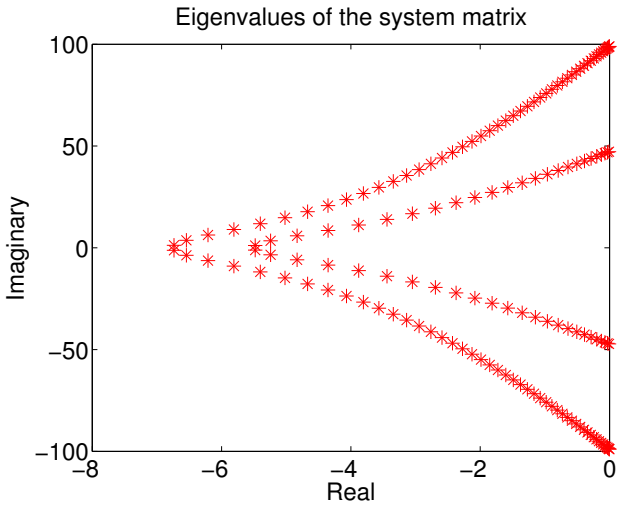

Figure 4.3: Eigenvalue spectrum of the system matrix M, given by Eq. (4.9), for the $1-2-1$ SBP first derivative approximation.

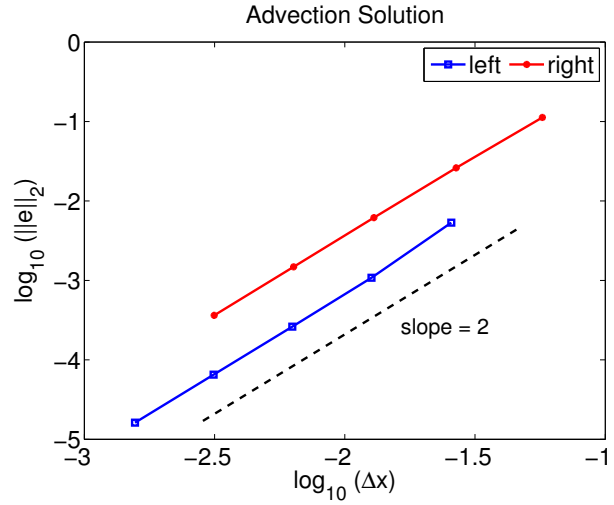

Figure 4.4: Convergence plot of the method (4.6)-(4.7) with $1-2-1$ SBP first derivative approximation at $t_f = 0.5$.

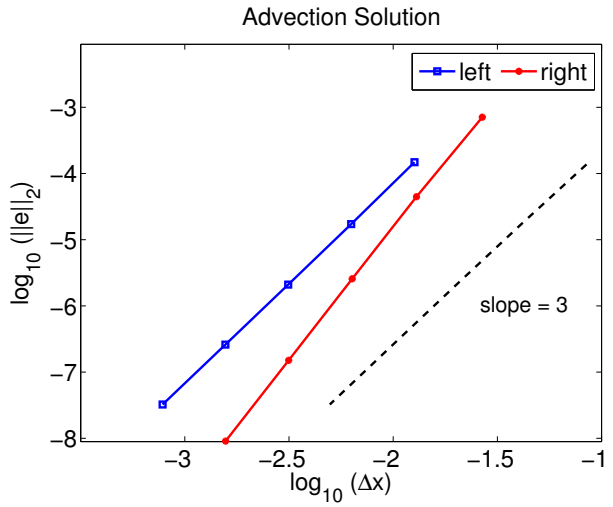

Figure 4.5: Convergence plot of the method (4.6)-(4.7) with $2-4-2$ SBP first derivative approximation at $t_f = 0.5$.

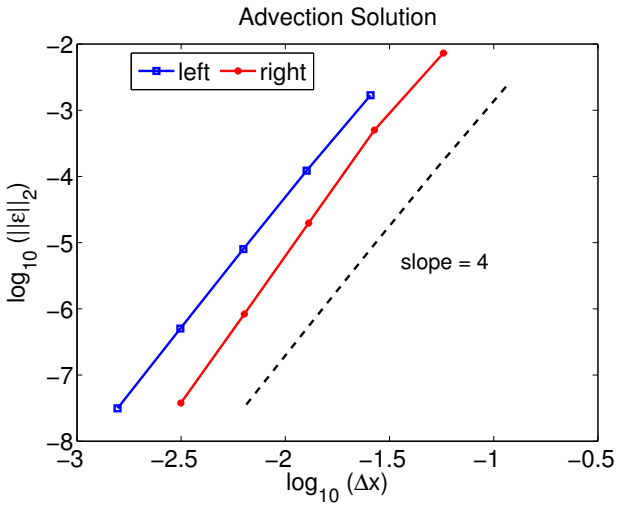

Figure 4.6: Convergence plot of the method (4.6)-(4.7) with $3-6-3$ SBP first derivative approximation at $t_f = 0.5$.

	$1-2-1$		$2-4-2$		$3-6-3$	
N	$\log_{10}\|\|\epsilon\|\|_2$	Rate	$\log_{10}\|\|\epsilon\|\|_2$	Rate	$\log_{10}\|\|\epsilon\|\|_2$	Rate
20	-1.372494		-2.074846		-2.156269	
40	-2.024602	2.127	-3.141376	3.479	-3.400320	4.058
80	-2.671394	2.129	-4.320283	3.881	-4.770536	4.511
160	-3.297982	2.072	-5.479973	3.835	-6.087828	4.356
320	-3.911992	2.035	-6.522413	3.455	-7.361104	4.220

Table 4.1: $\text{Log}_{10}(L^2\text{-error})$ and the convergence rate with the $1-2-1$, $2-4-2$ and $3-6-3$ SBP first derivative approximation. Error calculations performed at $t_f = 0.5$ with $2N$ grid points on the left domain and N on the right domain.

4.3.2 Inviscid Burgers' Equation

We solve the inviscid Burgers' equation with a Gaussian initial pulse,

$$\frac{\partial u}{\partial t} + u\frac{\partial u}{\partial x} = 0, \qquad -1 \leq x \leq 1, \qquad t \geq 0, \tag{4.32}$$

$$u(x,0) = e^{-3x^2}.$$

An implicit relation that determines the solution to the Cauchy problem, provided the characteristics do not intersect, is given by

$$u(x,t) = e^{-3(x-ut)^2}.$$

It was solved using the Newton's method to specify the boundary condition and to compute the error of the solution. For the given initial condition, the time at which shock first forms is given by $t^* = \frac{e^{1/2}}{\sqrt{6}} \approx 0.6731$. Figure 4.7 shows the solution at different times on a domain $x \in [-1, 1]$ with the overlapping subdomains, $x_L \in [-1, 0]$ and $x_R \in [-\frac{7}{2}h_L, 1]$. Table 4.2 shows the convergence of the method with different SBP first derivative approximations. t_f denotes the time at which the error was computed for each refinement.

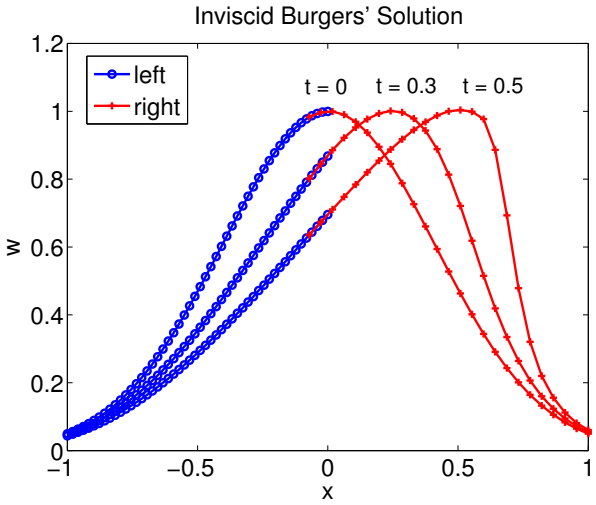

Figure 4.7: Solution to the problem (4.32).

	$1-2-1$		$2-4-2$		$3-6-3$	
N	$\log_{10}\|\|\epsilon\|\|_2$	Rate	$\log_{10}\|\|\epsilon\|\|_2$	Rate	$\log_{10}\|\|\epsilon\|\|_2$	Rate
20	-2.576613		-3.738387		-3.856417	
40	-3.207787	2.059	-4.931214	3.891	-5.286009	4.663
80	-3.826177	2.036	-6.002457	3.526	-6.708011	4.681
160	-4.437252	2.021	-6.979866	3.232	-7.917851	4.019
320	-5.043937	2.011	-7.906194	3.070		

Table 4.2: $\text{Log}_{10}(L^2\text{-error})$ and the convergence rate with the $1-2-1$ and the $2-4-2$ SBP first derivative approximation. Error calculations performed at $t_f = 0.25$ with $2N$ grid points on the left domain and N on the right domain.

4.3.3 The Euler Equations

We solve the two-dimensional Euler equations (see Eq. (3.8)) for the propagation of a compressible vortex under isentropic conditions. Initial and boundary conditions are determined from the exact solution given by

$$\begin{aligned}
&\rho = (1 - \frac{\epsilon^2(\gamma-1)}{8\pi^2\gamma} e^{1-\beta^2 r^2})^{\frac{1}{\gamma-1}}, \qquad && u = u_0 - \frac{\epsilon}{2\pi}\beta(y - y_0 - v_0 t) e^{\frac{1-\beta^2 r^2}{2}}, \\
&v = \frac{\epsilon}{2\pi}\beta(x - x_0 - u_0 t) e^{\frac{1-\beta^2 r^2}{2}}, && E = \frac{p}{\gamma-1} + \frac{1}{2}\rho(u^2+v^2), \\
&p = \rho^\gamma, && r^2 = (x - x_0 - u_0 t)^2 + (y - y_0 - v_0 t)^2,
\end{aligned} \tag{4.33}$$

where $(x_0,\, y_0)$ denotes the initial position of the vortex, (u_0, v_0) denotes the vortex convective velocity, γ is the ratio of specific heats, β controls the size of the vortex and ϵ denotes the non-dimensional circulation. Unless otherwise stated, we use $v_0 = 0$, $\gamma = 1.4$, $\beta = 11$ and $\epsilon = 1$. All quantities in (4.33) are non-dimensional, obtained from the density scale $= \rho_0^*$, velocity scale $u_0^* = \frac{c_0^*}{\sqrt{\gamma}}$, unit length scale and pressure scale $= \rho_0^* u_0^{*2}$, where $*$ denotes the dimensional quantities. The non-dimensional ambient speed of sound is $c_0 = \sqrt{\gamma}$.

Consider a simple two-grid overset configuration as shown in Figure 4.8, where the interface conditions are needed only on one edge of each gird. We refer to the domain with black grid as the left domain and the domain with red grid as the right domain. Following a similar notation as section 3.2.2, we denote the solution field by $q_{ijl}^{L,R}$ where the first two subscript indices i and j represent the x and y index of the grid point and the last index l, ranging between 1 and 4, represents the conservative variable, the superscript denotes the domain to which the grid function belongs. We assume $n_x^{L,R} + 1$ and $n_y^{L,R} + 1$ grid points in the x and y direction of the left and right grid. Define the vector $\mathbf{Q}^{L,R} = (q_{001}^{L,R},\, q_{002}^{L,R},\, ...,\, q_{n_x n_y 4}^{L,R})^T$. For the configuration shown in Figure 4.8 the discretization for the left and right domain, ignoring the physical boundaries, is given by

$$\frac{d\mathbf{Q}^L}{\partial t} = -\mathbf{D}_\mathbf{x}^L \mathbf{F}^L - \mathbf{D}_\mathbf{y}^L \mathbf{G}^L - \tau_1 (\mathbf{P}_\mathbf{x}^L)^{-1} \mathbf{E}_\mathbf{nx}^\mathbf{L} \mathbf{K}_\mathbf{x}^{L-} (\mathbf{Q}^L - \mathbf{T}^\mathbf{R}\mathbf{Q}^\mathbf{R}), \tag{4.34}$$

$$\frac{d\mathbf{Q}^R}{\partial t} = -\mathbf{D}_\mathbf{x}^R \mathbf{F}^R - \mathbf{D}_\mathbf{y}^R \mathbf{G}^R - \tau_1 (\mathbf{P}_\mathbf{x}^R)^{-1} \mathbf{E}_\mathbf{0x}^R \mathbf{K}_\mathbf{x}^{R+} (\mathbf{Q}^R - \mathbf{T}^\mathbf{L}\mathbf{Q}^\mathbf{L}), \tag{4.35}$$

where $\mathbf{T}^{\mathbf{L,R}}$ denotes the interpolation operator and

$$\mathbf{K}_\mathbf{x}^\pm = \mathbf{S}_\mathbf{x} \left(\frac{|\mathbf{\Lambda_x}| \pm \mathbf{\Lambda_x}}{2} \right) \mathbf{S}_\mathbf{x}^{-1}, \qquad , \mathbf{S_x} = I_y \otimes I_x \otimes S_x, \qquad \mathbf{\Lambda_x} = I_y \otimes I_x \otimes \Lambda_x.$$

Λ_x and Λ_y are diagonal matrices with the eigenvalues of $\tilde{A}$ and $\tilde{B}$ as the diagonal elements, where $\tilde{A} = \frac{\partial F}{\partial Q}$ and $\tilde{B} = \frac{\partial G}{\partial Q}$ (see Eq. (3.8)) such that

$$\Lambda_x = S_x^{-1}\tilde{A}S_x, \qquad \Lambda_y = S_y^{-1}\tilde{B}S_y.$$

We use tilde (˜) over A and B here to highlight the fact that the matrices $\tilde{A}$ and $\tilde{B}$ are different from the matrices A and B of Section 3.2.2. The eigenvalue matrices are given by

$$\Lambda_x = \begin{bmatrix} u & & & \\ & u & & \\ & & u+c & \\ & & & u-c \end{bmatrix}, \qquad \Lambda_y = \begin{bmatrix} v & & & \\ & v & & \\ & & v+c & \\ & & & v-c \end{bmatrix}.$$

The right eigenvector matrices are given by

$$S_x = \begin{bmatrix} 1 & 0 & 1 & 1 \\ u & 0 & u+c & u-c \\ v & -1 & v & v \\ \frac{\phi^2}{(\gamma-1)} & -v & [\frac{\phi^2+c^2}{(\gamma-1)} + cu] & [\frac{\phi^2+c^2}{(\gamma-1)} - cu] \end{bmatrix}, \qquad S_y = \begin{bmatrix} 1 & 0 & 1 & 1 \\ u & 1 & u & u \\ v & 0 & v+c & v-c \\ \frac{\phi^2}{(\gamma-1)} & u & [\frac{\phi^2+c^2}{(\gamma-1)} + cv] & [\frac{\phi^2+c^2}{(\gamma-1)} - cv] \end{bmatrix},$$

and the corresponding left eigenvector matrices by

$$S_x^{-1} = \begin{bmatrix} 1-\frac{\phi^2}{c^2} & (\gamma-1)\frac{u}{c^2} & (\gamma-1)\frac{v}{c^2} & -\frac{(\gamma-1)}{c^2} \\ v & 0 & -1 & 0 \\ \beta(\phi^2 - cu) & \beta[c-(\gamma-1)u] & -\beta(\gamma-1)v & \beta(\gamma-1) \\ \beta(\phi^2 + cu) & -\beta[c+(\gamma-1)u] & -\beta(\gamma-1)v & \beta(\gamma-1) \end{bmatrix},$$

$$S_y^{-1} = \begin{bmatrix} 1-\frac{\phi^2}{c^2} & (\gamma-1)\frac{u}{c^2} & (\gamma-1)\frac{v}{c^2} & -\frac{(\gamma-1)}{c^2} \\ -u & 1 & 0 & 0 \\ \beta(\phi^2 - cv) & -\beta(\gamma-1)u & \beta[c-(\gamma-1)v] & \beta(\gamma-1) \\ \beta(\phi^2 + cv) & -\beta(\gamma-1)u & -\beta[c+(\gamma-1)v] & \beta(\gamma-1) \end{bmatrix},$$

with $c^2 = \frac{\gamma p}{\rho}$, $\beta = \frac{1}{2c^2}$ and $\phi^2 = \frac{1}{2}(\gamma-1)(u^2+v^2)$.

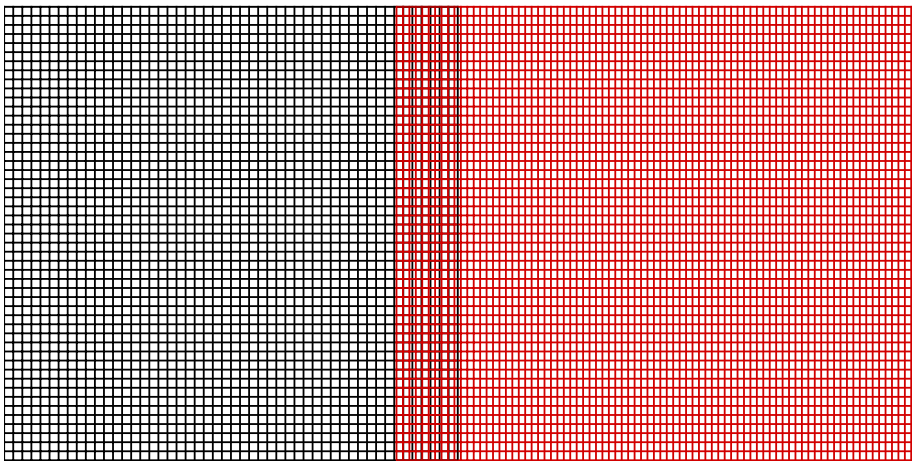

Figure 4.8: Two-grid overset configuration that requires interpolation along just one edge of the either grid.

Grid Configuration-1

We use $u_0 = 1$ in Eq. (4.33) to compute the convection of vortex over time on the grid configuration shown in Figure 4.8 with following number of points on the left and right domain:

Left		Right	
n_x^L	n_y^L	n_x^R	n_y^R
101	101	151	101

.

Figure 4.9 shows the solution at different times. Figure 4.10 shows the convergence of the method with second order accurate difference operator and linear interpolation with t_f denoting the time at which the error is computed for each refinement. For convergence study, each grid is refined in both directions by the same ratio in subsequent refinements and the error is defined as $e_{i,j} = \rho_{i,j}^{computed} - \rho_{i,j}^{exact}$ and,

$$\|\mathbf{e}(t_f)\|_2 = \sqrt{\sum_{k=1}^{M}\left(\sum_{j=0}^{n_y^k}\sum_{i=0}^{n_x^k}((e_{i,j}^k)^2\Delta x_k \Delta y_k)\right)}, \tag{4.36}$$

where M is the number of subdomains, and $n_x^k + 1$ and $n_y^k + 1$ denote the number of grid points in x and y direction of the k-th subdomain. Here $M = 2$. Figures 4.11 and 4.13 show the convection of vortex over time on an overlapping rotated grid configuration and Figures 4.12 and 4.14 are the corresponding convergence plots. All the convergence results are plotted against $\triangle x = \triangle x_L$. One would get the same trend if the error is plotted against $\triangle x_R$ or $\triangle y_L$ or $\triangle y_R$ since we refine both left and right grid in each direction by the same ratio.

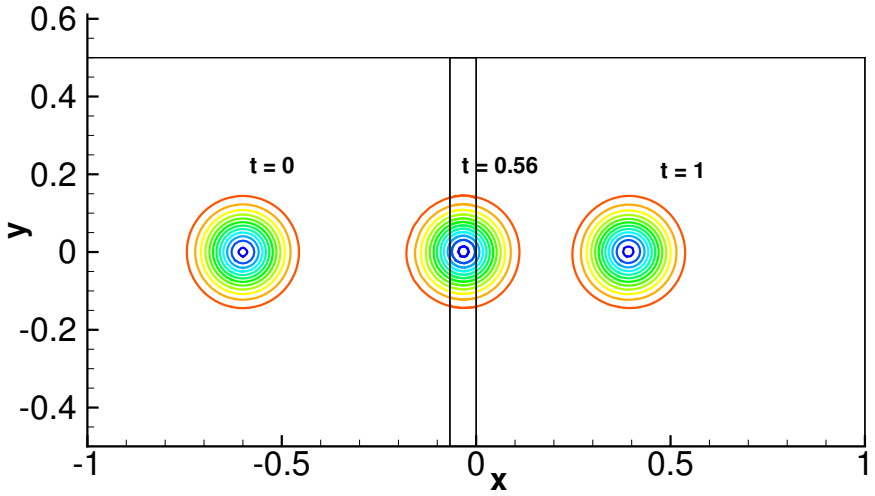

Figure 4.9: Contours of density showing convection of vortex over time.

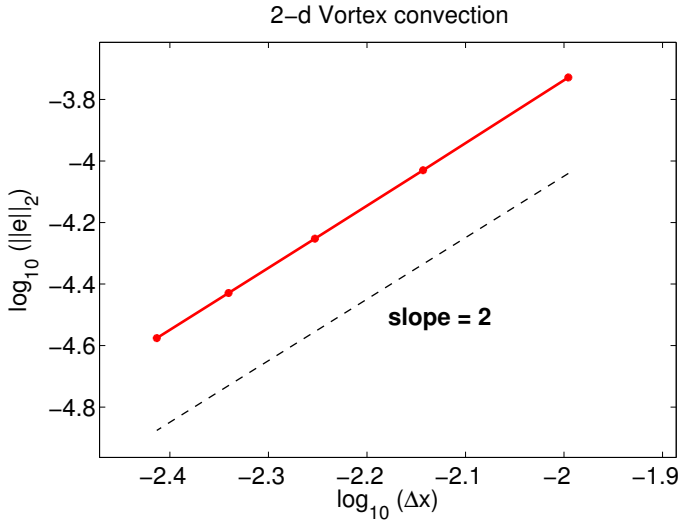

Figure 4.10: Convergence of method (4.34) with $1-2-1$ SBP operator at $t_f = 1$ with $\triangle x = \triangle x_L$.

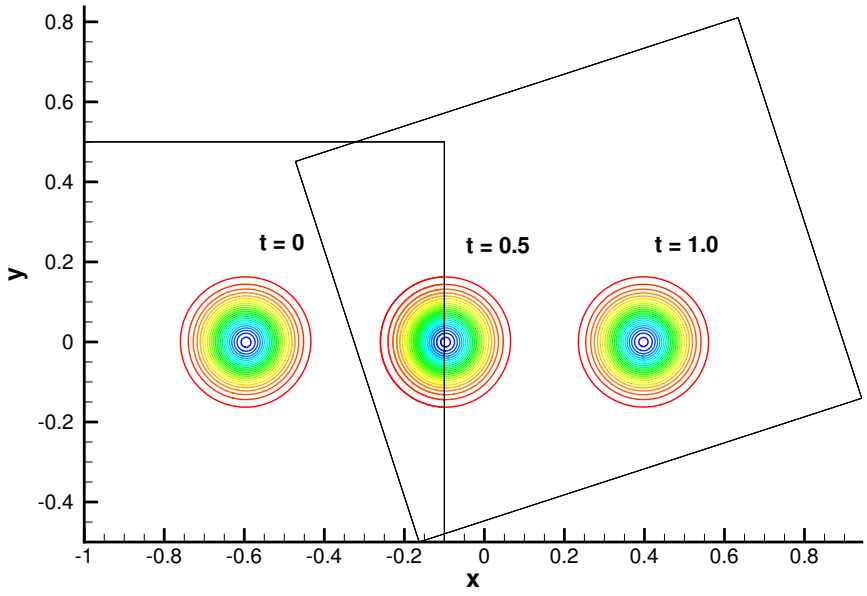

Figure 4.11: Contours of density showing convection of vortex over time on the rotated grid configuration.

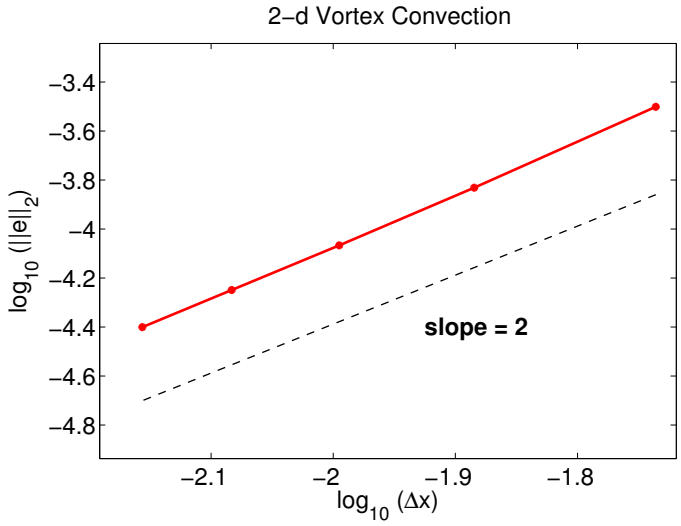

Figure 4.12: Convergence of method (4.34) with $1-2-1$ SBP operator at $t_f = 0.5$, on the rotated grid configuration shown in Figure 4.11, with a grid spacing ratio of $2:3$ between left and right grids in each direction and $\triangle x = \triangle x_L$.

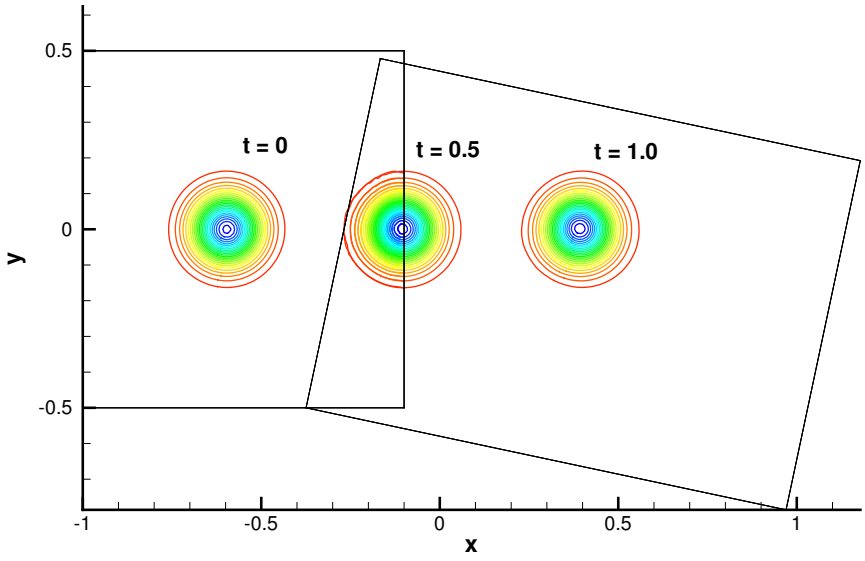

Figure 4.13: Contours of density showing convection of vortex over time on the rotated grid configuration.

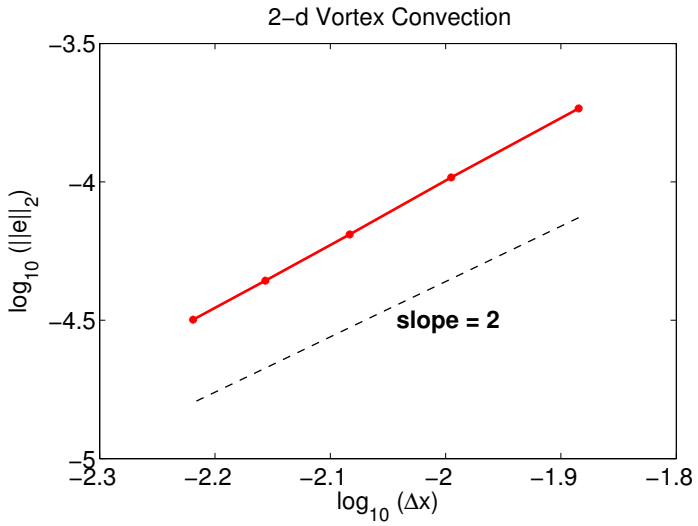

Figure 4.14: Convergence of method (4.34) with $1-2-1$ SBP operator at $t_f = 0.5$, on the rotated grid configuration shown in Figure 4.13, with a grid spacing ratio of $2:3$ between left and right grids in each directions and $\triangle x = \triangle x_L$.

Grid Configuration-2

The above numerical tests examined the robustness of the overset method proposed in Section 4.1.2 for 1-D and 2-D, linear and non-linear problems. But in all the previous cases we considered two-grid configurations with BCs that allowed the Gaussian pulse or the vortex to cross over the interface just once, which is not

sufficient to assess the long-time behavior of the interface treatment. Therefore, in this section, we consider a computational domain as shown in Figure 4.15, the grid for which is shown in Figure 4.16. The base Cartesian grid of size 201×201, shown in black in Figure 4.16, has a rectangular hole that is covered by a square patch (rotated Cartesian grid) of size 101×101 shown in red. The square patch is aligned at an angle θ with respect to the base Cartesian grid and its dimension for different values of θ are listed in Table 4.3. The hole on the base grid is created by blanking out a set of grid points denoted by $[i_s, i_e] \times [j_s, j_e]$ in Table 4.3.

θ	Patch side length (L)	Hole indices $[i_s, i_e] \times [j_s, j_e]$
0	0.76	$[68, 134] \times [30, 172]$
$\pi/12$	0.76	$[75, 127] \times [49, 154]$
$\pi/8$	0.68	$[80, 123] \times [62, 141]$
$\pi/6$	0.68	$[78, 125] \times [66, 137]$
$\pi/4$	0.64	$[84, 119] \times [61, 142]$

Table 4.3: Grid specifications for different values of θ in Figure 4.16. $[i_s, i_e]$ denotes the range of grid point indices in the x-direction that are blanked out and, similarly, $[j_s, j_e]$ denotes the range of blanked out indices in the y-direction. Note that $1 \leq i, j \leq 201$ for the base grid.

The solution on the base grid is assumed to be periodic in x-direction to let the vortex cross over the patch as many times as desired. We use $u_0 = 2$ in Eq. (4.33) to compute the convection of vortex over time. The initial condition is shown in Figure 4.17. The norm of density error, using Eq. (4.36), for time $0 \leq t_f \leq 4$ is shown in Figure 4.18 for different values of θ. The error profile is approximately the same for different values of θ in Figure 4.18 therefore the method is not sensitive to the orientation of the grids.

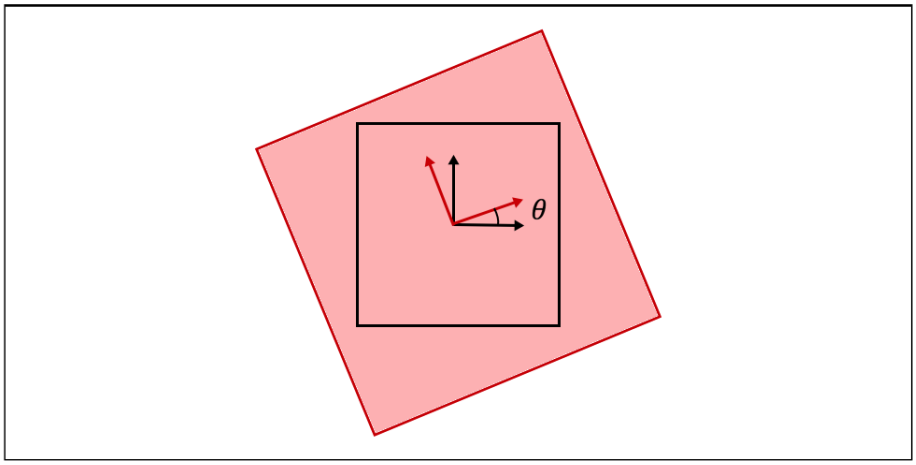

Figure 4.15: Overset grid configuration with a base and a patch grid. The patch grid shaded in red is rotated at an angle θ with respect to the base grid.

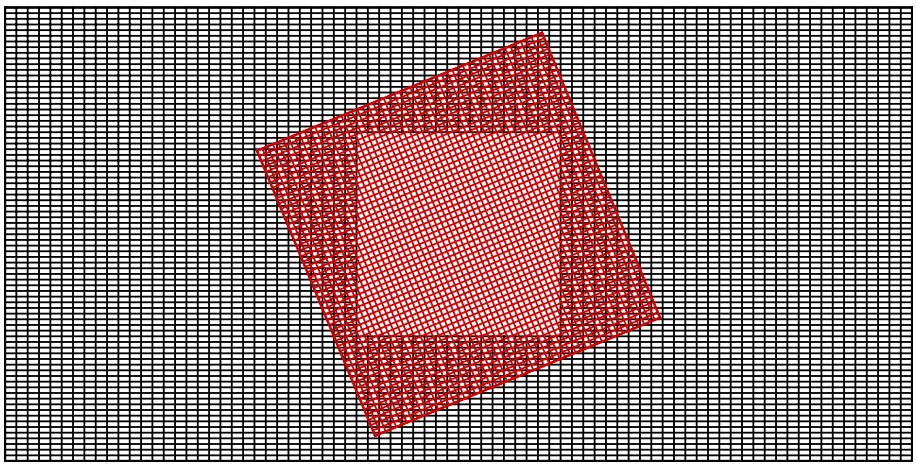

Figure 4.16: Grid for the overset configuration shown in Figure 4.15.

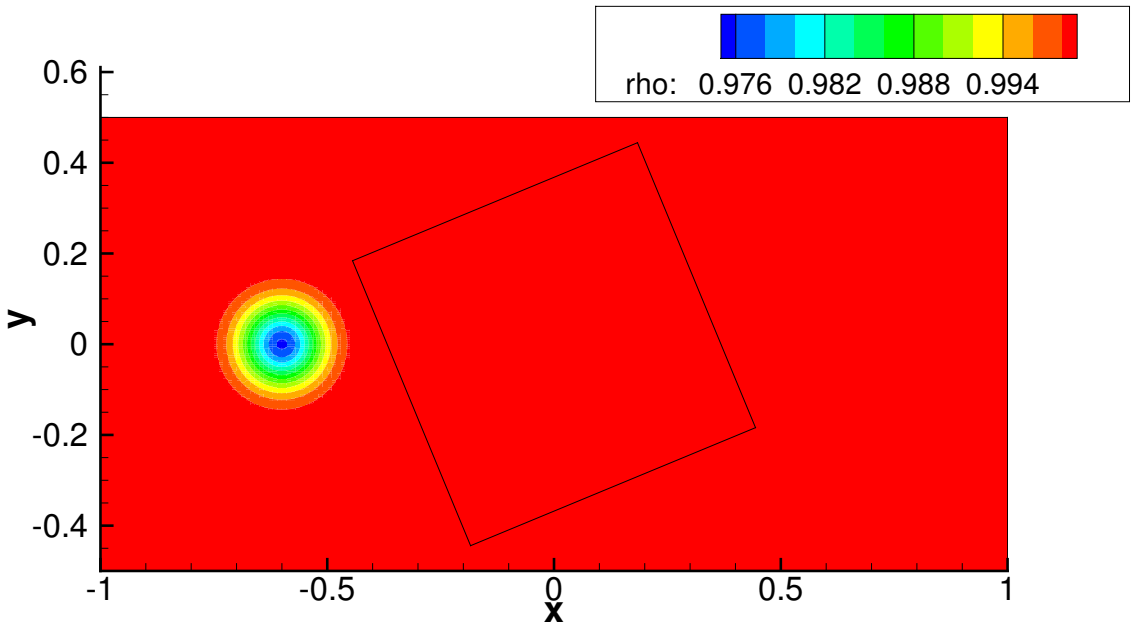

Figure 4.17: Initial condition on the grid configuration shown in Figure 4.15.

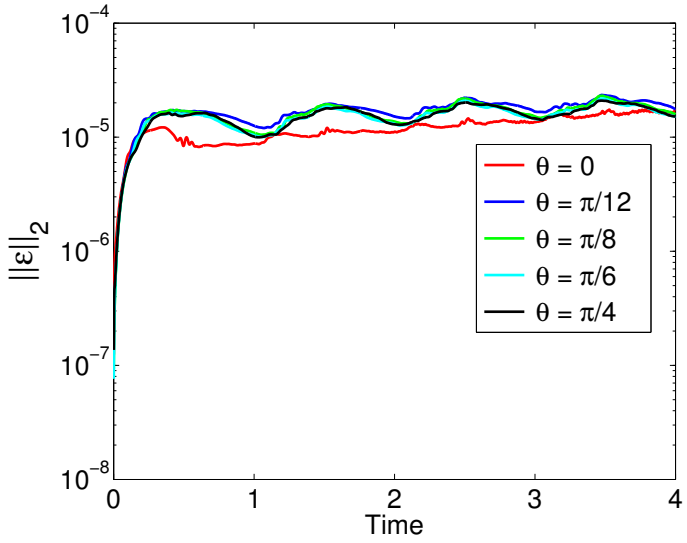

Figure 4.18: Norm of the density error with time for different values of θ (see Figure 4.15), using $2-4-2$ SBP operator with cubic interpolation.

Figure 4.19 compares the long-time performance of the method (4.34)–(4.35), hereafter referred to as the SAT method, against the "injection method" for $\theta = \frac{\pi}{4}$ (see Figure 4.15) using the third-order scheme. The "injection method" is the most commonly used approach of interface treatment for overset grids where the computed solution at the interface grid points are overwritten by the interpolated value from the underlying grid at each time (sub-)step. Figures 4.20 and 4.21 compare, for supersonic and subsonic convective speed

respectively, the L_2-error with time between the SAT method and the "injection method". The vortex flow specifications were same as that used to obtain Figure (4.18). The SAT method clearly produces lower error, but more importantly the error does not grow exponentially in time as the results from the injection method.

Table 4.4 shows the convergence of the method with $1-2-1$, $2-4-2$ and $3-6-3$ SBP difference approximation with $\|\mathbf{e}\|_2$ given by Eq. (4.36). Linear Lagrange interpolation was used at the interface with $1-2-1$ operator and cubic Lagrange interpolation with $2-4-2$ and $3-6-3$ operators. The error was computed for subsequent refinements with $N = n_x^1 = n_y^1 = n_x^2 = n_y^2$ at $t_f = 1.0$ with a constant CFL of 0.5, 0.25 and 0.15 for $1-2-1$, $2-4-2$ and $3-6-3$ operators respectively.

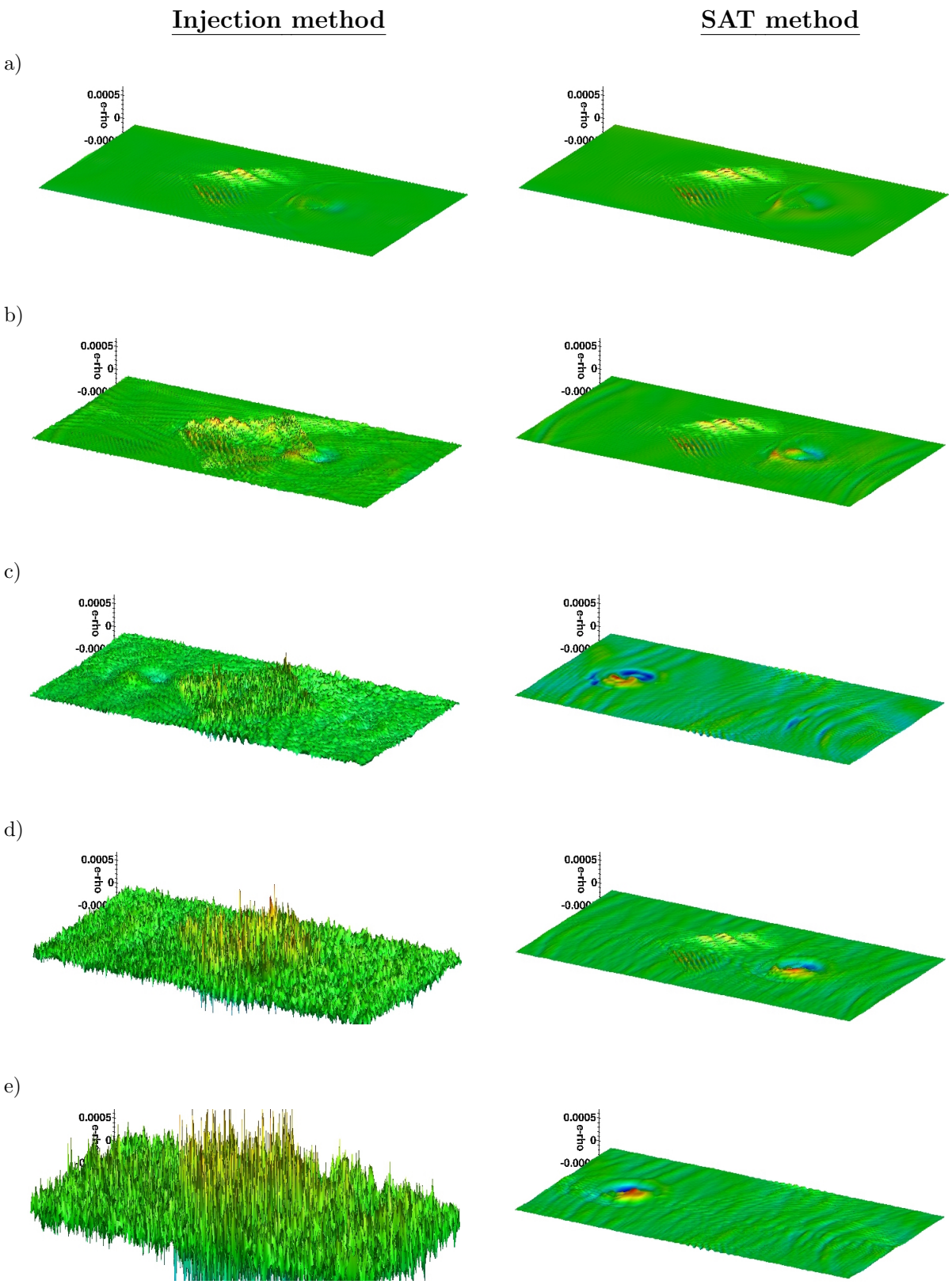

Figure 4.19: Surface plots for the density error comparison between the injection method and the SAT method. The plots show the error at the following times: a) $t = 0.5$, b) $t = 1.5$, c) $t = 3.0$, d) $t = 5.5$, e) $t = 8.0$.

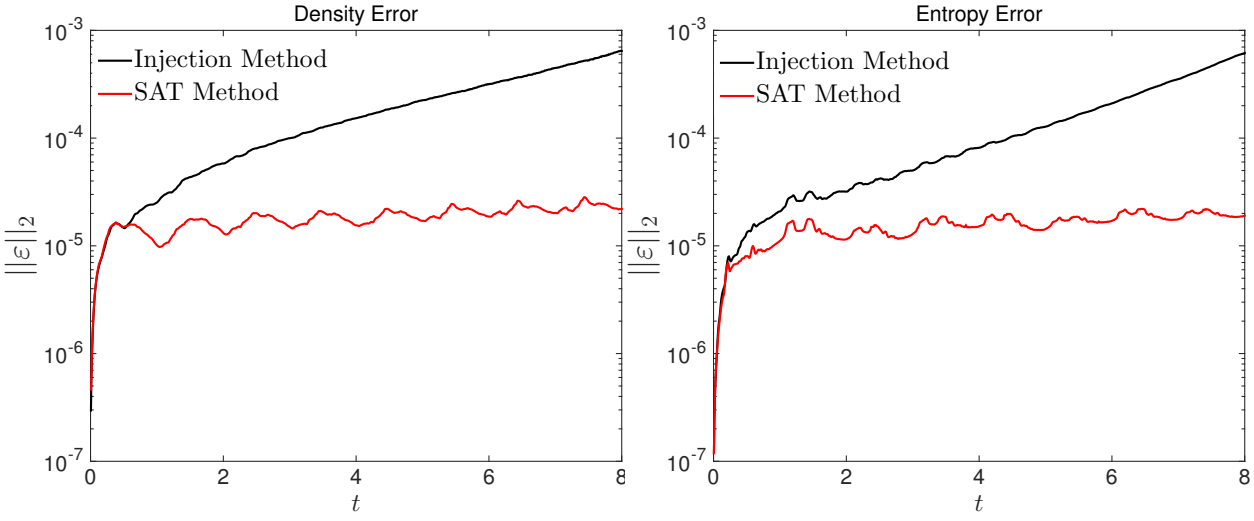

(a)

(b)

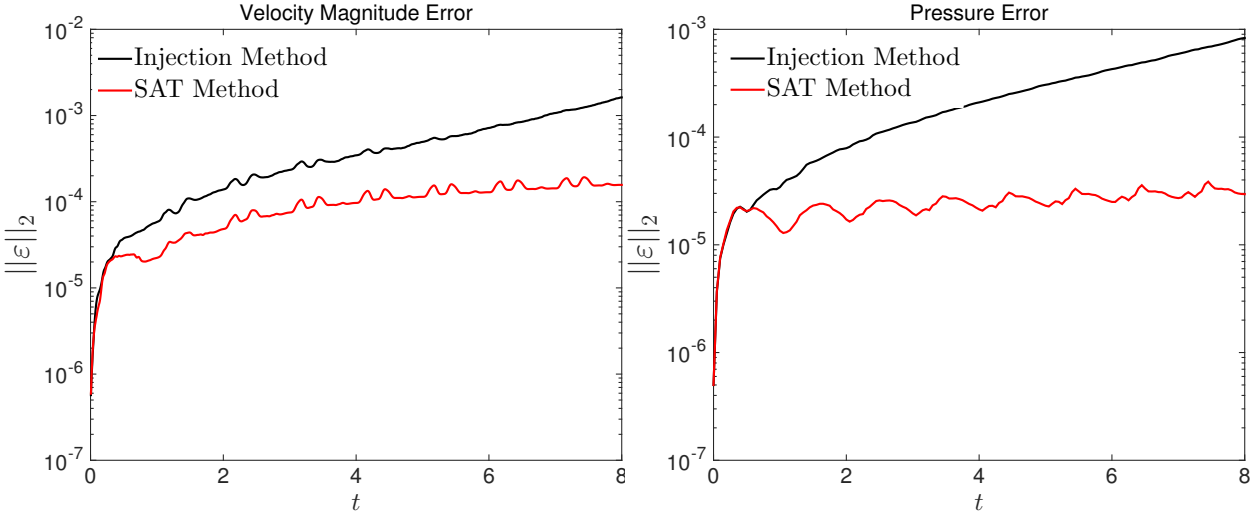

(c)

(d)

Figure 4.20: Error comparison of the injection method against the SAT method for $u_0 = 2.0$. (a) Density error, (b) Entropy error, (c) Velocity magnitude error, (d) Pressure error.

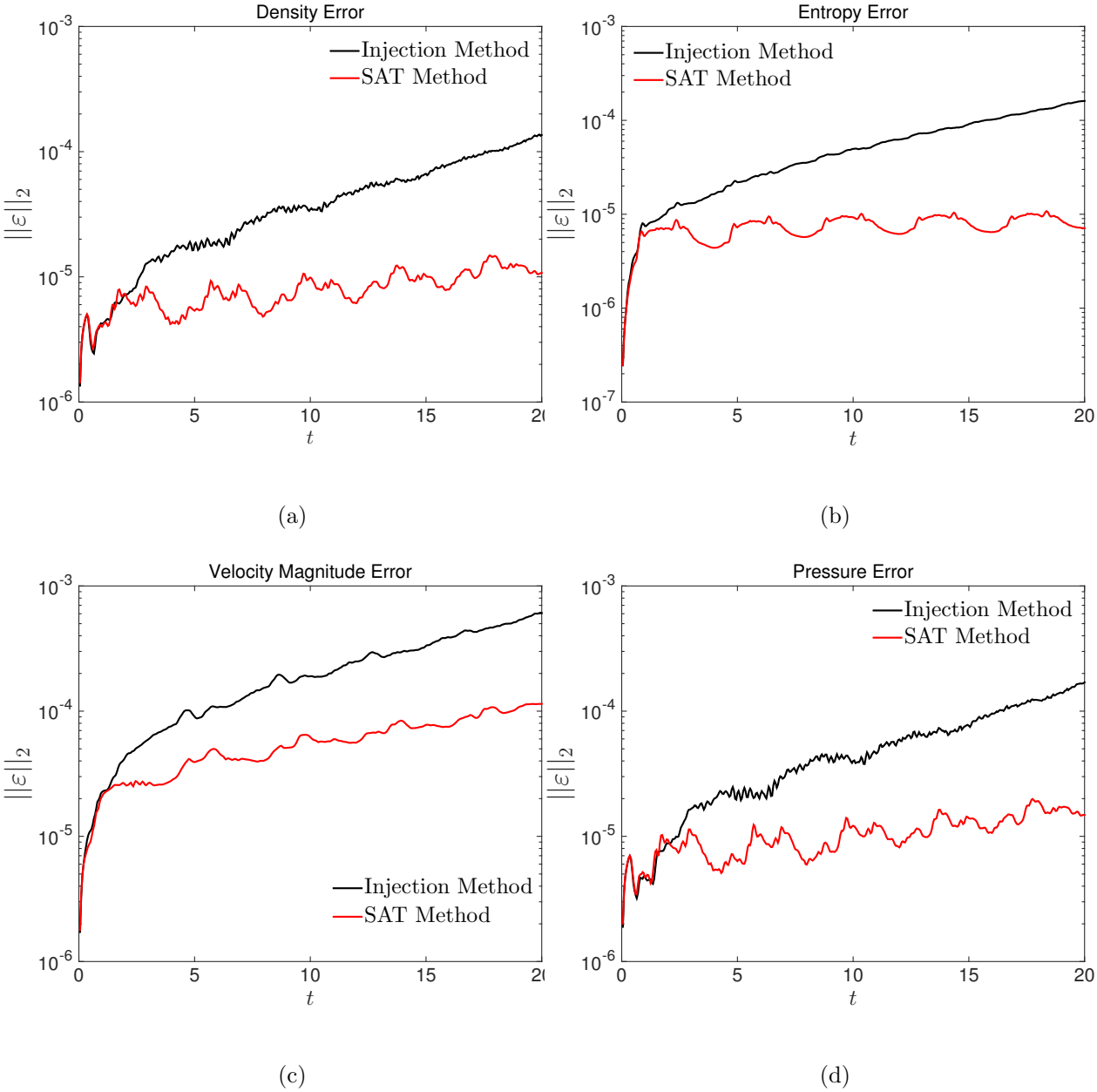

Figure 4.21: Error comparison of the injection method against the SAT method for $u_0 = 0.5$. (a) Density error, (b) Entropy error, (c) Velocity magnitude error, (d) Pressure error.

	$1-2-1$		$2-4-2$		$3-6-3$	
N	$\log_{10}\|\mathbf{e}\|_2$	Rate	$\log_{10}\|\mathbf{e}\|_2$	Rate	$\log_{10}\|\mathbf{e}\|_2$	Rate
50	-2.551		-3.011		-2.970	
100	-3.009	1.501	-3.935	3.028	-3.895	3.029
150	-3.359	1.971	-4.516	3.271	-4.534	3.601
200	-3.615	2.044	-4.955	3.492	-5.054	4.134

Table 4.4: Convergence, for different SBP first derivative approximations, of the SAT method for the grid configuration shown in Figure 4.15 with $\theta = \frac{\pi}{4}$. The density error $\|\mathbf{e}\|_2$ is given by Eq. (4.36).

4.3.4 Cyclic Hyperbolic System

To prove time-stability of the method (4.6) and (4.7) we analyzed the system matrix M and showed stability in terms of its eigenvalues. This approach was successful since we had system matrices in a block lower- or block upper-triangular form, whose eigenvalues could be estimated from the diagonal blocks. For problems, such as that discussed next, where the system matrix is not of a block lower- or block upper-triangular form the approach discussed in chapter 4 does not lead to a time-stable scheme.

Consider the hyperbolic system discussed in (Carpenter *et al.*, 1994, Section 3),

$$\frac{\partial u}{\partial t} + A\frac{\partial u}{\partial x} = 0, \tag{4.37}$$

where

$$u = \begin{bmatrix} u_1 \\ u_2 \end{bmatrix}, \qquad A = \begin{bmatrix} 1 & 0 \\ 0 & -1 \end{bmatrix},$$

on the domain $x \in [0,1]$ with the initial and the boundary conditions given by

$$u_1(x,0) = \sin 2\pi x, \qquad u_2(x,0) = -\sin 2\pi x,$$

$$u_1(0,t) = u_2(0,t), \qquad u_2(1,t) = u_1(1,t). \tag{4.38}$$

The exact solution for the problem is $u_1(x,t) = \sin\, 2\pi(x-t)$ and $u_2(x,t) = -\sin\, 2\pi(x+t)$. Let the domain $x \in [0,1]$ be comprised of two overlapping subdomains, $x_L \in [0,\, b_L]$ and $x_R \in [a_R, 1]$. Denote the grid function on the left and the right subdomain by $\mathbf{u} = \begin{bmatrix} \mathbf{u}_1 & \mathbf{u}_2 \end{bmatrix}^T$ and $\mathbf{v} = \begin{bmatrix} \mathbf{v}_1 & \mathbf{v}_2 \end{bmatrix}^T$ respectively. The

semidiscrete approximation of (4.37)-(4.38) can be written as

$$\frac{d\mathbf{w}}{dt} = M\mathbf{w}, \tag{4.39}$$

where $\mathbf{w} = \begin{bmatrix} \mathbf{w}_1 & \mathbf{w}_2 \end{bmatrix}^T$ with $\mathbf{w}_1 = \begin{bmatrix} \mathbf{u}_1 & \mathbf{v}_1 \end{bmatrix}$ and $\mathbf{w}_2 = \begin{bmatrix} \mathbf{u}_2 & \mathbf{v}_2 \end{bmatrix}$, and

$$M = \begin{bmatrix} M_{11} & M_{12} \\ M_{21} & M_{22} \end{bmatrix},$$

$$M_{11} = \begin{bmatrix} -P_L^{-1}Q_L - \tau_L P_L^{-1} E_0^L & 0 \\ \\ \tau_R P_R^{-1} e_0^R T_L^T & -P_R^{-1}Q_R - \tau_R P_R^{-1} E_0^R \end{bmatrix}, \quad M_{12} = \begin{bmatrix} \tau_L P_L^{-1} E_0^L & 0 \\ \\ 0 & 0 \end{bmatrix}, \tag{4.40}$$

$$M_{21} = \begin{bmatrix} 0 & 0 \\ \\ 0 & \tau_R P_R^{-1} E_n^R \end{bmatrix}, \quad M_{22} = \begin{bmatrix} P_L^{-1}Q_L - \tau_L P_L^{-1} E_m^L & \tau_L P_L^{-1} e_m^L T_R^T \\ \\ 0 & P_R^{-1}Q_R - \tau_R P_R^{-1} E_n^R \end{bmatrix},$$

where E_0^L and E_0^R are given by Eq. (4.9), and

$$E_m^L = e_m^L (e_m^L)^T, \qquad E_n^R = e_n^R (e_n^R)^T.$$

$e_m^L = \begin{bmatrix} 0 & \cdots & 1 \end{bmatrix}^T$ is a vector of size $m+1$ and $e_n^L = \begin{bmatrix} 0 & \cdots & 1 \end{bmatrix}^T$ is a vector of size $n+1$. T_L and T_R denote the vectors with interpolation coefficients such that the numerical boundary conditions at the interface are given by (see Figure 4.22),

$$(\hat{\mathbf{v}}_1)_0 = T_L^T \mathbf{u}_1,$$

$$(\hat{\mathbf{u}}_2)_m = T_R^T \mathbf{v}_2.$$

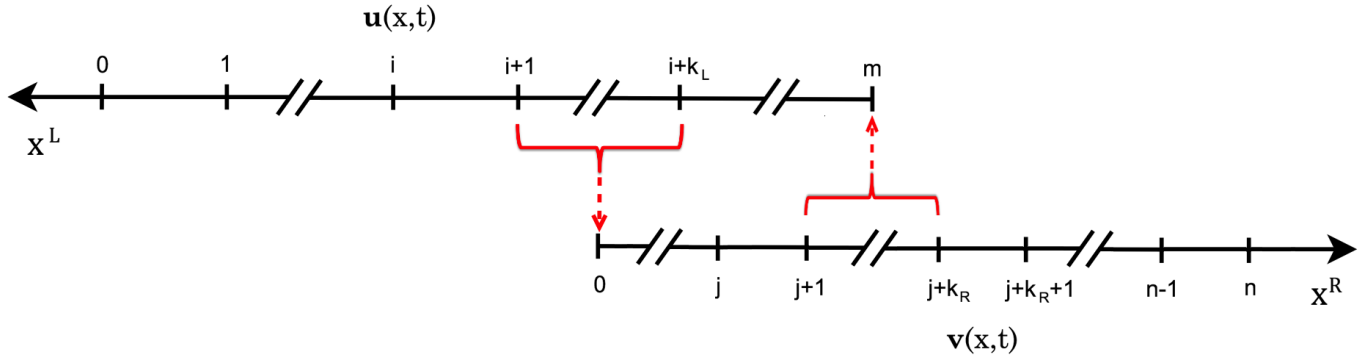

Figure 4.22: Schematic diagram of overlapping grids on which Eq. (4.37)-(4.38) is solved. The red arrow denotes the interpolation.

Figure 4.23 shows the eigenvalues of the system matrix M for 60 grid points on the left domain and 30 on the right with $1-2-1$ SBP first derivative approximation, linear Lagrange interpolation and $a_R = \frac{1}{2} - \frac{h_L}{2}$, $b_L = \frac{1}{2}$. The maximum real part among all eigenvalues is 0.0107 which implies that the method (4.39) is not time-stable for this problem. For large times, the eigenvalues with positive real part will dominate the solution resulting in an exponential growth.

The system matrix, in this case, does not have a block lower- or a block upper-triangular structure and, therefore, estimating the sign of the real part of the eigenvalue is not straight-forward. Without the knowledge of the eigenvalues, it is difficult to comment whether a different value of τ_L or τ_R, or a matrix other than $P_{L,R}$ in the SAT implementation would yield a time-stable scheme. Lemma 3.3 can, therefore, be used only in limited number of cases. In the next chapter, we discuss the second case of the method which uses the energy method and Lemma 3.1 to prove time-stability on the overset grids for all problems that have a bounded energy norm. In anticipation of the upcoming results, Figure 4.24 shows for the above problem the eigenvalue spectrum of the system matrix from the method discussed in the next chapter. The maximum real part among all eigenvalues is less than zero in Figure 4.24 indicating a time-stable behavior.

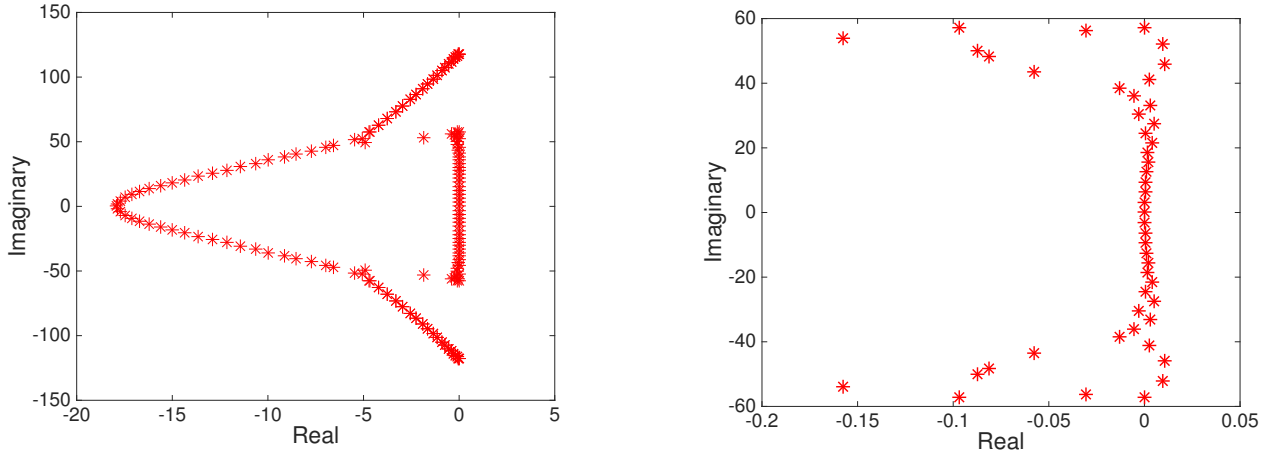

(a) (b)

Figure 4.23: Eigenvalues of the system matrix M from the method (4.39). (a) All eigenvalues. (b) Magnified view near the imaginary axis. $\text{Max}(\text{Re}(\lambda_i)) = 0.0107$.

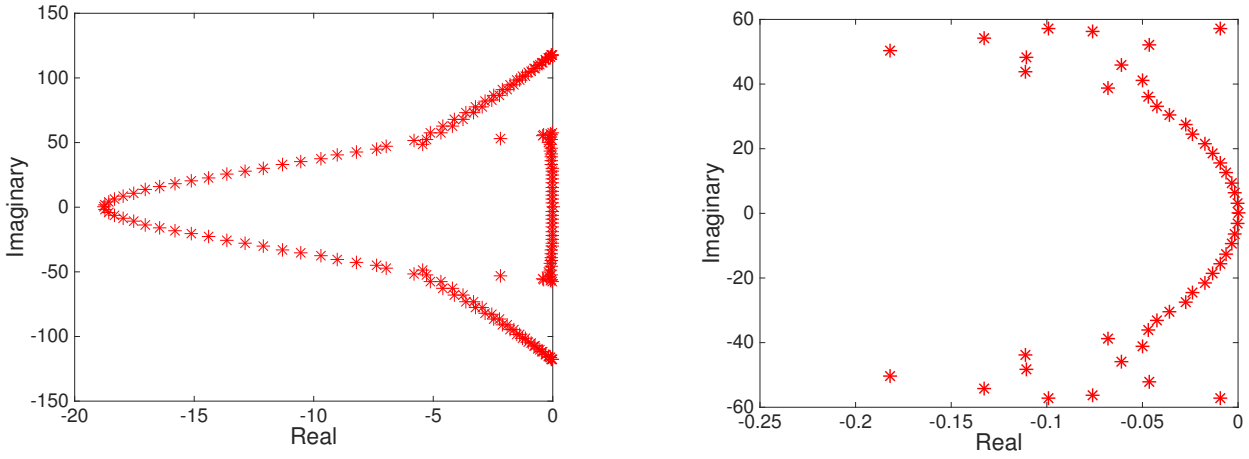

(a) (b)

Figure 4.24: Eigenvalues of the system matrix from the method discussed in Chapter 5. (a) All eigenvalues. (b) Magnified view near the imaginary axis. $\text{Max}(Re(\lambda_i)) = -6.7347 \times 10^{-15}$.

Chapter 5

Stable Overset Methods for Hyperbolic Problems - II

In this chapter, we discuss the same method as the previous chapter but with a localized dissipation term that allows the use of energy method for proof of stability. Like in the previous chapter, we will first discuss the proof of stability for a scalar problem before analyzing the extension to the Euler equations.

5.1 The Scalar Problem

We consider the simple advection equation (4.1) with the initial and the boundary condition given by (4.2) and (4.3) respectively.

5.1.1 Numerical Scheme

For the overlapping grid configuration and the numerical boundary condition discussed in Section 4.1.1 the proposed semidiscrete approximation for the left and the right subdomains is given by,

$$\frac{\mathrm{d}\mathbf{u}}{\mathrm{d}t} = -P_L^{-1}Q_L\mathbf{u} - \tau_L S_L(u_0 - g) + \Upsilon_L\mathbf{u}, \tag{5.1}$$

$$\frac{\mathrm{d}\mathbf{v}}{\mathrm{d}t} = -P_R^{-1}Q_R\mathbf{v} - \tau_R S_R(v_0 - \hat{v}_0), \tag{5.2}$$

$$S_{L,R} = H_{L,R}^{-1}e_0^{L,R}, \qquad e_0^{L,R} = [1\,0\,\ldots\,0]^T, \tag{5.3}$$

where the vectors e_0^L and e_0^R are of sizes $(m+1)$ and $(n+1)$ respectively. Υ_L in (4.6) denotes a dissipative operator whose exact structure will be determined from the stability analysis. The reason the dissipation term appears only on the discretization for the upwind domain will become clear once we examine the stability of the method. H_L and H_R constitute a norm matrix H given by

$$H = \begin{bmatrix} H_L & \\ & H_R \end{bmatrix}, \quad H_L = C_L P_L, \quad H_R = C_R P_R, \tag{5.4}$$

where $C_L = \text{diag}(c_0^L, \ ..... \ , c_m^L)$ with $c_i^L > 0$ for all i, and $C_R = \beta_R I_R$ where I_R denotes an identity matrix of size $(n+1) \times (n+1)$, and $\beta_R > 0$ is a scalar constant.

For time-stability it is sufficient to consider the case with $g(t) = 0$. Applying the energy method to (5.1)–(5.2), with $g = 0$, using the H norm yields

$$\frac{\mathrm{d}}{\mathrm{d}t}||\mathbf{u}||_{H_L}^2 = -\mathbf{u}^T(C_L Q_L + (C_L Q_L)^T)\mathbf{u} - 2\tau_L u_0^2 + 2\mathbf{u}^T(H_L \Upsilon_L + (H_L \Upsilon_L)^T)\mathbf{u}, \tag{5.5}$$

$$\frac{\mathrm{d}}{\mathrm{d}t}||\mathbf{v}||_{H_R}^2 = -\beta_R \mathbf{v}^T(Q_R + Q_R^T)\mathbf{v} - 2\tau_R v_0^2 + 2\tau_R(\mathbf{v}^T e_0^R)T_L^T \mathbf{u}. \tag{5.6}$$

The above equations can be collectively written as

$$\frac{\mathrm{d}}{\mathrm{d}t}||\mathbf{w}||_H^2 = \frac{\mathrm{d}}{\mathrm{d}t}||\mathbf{u}||_{H_L}^2 + \frac{\mathrm{d}}{\mathrm{d}t}||\mathbf{v}||_{H_R}^2, \tag{5.7}$$

where $\mathbf{w} = \begin{bmatrix} \mathbf{u} & \mathbf{v} \end{bmatrix}^T$. To prove time-stability, we need to show that $\frac{\mathrm{d}}{\mathrm{d}t}||\mathbf{w}||_H^2 \leq 0$. Since (5.7) involves T_L, which contains the interpolation coefficients and the information about the location of donor points, the proof of stability will depend on the interpolation method used and the amount of overlap between the grids. We will have to proceed on a case-by-case basis for different orders of the first derivative approximation and the overlap position. The overlap positions will be classified as:

- Interior overlap - if all the donor points for interpolation are the interior points
- Boundary overlap - if at least one donor point is a boundary point.

In this chapter, we use Lagrange interpolation for all the proofs; a similar approach may be used with other interpolation bases.

5.1.2 Stability of the Second-Order Scheme

In this section, we provide the proof of time-stability for the second-order accurate scheme of the method (5.1)–(5.2), for which the operator $P^{-1}Q$ denotes the $1-2-1$ SBP first derivative approximation. Linear interpolation ($k = 2$ in Eq. (4.5)) is used to retain the second order of accuracy globally. We choose the dissipative operator Υ_L of the form

$$\Upsilon_L = \Gamma_L R_L, \tag{5.8}$$

where $\Gamma_L = \text{diag}(\gamma_0, \gamma_1, \ ..... \ , \gamma_m)$ and R_L is an approximation of $h_L \frac{\partial^2 u}{\partial x^2}$ given by

$$R_L = \frac{1}{h_L}\begin{bmatrix} 1 & -2 & 1 & & & \\ 1 & -2 & 1 & & & \\ & \ddots & \ddots & \ddots & & \\ & & \ddots & \ddots & \ddots & \\ & & & 1 & -2 & 1 \\ & & & 1 & -2 & 1 \end{bmatrix}. \tag{5.9}$$

The non-zero entries of the diagonal matrix Γ_L will determine the grid points where the dissipation is added as well as the weight of the dissipation term for each grid point. In all cases, the term would be active only at the donor grid points. The dissipation term upwinds the difference stencil at the donor points with γ_i (in matrix Γ_L) denoting the amount of upwinding influence at the i-th grid point.

Boundary Overlap

First we discuss the scenario where the left-most grid point on the right grid (x_0^R) lies between the two right-most grid points of the left domain (i.e. x_{m-1}^L and x_m^L) as shown in Figure 5.1. Therefore the numerical boundary condition at x_0^R, using the Lagrange interpolation, is given by

$$\hat{v}_0 = T_L^T \mathbf{u} = \alpha_L u_{m-1} + (1-\alpha_L) u_m, \tag{5.10}$$

$$T_L = [0 \ldots . 0 \;\; \alpha_L \;\; (1-\alpha_L)]^T, \tag{5.11}$$

where T_L is a vector of size $(m+1)$.

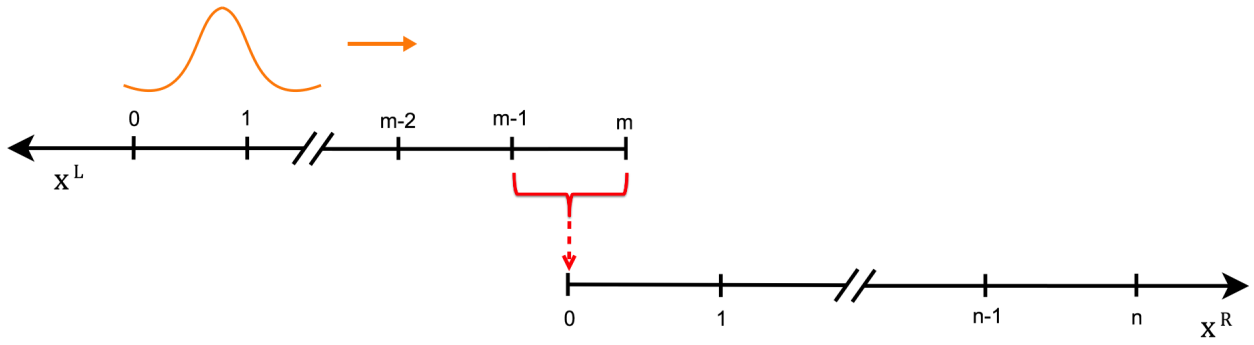

Figure 5.1: Schematic diagram of overlapping grids for linear interpolation.

Our aim is to determine the values of the parameters τ_L, τ_R, C_L, Γ_L and β_R for $\alpha_L \in [0,1]$ such that

$\frac{\mathrm{d}}{\mathrm{d}t}||\mathbf{w}||_H^2 \leq 0$ (see Eq. (5.7)).

Theorem 5.1 *The method (5.1)–(5.2) for the overlapping grid configuration shown in Figure 5.1 with the* $1-2-1$ *SBP first derivative approximation, linear Lagrangian interpolation and a dissipative operator given by Eqs. (5.8)–(5.9) is time-stable if*

$$\tau_L \geq \frac{1}{2}, \qquad \beta_R = \frac{8q}{(1+2q)^2}, \qquad \tau_R = \beta_R\left(\frac{1}{2}+q\right),$$

$$c_0^L = c_1^L = ... = c_{m-2}^L = 1, \qquad c_{m-1}^L = 1 - \frac{\epsilon + \alpha_L^2}{2}, \qquad c_m^L = \epsilon + (1-\alpha_L)^2, \tag{5.12}$$

$$\Gamma_L = \mathrm{diag}\left(0, \cdots, 0, \frac{1-c_{m-1}^L}{2c_{m-1}^L}, 0\right),$$

for all values of $q > 0$ *and* $0 \leq \epsilon < 1$.

Proof. Consider $C_L = \mathrm{diag}(1, \cdots, 1, c_{m-1}^L, c_m^L)$ and $\Gamma_L = \mathrm{diag}(0, ..., 0, \gamma, 0)$. Substituting them in (5.7) using (5.9), (5.11) and the $1-2-1$ SBP first derivative approximation yields

$$\frac{\mathrm{d}}{\mathrm{d}t}||\mathbf{w}||_H^2 = -[1-(1+2\gamma)c_{m-1}^L]u_{m-2}u_{m-1} - 4\gamma c_{m-1}^L u_{m-1}^2 - [(1-2\gamma)c_{m-1}^L - c_m^L]u_m u_{m-1} - c_m^L u_m^2$$

$$+ 2\tau_R\alpha_L v_0 u_{m-1} + 2\tau_R(1-\alpha_L)v_0 u_m + (\beta_R - 2\tau_R)v_0^2 + (1-2\tau_L)u_0^2 - \beta_R v_n^2. \tag{5.13}$$

If we take,

$$\mathbf{s} = [u_{m-2} \quad u_{m-1} \quad u_m \quad v_0]^T, \qquad \tau_L \geq \tfrac{1}{2},$$

Eq. (5.13) yields,

$$\frac{\mathrm{d}}{\mathrm{d}t}||\mathbf{w}||_H^2 \quad \leq$$

$$\mathbf{s}^T \begin{bmatrix} 0 & -\frac{1}{2}(1-(1+2\gamma)c_{m-1}^L) & 0 & 0 \\ -\frac{1}{2}(1-(1+2\gamma)c_{m-1}^L) & -4\gamma c_{m-1}^L & -\frac{1}{2}((1-2\gamma)c_{m-1}^L - c_m^L) & \tau_R\alpha_L \\ 0 & -\frac{1}{2}((1-2\gamma)c_{m-1}^L - c_m^L) & -c_m^L & \tau_R(1-\alpha_L) \\ 0 & \tau_R\alpha_L & \tau_R(1-\alpha_L) & \beta_R - 2\tau_R \end{bmatrix} \mathbf{s}. \tag{5.14}$$

Choosing $\gamma = \frac{1-c^L_{m-1}}{2c^L_{m-1}}$ to cancel the (1, 2) and (2, 1) entries, proving stability requires we show that

$$K = \begin{bmatrix} -2(1-c^L_{m-1}) & -\frac{1}{2}(2c^L_{m-1} - c^L_m - 1) & \tau_R\alpha_L \\ -\frac{1}{2}(2c^L_{m-1} - c^L_m - 1) & -c^L_m & \tau_R(1-\alpha_L) \\ \tau_R\alpha_L & \tau_R(1-\alpha_L) & \beta_R - 2\tau_R \end{bmatrix} \leq 0, \tag{5.15}$$

i.e., that the matrix K should be negative semi-definite. That is true if all principal minors, $\triangle_k$ of order $k = 1, 2, 3$, obey $(-1)^k\triangle_k \geq 0$. From first-order principal minors we have

$$1 - c^L_{m-1} \geq 0, \quad c^L_m \geq 0, \quad \tau_R \geq \frac{\beta_R}{2}. \tag{5.16}$$

Therefore, let us introduce a change of variables

$$c^L_{m-1} = 1 - x, \quad c^L_m = 2y, \quad \tau_R = \frac{\beta_R}{2} + \beta_R q, \tag{5.17}$$

where x, y and q are non-negative numbers, and $c^L_{m-1} > 0$ implies $x < 1$. Inserting (5.17) in (5.15) yields

$$K = \begin{bmatrix} -2x & x + y - \frac{1}{2} & \beta_R(\frac{1}{2} + q)\alpha_L \\ x + y - \frac{1}{2} & -2y & \beta_R(\frac{1}{2} + q)(1-\alpha_L) \\ \beta_R(\frac{1}{2} + q)\alpha_L & \beta_R(\frac{1}{2} + q)(1-\alpha_L) & -2\beta_R q \end{bmatrix}. \tag{5.18}$$

The second-order principal minors give the following three conditions:

$$(x-y)^2 - (x+y) + \frac{1}{4} \leq 0, \tag{5.19}$$

$$4xq - \beta_R\left(\frac{1}{2} + q\right)^2 \alpha_L^2 \geq 0, \tag{5.20}$$

$$4yq - \beta_R\left(\frac{1}{2} + q\right)^2 (1-\alpha_L)^2 \geq 0, \tag{5.21}$$

If we assume $x = \frac{\theta+\eta}{2}$ and $y = \frac{\theta-\eta}{2}$, (5.19) gives $\theta \geq \eta^2 + \frac{1}{4}$, or

$$\theta = \epsilon + \eta^2 + \frac{1}{4}, \qquad \text{for} \quad \epsilon \geq 0. \tag{5.22}$$

Therefore, $\theta = \eta^2 + \frac{1}{4}$ or, $x = \frac{\eta^2+\eta+\frac{1}{4}}{2}$ and $y = \frac{\eta^2-\eta+\frac{1}{4}}{2}$ represent the boundary (in the x-y plane) of the solution required for numerical stability. The shaded region in Figure 5.2 shows the admissible values of x

and y.

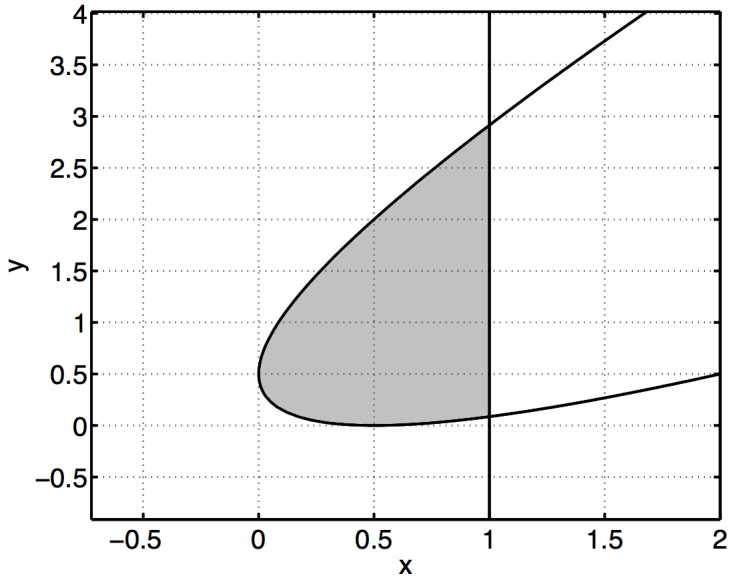

Figure 5.2: Shaded region shows the admissible values of x and y for $\det(K_{2\times 2}) \geq 0$.

Two cases exist for the conditions from the other two second-order principal minors, Eqs. (5.20) and (5.21),

Case 1: $q = 0$

Setting $q = 0$ in Eq. (5.20) and (5.21) yields $\frac{\beta_R}{4}\alpha_L^2 \leq 0$ and $\frac{\beta_R}{4}(1-\alpha_L)^2 \leq 0$ respectively. Since $\beta_R > 0$ and the inequality must hold for all values of $\alpha_L \in [0,1]$, q cannot equal zero.

Case 2: $q > 0$

Eqs. (5.20) and (5.21) yield, respectively,

$$x \geq \frac{\beta_R}{4}\left(\frac{1}{2\sqrt{q}} + \sqrt{q}\right)^2 \alpha_L^2, \qquad y \geq \frac{\beta_R}{4}\left(\frac{1}{2\sqrt{q}} + \sqrt{q}\right)^2 (1-\alpha_L)^2. \tag{5.23}$$

Now, the condition on third order principal minor implies,

$$\triangle_3 \leq 0 \Rightarrow -8q\epsilon + \beta_R(1+2q)^2\left\{\alpha_L^2 + \epsilon - \alpha_L(1+2\eta) + \frac{(1+2\eta)^2}{4}\right\} \leq 0. \tag{5.24}$$

Rearranging (5.24) gives

$$\epsilon\left(1 - \frac{8q}{\beta_R(1+2q)^2}\right) + f(\alpha_L) \leq 0, \tag{5.25}$$

where,

$$f(\alpha_L) = \alpha_L^2 - \alpha_L(1+2\eta) + \tfrac{(1+2\eta)^2}{4} = (\alpha_L - \tfrac{1+2\eta}{2})^2.$$

Three cases exist for Eq. (5.25):

Sub-case 1: $1 - \frac{8q}{\beta_R(1+2q)^2} > 0$

Eq. (5.25) gives

$$\epsilon \leq \frac{-f(\alpha_L)}{\left(1 - \frac{8q}{\beta_R(1+2q)^2}\right)}.$$

Since $f(\alpha_L) \geq 0$ and $\epsilon \geq 0$, this case will not provide an allowable value of ϵ.

Sub-case 2: $1 - \frac{8q}{\beta_R(1+2q)^2} = 0$

Eq. (5.25) provides

$$f(\alpha_L) = 0 \Rightarrow \eta = \alpha_L - \frac{1}{2}.$$

Eq. (5.23) results in

$$x \geq \frac{\alpha_L^2}{2}, \qquad y \geq \frac{(1-\alpha_L)^2}{2}.$$

Therefore, for all admissible values of q (i.e., $q > 0$),

$$\beta_R = \frac{8q}{(1+2q)^2}, \qquad x = \frac{\epsilon + \alpha_L^2}{2}, \qquad y = \frac{\epsilon + (1-\alpha_L)^2}{2}, \tag{5.26}$$

for $0 \leq \epsilon < 1$, since $x < 1$. Inserting x and y in Eq. (5.17) completes the proof. □

The third Sub-case, $1 - \frac{8q}{\beta_R(1+2q)^2} < 0$, provides additional solutions as Eq. (5.25) for this case yields

$$\epsilon \geq \frac{f(\alpha_L)}{\left(\frac{8q}{\beta_R(1+2q)^2} - 1\right)},$$

where $f(\alpha_L) = \left(\alpha_L - \frac{1+2\eta}{2}\right)^2$.

The admissible values of x and y can then be obtained from,

$$0 \leq x = \frac{\epsilon + \eta^2 + \eta + \frac{1}{4}}{2} < 1, \qquad y = \frac{\epsilon + \eta^2 - \eta + \frac{1}{4}}{2} > 0. \tag{5.27}$$

Another set of values that make the method (5.1)–(5.2) time-stable is then given by

$$\tau_L \geq \frac{1}{2}, \qquad \beta_R < \frac{8q}{(1+2q)^2}, \qquad \tau_R = \beta_R \left(\frac{1}{2} + q\right),$$

$$c_0^L = c_1^L = ... = c_{m-2}^L = 1, \qquad c_{m-1}^L = 1 - x, \qquad c_m^L = 2y,$$

$$\Gamma = \text{diag}\left(0, \cdots, 0, \frac{1 - c_{m-1}^L}{2c_{m-1}^L}, 0\right),$$

for all $q > 0$ and x and y given by Eq. (5.27).

Interior overlap

In this section, we discuss the time-stability of the method (5.1)-(5.2) for a grid configuration, as shown in Figure 5.3, where the donor grid points lie in the interior of the domain. The numerical boundary condition in this case is given by,

$$\hat{v}_0 = T_L^T \mathbf{u} = \alpha_L u_{j+1} + (1 - \alpha_L) u_{j+2}, \tag{5.28}$$

$$T_L = [0 \cdots 0 \;\; \alpha_L \;\; (1 - \alpha_L) \;\; 0 \cdots 0]^T. \tag{5.29}$$

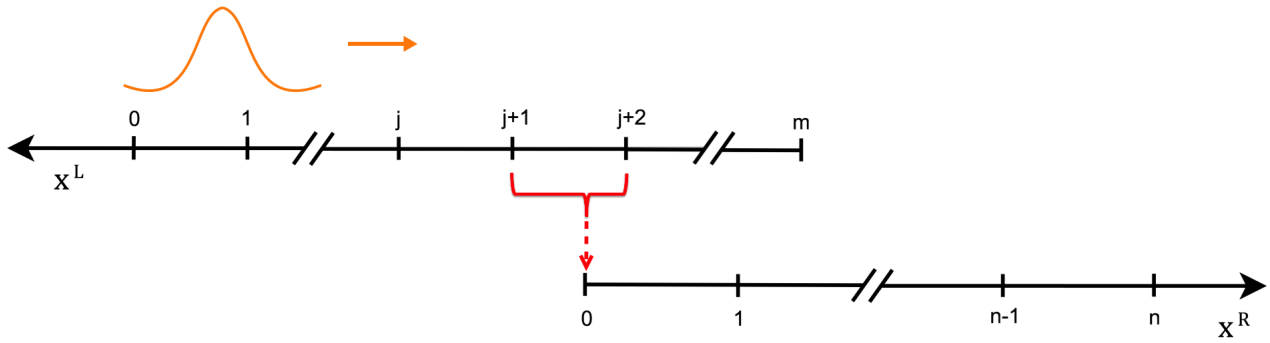

Figure 5.3: Schematic diagram of the overlapping grids where interpolation is needed from the interior points of the left domain.

Theorem 5.2 *The method (5.1)–(5.2) for the overlapping grid configuration shown in Figure 5.3 with the* $1-2-1$ *SBP first derivative approximation, linear Lagrange interpolation and a dissipative operator given by Eq. (5.8) is time-stable if*

$$\tau_L \geq \frac{1}{2}, \qquad 0 < \beta_R \leq \frac{8q}{(1+2q)^2}\left(\frac{2py}{p - 2p\alpha_L + (p+y)\alpha_L^2}\right), \qquad \tau_R = \beta_R\left(\frac{1}{2} + q\right),$$

$$c_0^L = \ldots\ldots = c_j^L = 1, \qquad c_{j+1}^L = 1 - p, \qquad c_{j+2}^L = y + z, \qquad c_{j+3}^L = \ldots\ldots = c_m^L = z, \tag{5.30}$$

$$\Gamma_L = \text{diag}\left(0, \ldots\ldots, 0, \frac{1 - c_{j+1}^L}{2c_{j+1}^L}, \frac{c_{j+2}^L - c_m^L}{2c_{j+2}^L}, 0, \ldots\ldots, 0\right)$$

with $z = 1 - 2p - 2y$ *and* $p + y < \frac{1}{2}$ *for* $p, y, z, q > 0$.

Proof. Consider $C_L = \text{diag}(1, \cdots, 1, c_{j+1}^L, c_{j+2}^L, z, \cdots, z)$ and $\Gamma_L = \text{diag}(0, ..., 0, \gamma_{j+1}, \gamma_{j+2}, 0, ..., 0)$. Substituting them to (5.7) using (5.9), (5.29) and the $1-2-1$ SBP first derivative approximation yields

$$\frac{\mathrm{d}}{\mathrm{d}t}||\mathbf{w}||_H^2 = -[1-(1+2\gamma_{j+1})c_{j+1}^L]u_j u_{j+1} - 4\gamma_{j+1}c_{j+1}^L u_{j+1}^2 - [(1-2\gamma_{j+1})c_{j+1}^L - c_{j+2}^L(1+2\gamma_{j+2})]u_{j+1}u_{j+2}$$

$$-4\gamma_{j+2}c_{j+2}^L u_{j+2}^2 + (c_m^L - c_{j+2}^L(1-2\gamma_{j+2}))u_{j+2}u_{j+3} - c_m^L u_m^2 + 2\tau_R\alpha_L v_0 u_{j+1} + 2\tau_R(1-\alpha_L)v_0 u_{j+2} + (\beta_R - 2\tau_R)v_0^2$$

$$+ (1-2\tau_L)u_0^2 - \beta_R v_n^2. \tag{5.31}$$

Using

$$\gamma_{j+1} = \tfrac{1-c_{j+1}^L}{2c_{j+1}^L}, \qquad \gamma_{j+2} = \tfrac{c_{j+2}^L - c_m^L}{2c_{j+2}^L}, \qquad \mathbf{s} = [u_{j+1} \;\; u_{j+2} \;\; v_0]^T, \qquad \tau_L \geq \tfrac{1}{2},$$

Eq. (5.31) becomes,

$$\frac{\mathrm{d}}{\mathrm{d}t}||\mathbf{w}||_H^2 \leq \mathbf{s}^T \begin{bmatrix} 2(-1+c_{j+1}^L) & -c_{j+1}^L + c_{j+2}^L - \frac{c_m^L}{2} + \frac{1}{2} & \tau_R\alpha_L \\ -c_{j+1}^L + c_{j+2}^L - \frac{c_m^L}{2} + \frac{1}{2} & 2c_m^L - 2c_{j+2}^L & \tau_R(1-\alpha_L) \\ \tau_R\alpha_L & \tau_R(1-\alpha_L) & \beta_R - 2\tau_R \end{bmatrix} \mathbf{s} = \mathbf{s}^T K \mathbf{s}, \tag{5.32}$$

For time-stability, the matrix K must be negative semidefinite, i.e. all principal minors, $\triangle_k$ of order $k = 1, 2, 3$ must obey $(-1)^k \triangle_k \geq 0$. From first-order principal minors we have,

$$1 - c_{j+1}^L \geq 0, \qquad c_{j+2}^L \geq c_m^L, \qquad \tau_R \geq \frac{\beta_R}{2}. \tag{5.33}$$

Therefore, let us assume that

$$c_{j+1}^L = 1 - p, \qquad c_{j+2}^L = c_m^L + y, \qquad c_m^L = z, \qquad \tau_R = \frac{\beta_R}{2} + \beta_R q, \tag{5.34}$$

where p, y and q are non-negative numbers, $z > 0$, and $p < 1$ to ensure $c_{j+1}^L > 0$. Inserting the change of variables (5.34) into (5.32) yields

$$K = \begin{bmatrix} -2p & p + y + \frac{z}{2} - \frac{1}{2} & \beta_R(\frac{1}{2}+q)\alpha_L \\ p + y + \frac{z}{2} - \frac{1}{2} & -2y & \beta_R(\frac{1}{2}+q)(1-\alpha_L) \\ \beta_R(\frac{1}{2}+q)\alpha_L & \beta_R(\frac{1}{2}+q)(1-\alpha_L) & -2\beta_R q \end{bmatrix}. \tag{5.35}$$

If we take $z = 1 - 2p - 2y$, the second-order principal minors give the following three conditions:

$$4py \geq 0, \tag{5.36}$$

$$4pq - \beta_R \left(\frac{1}{2} + q\right)^2 \alpha_L^2 \geq 0, \tag{5.37}$$

$$4yq - \beta_R \left(\frac{1}{2} + q\right)^2 (1-\alpha_L)^2 \geq 0, \tag{5.38}$$

and the third order principal minor yields

$$\beta_R \leq \frac{8q}{(1+2q)^2}\left(\frac{2py}{p - 2p\alpha_L + (p+y)\alpha_L^2}\right). \tag{5.39}$$

Values of $p, y > 0$ such that $p + y < \frac{1}{2}$ and $q > 0$ satisfies Eqs. (5.36)-(5.39) for all values of $\alpha_L \in [0, 1]$. This completes the proof. □

5.1.3 Stability of the Third-Order Scheme

In this section, we discuss the proof of time-stability for the globally third-order accurate version of the method (5.1)–(5.2). The operator $D = P^{-1}Q$, in this case, denotes the $2-4-2$ SBP first derivative approximation. Cubic interpolation is used to retain third order global accuracy.

Boundary Overlap

First we discuss the scenario where the left-most grid point of the right grid (x_0^R) lies between the points x_{m-2}^L and x_{m-1}^L of the left grid as shown in Figure 5.4. Therefore, the numerical boundary condition at x_0^R is given using the cubic Lagrange interpolation by,

$$\hat{v}_0 = T_L^T \mathbf{u} = \sum_{i=1}^{4} l_i(x_0^R) u_{m-4+i} = l_1(x_0^R)u_{m-3} + l_2(x_0^R)u_{m-2} + l_3(x_0^R)u_{m-1} + l_4(x_0^R)u_m, \tag{5.40}$$

$$T_L = [0 \,....\, 0 \; l_1 \; l_2 \; l_3 \; l_4]^T, \tag{5.41}$$

where T_L is a vector of size $(m+1)$. The interpolation coefficients $l_i(x_0^R)$ for the cubic Lagrange interpolation are obtained from

$$l_i(x_0^R) = \prod_{\substack{p=1 \\ p \neq i}}^{4} \frac{x_0^R - x_{m-4+p}^L}{x_{m-4+i}^L - x_{m-4+p}^L}, \qquad \text{for } i = 1, 2, 3, 4. \tag{5.42}$$

To simplify the notation in proofs we substitute in (5.42) $\delta x = x_0^R - x_{m-2}^L$ and $\alpha_L = 1 - \frac{\delta x}{h_L}$, where h_L is the grid spacing on the left domain, to get

$$l_1(x_0^R) = -\frac{1}{6}\alpha_L(1-\alpha_L)(1+\alpha_L), \qquad l_2(x_0^R) = \frac{1}{2}\alpha_L(2-\alpha_L)(1+\alpha_L),$$

$$l_3(x_0^R) = \frac{1}{2}(1-\alpha_L)(2-\alpha_L)(1+\alpha_L), \qquad l_4(x_0^R) = -\frac{1}{6}\alpha_L(1-\alpha_L)(2-\alpha_L). \tag{5.43}$$

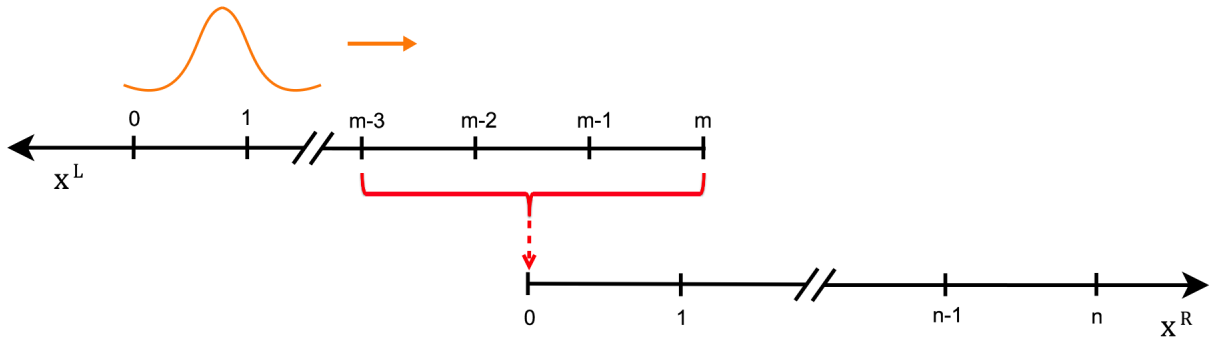

Figure 5.4: Schematic diagram of overlapping grids for boundary overlap case of cubic interpolation.

We use a dissipative operator Υ_L given by Eq. (5.8) where

$$\Upsilon_L = \frac{1}{h_L}\begin{bmatrix} 0 & 0 & 0 & 0 & 0 & 0 & & & & \\ \ddots & \ddots & \ddots & \ddots & \ddots & \ddots & \ddots & & & \\ & \ddots & \ddots & \ddots & \ddots & \ddots & \ddots & \ddots & & \\ & & & 0 & 0 & 0 & 0 & 0 & 0 & \\ & & & & r_{11} & r_{12} & r_{13} & r_{14} & r_{15} & r_{16} \\ & & & & & r_{21} & r_{22} & r_{23} & r_{24} & r_{25} \\ & & & & & & r_{31} & r_{32} & r_{33} & r_{34} \\ & & & & & & r_{41} & r_{42} & r_{43} & r_{44} \end{bmatrix}. \tag{5.44}$$

For consistency of the discrete approximation (4.6), $\tilde{D}_L = P_L^{-1}Q_L - \Upsilon_L$ must be an approximation of the first spatial derivative and for a global accuracy of third-order the derivative stencils of $\tilde{D}_L$ at the donor grid points must be at least second-order accurate (see Gustafsson, 1975).

Our aim is to satisfy $\frac{\mathrm{d}}{\mathrm{d}t}||\mathbf{w}||_H^2 \leq 0$ (see Eq. 5.7) by determining the suitable values of the parameters τ_L, τ_R, C_L, Υ_L and β_R for $\alpha_L \in [0,1]$.

Theorem 5.3 *The method (5.1)–(5.2) for the overlapping grid configuration shown in Figure 5.4 with the* $2-4-2$ *SBP first derivative approximation, cubic Lagrangian interpolation and a dissipative operator given by Eq. (5.44) is time-stable if*

$$\beta_R > 0, \qquad \tau_R \geq \frac{4\beta_R}{3}, \tag{5.45}$$

$$\tau_L \geq \frac{\lambda}{2}, \qquad c_0^L = \ldots\ldots = c_{m-4}^L = \lambda, \qquad c_{m-3}^L = \frac{1}{147}(112\lambda + 43c_{m-2}^L - 59c_{m-1}^L + 51c_m^L),$$

$$r_{16} = -\frac{43}{1176} + \frac{215c_{m-2}^L - 1121c_{m-1}^L + 1207c_m^L}{56(43c_{m-2}^L - 59c_{m-1}^L + 51c_m^L + 112\lambda)}, \qquad r_{25} = \frac{8\lambda - 91c_{m-2}^L + 236c_{m-1}^L - 153c_m^L}{516c_{m-2}^L},$$

$$r_{34} = \frac{43c^L_{m-2} + 118c^L_{m-1} - 153c^L_m - 8\lambda}{708c^L_{m-1}}, \qquad r_{44} = \frac{43c^L_{m-2} - 236c^L_{m-1} + 201c^L_m - 8\lambda}{612c^L_m}, \tag{5.46}$$

$$r_{11} = \frac{4(c^L_{m-3} - \lambda)}{49c^L_{m-3}}, \quad r_{12} = -\frac{32(c^L_{m-3} - \lambda)}{49c^L_{m-3}}, \quad r_{13} = -6r_{11} - 3r_{12} - r_{16}, \quad r_{14} = 8r_{11} + 3r_{12} + 3r_{16},$$

$$r_{15} = -3r_{11} - r_{12} - 3r_{16}, \quad r_{21} = \frac{4(c^L_{m-2} - \lambda)}{43c^L_{m-2}}, \quad r_{22} = -3r_{21} - r_{25}, \quad r_{23} = 3(r_{21} + r_{25}),$$

$$r_{24} = -r_{21} - 3r_{25}, \quad r_{31} = -r_{34}, \quad r_{32} = 3r_{34}, \quad r_{33} = -3r_{34}, \quad r_{41} = -r_{44}, \quad r_{42} = 3r_{44}, \quad r_{43} = -3r_{44},$$

where

$$c^L_{m-2} = \frac{16(135 + 2\sqrt{3})}{1161}, \qquad c^L_{m-1} = \frac{16(27 + 4\sqrt{3})}{1593}, \qquad c^L_m = \frac{16}{153\sqrt{3}}, \qquad \lambda = 2 + \frac{2}{9\sqrt{3}}. \tag{5.47}$$

Proof. Using (5.54) and (5.58) in (5.5) and (5.6) with

$$C_L = \mathrm{diag}(\lambda, \ldots, \lambda, c^L_{m-3}, c^L_{m-2}, c^L_{m-1}, c^L_m), \quad \tau_L \geq \frac{\lambda}{2}, \tag{5.48}$$

$$r_{11} = \frac{4(c^L_{m-3} - \lambda)}{49c^L_{m-3}}, \quad r_{12} = -\frac{32(c^L_{m-3} - \lambda)}{49c^L_{m-3}}, \quad r_{21} = \frac{4(c^L_{m-2} - \lambda)}{43c^L_{m-2}}, \tag{5.49}$$

we get

$$\frac{\mathrm{d}}{\mathrm{d}t}||\mathbf{w}||^2_H \leq \mathbf{s}^T K \mathbf{s},$$

where

$$\mathbf{s} = \begin{bmatrix} u_{m-3} & u_{m-2} & u_{m-1} & u_m & v_0 \end{bmatrix}^T,$$

$$K = \begin{bmatrix} \frac{49}{24}c^L_{m-3}r_{13} & \frac{1}{96}(c^L_{m-3}(-59 + 98r_{14}) + c^L_{m-2}(59 + 86r_{22})) \\ \frac{1}{96}(c^L_{m-3}(-59 + 98r_{14}) + c^L_{m-2}(59 + 86r_{22})) & \frac{43}{24}c^L_{m-2}r_{23} \\ \frac{1}{48}(49c^L_{m-3}r_{15} + 59c^L_{m-1}r_{31}) & \frac{1}{96}(c^L_{m-2}(-59 + 86r_{24}) + 59(c^L_{m-1} + 2c^L_{m-1}r_{32})) \\ \frac{1}{96}(c^L_{m-3}(3 + 98r_{16}) + c^L_m(-3 + 34r_{41})) & \frac{1}{48}(c^L_{m-2}(4 + 43r_{25}) + c^L_m(-4 + 17r_{42})) \\ \tau_R l_1 & \tau_R l_2 \end{bmatrix}$$

$$\begin{bmatrix} \frac{1}{48}(49c^L_{m-3}r_{15} + 59c^L_{m-1}r_{31}) & \frac{1}{96}(c^L_{m-3}(3 + 98r_{16}) + c^L_m(-3 + 34r_{41})) & \tau_R l_1 \\ \frac{1}{96}(c^L_{m-2}(-59 + 86r_{24}) + 59(c^L_{m-1} + 2c^L_{m-1}r_{32})) & \frac{1}{48}(c^L_{m-2}(4 + 43r_{25}) + c^L_m(-4 + 17r_{42})) & \tau_R l_2 \\ \frac{59}{24}c^L_{m-1}r_{33} & \frac{1}{96}(59(c^L_m + c^L_{m-1}(-1 + 2r_{34})) + 34c^L_m r_{43})) & \tau_R l_3 \\ \frac{1}{96}(59(c^L_m + c^L_{m-1}(-1 + 2r_{34})) + 34c^L_m r_{43})) & c^L_m(-1 + \frac{17}{24}r_{44}) & \tau_R l_4 \\ \tau_R l_3 & \tau_R l_4 & \beta_R - 2\tau_R \end{bmatrix}.$$

A second-order accuracy of the first derivative approximation $\tilde{D}_L\mathbf{u} = (P_L^{-1}Q_L - \Upsilon_L)\mathbf{u}$ at the donor points requires

$$r_{13} = -6r_{11} - 3r_{12} - r_{16}, \qquad r_{14} = 8r_{11} + 3r_{12} + 3r_{16}, \qquad r_{15} = -3r_{11} - r_{12} - 3r_{16},$$

$$r_{22} = -3r_{21} - r_{25}, \qquad r_{23} = 3(r_{21} + r_{25}), \qquad r_{24} = -r_{21} - 3r_{25}, \tag{5.50}$$

$$r_{31} = -r_{34}, \qquad r_{32} = 3r_{34}, \qquad r_{33} = -3r_{34},$$

$$r_{41} = -r_{44}, \qquad r_{42} = 3r_{44}, \qquad r_{43} = -3r_{44}.$$

Substituting the above accuracy conditions in K with (5.49) yields

$$K = \begin{bmatrix} -3\lambda + c_{m-3}^L(3 - \frac{49}{24}r_{16}) & \frac{1}{96}(152\lambda + c_{m-3}^L(-187 + 294r_{16}) + c_{m-2}^L(35 - 86r_{25})) \\ \frac{1}{96}(152\lambda + c_{m-3}^L(-187 + 294r_{16}) + c_{m-2}^L(35 - 86r_{25})) & \frac{1}{8}(-4\lambda + c_{m-2}^L(4 + 43r_{25})) \\ \frac{1}{48}(-20\lambda + c_{m-3}^L(20 - 147r_{16}) - 59c_{m-1}^L r_{34}) & \frac{1}{96}(8\lambda - c_{m-2}^L(67 + 258r_{25}) + 59c_{m-1}^L(1 + 6r_{34})) \\ \frac{1}{96}(c_{m-3}^L(3 + 98r_{16}) - c_m^L(3 + 34r_{44})) & \frac{1}{48}(c_{m-2}^L(4 + 43r_{25}) + c_m^L(-4 + 51r_{44})) \\ \tau_R l_1 & \tau_R l_2 \end{bmatrix}$$

$$\begin{bmatrix} \frac{1}{48}(-20\lambda + c_{m-3}^L(20 - 147r_{16}) - 59c_{m-1}^L r_{34}) & \frac{1}{96}(c_{m-3}^L(3 + 98r_{16}) - c_m^L(3 + 34r_{44})) & \tau_R l_1 \\ \frac{1}{96}(8\lambda - c_{m-2}^L(67 + 258r_{25}) + 59c_{m-1}^L(1 + 6r_{34})) & \frac{1}{48}(c_{m-2}^L(4 + 43r_{25}) + c_m^L(-4 + 51r_{44})) & \tau_R l_2 \\ -\frac{59}{8}c_{m-1}^L r_{34} & \frac{1}{96}(59(c_m^L + c_{m-1}^L(-1 + 2r_{34})) - 102c_m^L r_{44}) & \tau_R l_3 \\ \frac{1}{96}(59(c_m^L + c_{m-1}^L(-1 + 2r_{34})) - 102c_m^L r_{44}) & c_m^L(-1 + \frac{17}{24}r_{44}) & \tau_R l_4 \\ \tau_R l_3 & \tau_R l_4 & \beta_R - 2\tau_R \end{bmatrix}.$$

To prove time-stability, we need to show that the above symmetric matrix K is negative semidefinite. Substituting

$$r_{16} = -\frac{43}{1176} + \frac{215c_{m-2}^L - 1121c_{m-1}^L + 1207c_m^L}{56(43c_{m-2}^L - 59c_{m-1}^L + 51c_m^L + 112\lambda)}, \quad r_{25} = \frac{8\lambda - 91c_{m-2}^L + 236c_{m-1}^L - 153c_m^L}{516c_{m-2}^L},$$

$$r_{34} = \frac{43c_{m-2}^L + 118c_{m-1}^L - 153c_m^L - 8\lambda}{708c_{m-1}^L}, \quad r_{44} = \frac{43c_{m-2}^L - 236c_{m-1}^L + 201c_m^L - 8\lambda}{612c_m^L},$$

$$c_{m-3}^L = \frac{1}{147}(112\lambda + 43c_{m-2}^L - 59c_{m-1}^L + 51c_m^L),$$

in K simplifies the matrix to

$$K = \begin{bmatrix} k_{11} & 0 & 0 & 0 & \tau_R l_1 \\ 0 & k_{22} & 0 & 0 & \tau_R l_2 \\ 0 & 0 & k_{33} & 0 & \tau_R l_3 \\ 0 & 0 & 0 & k_{44} & \tau_R l_4 \\ \tau_R l_1 & \tau_R l_2 & \tau_R l_3 & \tau_R l_4 & \beta_R - 2\tau_R \end{bmatrix}, \tag{5.51}$$

where

$$k_{11} = \frac{(-568\lambda + 731c^L_{m-2} - 826c^L_{m-1} + 663c^L_m)}{864}, \qquad k_{22} = \frac{(-40\lambda - 43c^L_{m-2} + 236c^L_{m-1} - 153c^L_m)}{96},$$

$$k_{33} = \frac{(8\lambda - 43c^L_{m-2} - 118c^L_{m-1} + 153c^L_m)}{96}, \qquad k_{44} = \frac{(-8\lambda + 43c^L_{m-2} - 236c^L_{m-1} - 663c^L_m)}{864}.$$

For cubic Lagrangian interpolation, given by Eq. (5.43), where $\alpha_L \in [0, 1]$ we have

$$l_1,\, l_4 \,\in\, [-\frac{1}{9\sqrt{3}}, 0], \qquad l_2,\, l_3 \,\in\, [0, 1], \qquad (\sum_{i=1}^{4} |l_i|)_{max} = \frac{5}{4} \tag{5.52}$$

From the Gershgorin circle theorem, all eigenvalues of the matrix K are non-positive for $\alpha_L \in [0, 1]$ if

$$\beta_R > 0, \quad \tau_R \geq \frac{4\beta_R}{3}, \quad -k_{11},\, -k_{44} \geq \frac{\tau_R}{9\sqrt{3}}, \qquad -k_{22},\, -k_{33} \geq \tau_R, \tag{5.53}$$

for k_{11}, k_{22}, k_{33}, $k_{44} \leq 0$. Solving k_{11}, k_{22}, k_{33} and k_{44} in (5.53) with equality gives

$$c^L_{m-2} = \frac{16(135 + 2\sqrt{3})}{1161}, \qquad c^L_{m-1} = \frac{16(27 + 4\sqrt{3})}{1593}, \qquad c^L_m = \frac{16}{153\sqrt{3}}, \qquad \lambda = 2 + \frac{2}{9\sqrt{3}},$$

which completes the proof. □

Interior Overlap

Here we discuss the case where the left-most grid point of the right grid (x^R_0) lies between the points x^L_{j+2} and x^L_{j+3} of the left grid as shown in Figure 5.5, where all the donor grid points $x^L_{j+1}, \cdots, x^L_{j+4}$ lie in the interior of the left subdomain. Therefore, the numerical boundary condition at x^R_0 is given using the cubic Lagrange interpolation by

$$\hat{v}_0 = T^T_L \mathbf{u} = \sum_{i=1}^{4} l_i(x^R_0) u_{j+i} = l_1(x^R_0)u_{j+1} + l_2(x^R_0)u_{j+2} + l_3(x^R_0)u_{j+3} + l_4(x^R_0)u_{j+4}, \tag{5.54}$$

$$T_L = [0 \,....\, 0 \;\; l_1 \;\; l_2 \;\; l_3 \;\; l_4 \;\; 0 \,....\, 0]^T, \tag{5.55}$$

where T_L is a vector of size $(m+1)$. The interpolation coefficients $l_i(x^R_0)$ for the cubic Lagrange interpolation are obtained from

$$l_i(x^R_0) = \prod_{\substack{p=1 \\ p \neq i}}^{4} \frac{x^R_0 - x^L_{j+p}}{x^L_{j+i} - x^L_{j+p}}, \qquad \text{for } \; i = 1, 2, 3, 4. \tag{5.56}$$

To simplify the notation in proofs we substitute in (5.56) $\delta x = x_0^R - x_{j+2}^L$ and $\alpha_L = 1 - \frac{\delta x}{h_L}$, where h_L is the grid spacing on the left domain, to get

$$l_1(x_0^R) = -\frac{1}{6}\alpha_L(1-\alpha_L)(1+\alpha_L), \qquad l_2(x_0^R) = \frac{1}{2}\alpha_L(2-\alpha_L)(1+\alpha_L),$$

$$l_3(x_0^R) = \frac{1}{2}(1-\alpha_L)(2-\alpha_L)(1+\alpha_L), \qquad l_4(x_0^R) = -\frac{1}{6}\alpha_L(1-\alpha_L)(2-\alpha_L). \tag{5.57}$$

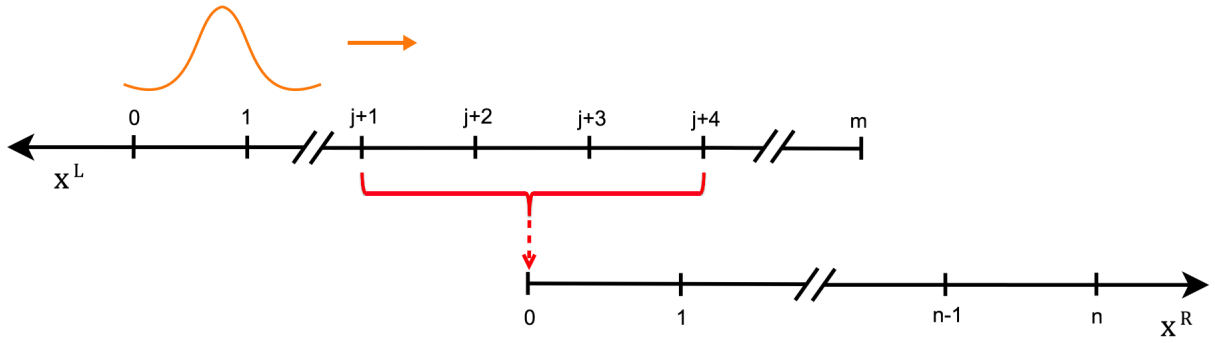

Figure 5.5: Schematic diagram of overlapping grids for cubic interpolation.

We use a dissipative operator Υ_L given by Eq. (5.8) where

$$\Upsilon_L = \frac{1}{h_L}\begin{bmatrix}
\ddots & \ddots & \ddots & \ddots & \ddots & & & & & & \\
 & 0 & 0 & 0 & 0 & 0 & & & & & \\
 & & r_{11} & r_{12} & r_{13} & r_{14} & r_{15} & & & & \\
 & & & r_{21} & r_{22} & r_{23} & r_{24} & r_{25} & & & \\
 & & & & r_{31} & r_{32} & r_{33} & r_{34} & r_{35} & & \\
 & & & & & r_{41} & r_{42} & r_{43} & r_{44} & r_{45} & \\
 & & & & & & 0 & 0 & 0 & 0 & 0 \\
 & & & & & & & \ddots & \ddots & \ddots & \ddots & \ddots
\end{bmatrix}. \tag{5.58}$$

The non-zero rows correspond to the donor grid points x_{j+1}, $\cdots$, x_{j+4}. For consistency of the discrete approximation (4.6), $\tilde{D}_L = P_L^{-1}Q_L - \Upsilon_L$ must be an approximation of the first spatial derivative and for a global accuracy of third-order the derivative stencils of $\tilde{D}_L$ at the donor grid points must be at least second-order accurate (see Gustafsson, 1975).

Our aim is to satisfy $\frac{\mathrm{d}}{\mathrm{d}t}||\mathbf{w}||_H^2 \leq 0$ (see Eq. 5.7) by determining the suitable values of the parameters τ_L, τ_R, C_L, Υ_L and β_R for $\alpha_L \in [0,1]$.

Theorem 5.4 *The method (5.1)–(5.2) for the overlapping grid configuration shown in Figure 5.5 with the* $2-4-2$ *SBP first derivative approximation, cubic Lagrangian interpolation and a dissipative operator given by Eq. (5.58) is time-stable if*

$$\tau_L \geq \frac{\lambda}{2}, \qquad \beta_R > 0, \qquad \tau_R \geq \frac{4\beta_R}{3},$$

$$c_0^L = ... = c_j^L = \lambda, \qquad c_{j+1}^L = \frac{1}{18}(17\lambda + \mu), \quad c_{j+2}^L = \frac{1}{3}(2\lambda + \mu),$$

$$c_{j+3}^L = \frac{1}{3}(\lambda + 2\mu), \quad c_{j+4}^L = \frac{1}{18}(\lambda + 17\mu), \qquad c_{j+5}^L = ... = c_m^L = \mu,$$

$$r_{11} = \frac{c_{j+1}^L - \lambda}{12c_{j+1}^L}, \quad r_{12} = -\frac{2(c_{j+1}^L - \lambda)}{3c_{j+1}^L}, \quad r_{13} = -6r_{11} - 3r_{12}, \quad r_{14} = 8r_{11} + 3r_{12}, \quad r_{15} = -3r_{11} - r_{12},$$

$$r_{21} = \frac{c_{j+2}^L - \lambda}{12c_{j+2}^L}, \qquad r_{22} = -4r_{21}, \qquad r_{23} = 6r_{21}, \qquad r_{24} = -4r_{21}, \qquad r_{25} = r_{21}, \tag{5.59}$$

$$r_{31} = r_{35}, \qquad r_{32} = -4r_{35}, \qquad r_{33} = 6r_{35}, \qquad r_{34} = -4r_{35}, \qquad r_{35} = \frac{-c_{j+3}^L + \mu}{12c_{j+3}^L},$$

$$r_{41} = -r_{44} - 3r_{45}, \quad r_{42} = 3r_{44} + 8r_{45}, \quad r_{43} = -3r_{44} - 6r_{45}, \quad r_{44} = \frac{2(c_{j+4}^L - \mu)}{3c_{j+4}^L}, \quad r_{45} = \frac{-c_{j+4}^L + \mu}{12c_{j+4}^L},$$

with choices of λ *and* μ *such that* $\lambda - \mu \geq 3\tau_R$ *for* $\lambda, \mu > 0$.

Proof. Using (5.54) and (5.58) in (5.5) and (5.6) with

$$C_L = \text{diag}(\lambda, \ldots, \lambda, c_{j+1}^L, c_{j+2}^L, c_{j+3}^L, c_{j+4}^L, \mu, \ldots, \mu), \quad \tau_L \geq \frac{\lambda}{2}, \tag{5.60}$$

$$r_{11} = \frac{c_{j+1}^L - \lambda}{12c_{j+1}^L}, \quad r_{12} = -\frac{2(c_{j+1}^L - \lambda)}{3c_{j+1}^L}, \quad r_{21} = \frac{c_{j+2}^L - \lambda}{12c_{j+2}^L}, \tag{5.61}$$

$$r_{35} = \frac{-c_{j+3}^L + \mu}{12c_{j+3}^L}, \quad r_{44} = \frac{2(c_{j+4}^L - \mu)}{3c_{j+4}^L}, \quad r_{45} = \frac{-c_{j+4}^L + \mu}{12c_{j+4}^L}, \tag{5.62}$$

we get

$$\frac{\mathrm{d}}{\mathrm{d}t}||\mathbf{w}||_H^2 \leq \mathbf{s}^T K \mathbf{s},$$

where

$$\mathbf{s} = [u_{j+1} \;\; u_{j+2} \;\; u_{j+3} \;\; u_{j+4} \;\; v_0]^T,$$

$$K = \begin{bmatrix} 2c_{j+1}^L r_{13} & c_{j+1}^L(-\frac{2}{3}+r_{14})+c_{j+2}^L(\frac{2}{3}+r_{22}) & c_{j+1}^L(\frac{1}{12}+r_{15})+c_{j+3}^L(-\frac{1}{12}+r_{31}) \\ c_{j+1}^L(-\frac{2}{3}+r_{14})+c_{j+2}^L(\frac{2}{3}+r_{22}) & 2c_{j+2}^L r_{23} & c_{j+2}^L(-\frac{2}{3}+r_{24})+c_{j+3}^L(\frac{2}{3}+r_{32}) \\ c_{j+1}^L(\frac{1}{12}+r_{15})+c_{j+3}^L(-\frac{1}{12}+r_{31}) & c_{j+2}^L(-\frac{2}{3}+r_{24})+c_{j+3}^L(\frac{2}{3}+r_{32}) & 2c_{j+3}^L r_{33} \\ 0 & c_{j+2}^L(\frac{1}{12}+r_{25})+c_{j+4}^L(-\frac{1}{12}+r_{41}) & c_{j+3}^L(-\frac{2}{3}+r_{34})+c_{j+4}^L(\frac{2}{3}+r_{42}) \\ \tau_R l_1 & \tau_R l_2 & \tau_R l_3 \end{bmatrix}$$

$$\begin{bmatrix} 0 & \tau_R l_1 \\ c_{j+2}^L(\frac{1}{12}+r_{25})+c_{j+4}^L(-\frac{1}{12}+r_{41}) & \tau_R l_2 \\ c_{j+3}^L(-\frac{2}{3}+r_{34})+c_{j+4}^L(\frac{2}{3}+r_{42}) & \tau_R l_3 \\ 2c_{j+4}^L r_{43} & \tau_R l_4 \\ \tau_R l_4 & \beta_R - 2\tau_R \end{bmatrix}.$$

We apply an accuracy of $2-3-3-2$ for the first derivative approximation $\tilde{D}_L\mathbf{u} = (P_L^{-1}Q_L - \Upsilon_L)\mathbf{u}$ at the donor grid points i.e. we constrain the elements of the operator Υ_L such that the derivative approximation $(\tilde{D}_L\mathbf{u})_{j+1}$ is second-order accurate, $(\tilde{D}_L\mathbf{u})_{j+2}$ and $(\tilde{D}_L\mathbf{u})_{j+3}$ are third-order accurate and $(\tilde{D}_L\mathbf{u})_{j+4}$ is second-order accurate. We chose $2-3-3-2$ since it was the highest order of approximation for which a solution could be found. The accuracy conditions,

$$\begin{gathered} r_{13} = -6r_{11} - 3r_{12}, \qquad r_{14} = 8r_{11} + 3r_{12}, \qquad r_{15} = -3r_{11} - r_{12}, \\ r_{22} = -4r_{21}, \qquad r_{23} = 6r_{21}, \qquad r_{24} = -4r_{21}, \qquad r_{25} = r_{21}, \\ r_{31} = r_{35}, \qquad r_{32} = -4r_{35}, \qquad r_{33} = 6r_{35}, \qquad r_{34} = -4r_{35}, \\ r_{41} = -r_{44} - 3r_{45}, \qquad r_{42} = 3r_{44} + 8r_{45}, \qquad r_{43} = -3r_{44} - 6r_{45}, \end{gathered} \tag{5.63}$$

substituted in K with (5.61) and (5.62) yields

$$K = \begin{bmatrix} 3(c_{j+1}^L - \lambda) & \frac{1}{3}(-6c_{j+1}^L + c_{j+2}^L + 5\lambda) & \frac{1}{12}(6c_{j+1}^L - 2c_{j+3}^L - 5\lambda + \mu) \\ \frac{1}{3}(-6c_{j+1}^L + c_{j+2}^L + 5\lambda) & c_{j+2}^L - \lambda & \frac{1}{3}(-3c_{j+2}^L + 3c_{j+3}^L + \lambda - \mu) \\ \frac{1}{12}(6c_{j+1}^L - 2c_{j+3}^L - 5\lambda + \mu) & \frac{1}{3}(-3c_{j+2}^L + 3c_{j+3}^L + \lambda - \mu) & -c_{j+3}^L + \mu \\ 0 & \frac{1}{12}(2c_{j+2}^L - 6c_{j+4}^L - \lambda + 5\mu) & \frac{1}{3}(-c_{j+3}^L + 6c_{j+4}^L - 5\mu) \\ \tau_R l_1 & \tau_R l_2 & \tau_R l_3 \end{bmatrix}$$

$$\begin{bmatrix} 0 & \tau_R l_1 \\ \frac{1}{12}(2c_{j+2}^L - 6c_{j+4}^L - \lambda + 5\mu) & \tau_R l_2 \\ \frac{1}{3}(-c_{j+3}^L + 6c_{j+4}^L - 5\mu) & \tau_R l_3 \\ -3c_{j+4}^L + 3\mu & \tau_R l_4 \\ \tau_R l_4 & \beta_R - 2\tau_R \end{bmatrix}.$$

To prove time-stability, we need to show that the above symmetric matrix K is negative semidefinite. Substituting,

$$c_{j+1}^L = \frac{1}{18}(17\lambda + \mu), \quad c_{j+2}^L = \frac{1}{3}(2\lambda + \mu), \quad c_{j+3}^L = \frac{1}{3}(\lambda + 2\mu), \quad c_{j+4}^L = \frac{1}{18}(\lambda + 17\mu),$$

in K simplifies the matrix to,

$$K = \begin{bmatrix} \frac{1}{6}(\mu - \lambda) & 0 & 0 & 0 & \tau_R l_1 \\ 0 & \frac{1}{3}(\mu - \lambda) & 0 & 0 & \tau_R l_2 \\ 0 & 0 & \frac{1}{3}(\mu - \lambda) & 0 & \tau_R l_3 \\ 0 & 0 & 0 & \frac{1}{6}(\mu - \lambda) & \tau_R l_4 \\ \tau_R l_1 & \tau_R l_2 & \tau_R l_3 & \tau_R l_4 & \beta_R - 2\tau_R \end{bmatrix}. \tag{5.64}$$

Using (5.52) and the Gershgorin circle theorem, all eigenvalues of the matrix K are non-positive for $\alpha_L \in [0, 1]$ if

$$\lambda - \mu \geq 3\tau_R, \quad \tau_R \geq \frac{4\beta_R}{3},$$

which completes the proof. □

5.1.4 Stability of the Fourth-Order Scheme

In this section, we discuss the proof of time-stability for the globally fourth-order accurate version of the method (4.19)-(4.20). The operator $D = P^{-1}Q$, in this case, denotes the $3 - 6 - 3$ SBP first derivative approximation. Cubic interpolation is used to retain the global fourth order of accuracy.

Interior Overlap

We use a dissipative operator Υ_L given by Eq. (5.8) where

$$\Upsilon_L = \frac{1}{h_L} \begin{bmatrix} \ddots & \ddots & \ddots & \ddots & \ddots & & & & & & & & \\ & 0 & 0 & 0 & 0 & 0 & 0 & 0 & & & & & \\ & & r_{11} & r_{12} & r_{13} & r_{14} & r_{15} & r_{16} & r_{17} & & & & \\ & & & r_{21} & r_{22} & r_{23} & r_{24} & r_{25} & r_{26} & r_{27} & & & \\ & & & & r_{31} & r_{32} & r_{33} & r_{34} & r_{35} & r_{36} & r_{37} & & \\ & & & & & r_{41} & r_{42} & r_{43} & r_{44} & r_{45} & r_{46} & r_{47} & \\ & & & & & & 0 & 0 & 0 & 0 & 0 & 0 & 0 \\ & & & & & & & \ddots & \ddots & \ddots & \ddots & \ddots & \ddots & \ddots \end{bmatrix}. \tag{5.65}$$

The non-zero rows correspond to the donor grid points. For consistency of the discrete approximation (4.19), $\tilde{D}_L = -P_L^{-1}Q_L + \Upsilon_L$ must be an approximation of the first spatial derivative and for a global accuracy of fourth-order the derivative stencils of $\tilde{D}_L$ at the donor grid points must be at least third-order accurate.

Theorem 5.5 *The method (5.1)–(5.2) for the overlapping grid configuration shown in Figure 5.5 with the* $3-6-3$ *SBP first derivative approximation, cubic Lagrange interpolation and a dissipative operator given by Eq. (5.65) is time-stable if* $\tau_L \geq \frac{\lambda}{2}$,

$$c_0^L = ... = c_j^L = \lambda, \qquad c_{j+2}^L = \frac{1}{20}(180c_{j+1}^L - 161\lambda + \mu), \quad c_{j+3}^L = \frac{1}{2}(18c_{j+1}^L - 17\lambda + \mu),$$

$$c_{j+4}^L = \frac{1}{20}(20c_{j+1}^L - 19\lambda + 19\mu),, \qquad c_{j+5}^L = ... = c_m^L = \mu,$$

$$r_{11} = \frac{c_{j+1}^L - \lambda}{12c_{j+1}^L}, \quad r_{12} = -\frac{2(c_{j+1}^L - \lambda)}{3c_{j+1}^L}, \quad r_{13} = -\frac{3(c_{j+1}^L - \lambda)}{4c_{j+1}^L}, \quad r_{14} = -2(10r_{11} + 5r_{12} + 2r_{13}), \tag{5.66}$$

$$r_{15} = 45r_{11} + 20r_{12} + 6r_{13}, \qquad r_{16} = -36r_{11} - 15r_{12} - 4r_{13}, \qquad r_{17} = 10r_{11} + 4r_{12} + r_{13},$$

$$r_{21} = \frac{-c_{j+2}^L + \lambda}{60c_{j+2}^L}, \qquad r_{22} = \frac{3(c_{j+2}^L - \lambda)}{20c_{j+2}^L}, \qquad r_{23} = -10r_{21} - 4r_{22} + r_{27}, \qquad r_{24} = 20r_{21} + 6r_{22} - 4r_{27},$$

$$r_{25} = -15r_{21} - 4r_{22} + 6r_{27}, \qquad r_{26} = 4r_{21} + r_{22} - 4r_{27}, \qquad r_{27} = \frac{c_{j+2}^L - \mu}{60c_{j+2}^L},$$

$$r_{31} = \frac{-c_{j+3}^L + \lambda}{60c_{j+3}^L}, \qquad r_{32} = -4r_{31} + r_{36} + 4r_{37}, \qquad r_{33} = 6r_{31} - 4r_{36} - 15r_{37},$$

$$r_{34} = -4r_{31} + 6r_{36} + 20r_{37}, \qquad r_{35} = r_{31} - 4r_{36} - 10r_{37}, \qquad r_{36} = -\frac{3(c_{j+3}^L - \mu)}{20c_{j+3}^L}, \qquad r_{37} = \frac{c_{j+3}^L - \mu}{60c_{j+3}^L},$$

$$r_{41} = r_{45} + 4r_{46} + 10r_{47}, \qquad r_{42} = -4r_{45} - 15r_{46} - 36r_{47}, \qquad r_{43} = 6r_{45} + 20r_{46} + 45r_{47},$$

$$r_{44} = -4r_{45} - 10r_{46} - 20r_{47}, \qquad r_{45} = \frac{3(c_{j+4}^L - \mu)}{4c_{j+4}^L}, \qquad r_{46} = -\frac{3(c_{j+4}^L - \mu)}{20c_{j+4}^L}, \qquad r_{47} = \frac{c_{j+4}^L - \mu}{60c_{j+4}^L},$$

with choices of c_{j+1}^L, λ *and* μ *such that the matrix* K *given by Eq. (5.70) is negative semidefinite.*

Proof. Using (5.54) and (5.65) in (5.5) and (5.6) with,

$$C_L = \text{diag}(\lambda, \ldots, \lambda, c_{j+1}^L, c_{j+2}^L, c_{j+3}^L, c_{j+4}^L, \mu, \ldots, \mu), \quad \tau_L \geq \frac{\lambda}{2},$$

$$r_{11} = \frac{-c_{j+1}^L + \lambda}{60c_{j+1}^L}, \qquad r_{12} = \frac{3(c_{j+1}^L - \lambda)}{20c_{j+1}^L}, \qquad r_{13} = -\frac{3(c_{j+1}^L - \lambda)}{4c_{j+1}^L}, \qquad r_{21} = \frac{-c_{j+2}^L + \lambda}{60c_{j+2}^L}, \tag{5.67}$$

$$r_{22} = \frac{3(c_{j+2}^L - \lambda)}{20c_{j+2}^L}, \qquad r_{31} = \frac{-c_{j+3}^L + \lambda}{60c_{j+3}^L}, \qquad r_{27} = \frac{c_{j+2}^L - \mu}{60c_{j+2}^L}, \qquad r_{36} = -\frac{3(c_{j+3}^L - \mu)}{20c_{j+3}^L}, \tag{5.68}$$

$$r_{37} = \frac{c^L_{j+3} - \mu}{60c^L_{j+3}}, \qquad r_{45} = \frac{3(c^L_{j+4} - \mu)}{4c^L_{j+4}}, \qquad r_{46} = -\frac{3(c^L_{j+4} - \mu)}{20c^L_{j+4}}, \qquad r_{47} = \frac{c^L_{j+4} - \mu}{60c^L_{j+4}}, \tag{5.69}$$

we get,

$$\frac{d}{dt}||\mathbf{w}||^2_H \leq \mathbf{s}^T K \mathbf{s},$$

where,

$$\mathbf{s} = [u_{j+1} \quad u_{j+2} \quad u_{j+3} \quad u_{j+4} \quad v_0]^T,$$

$$K = \begin{bmatrix} 2c^L_{j+1}r_{14} & c^L_{j+1}(-\frac{3}{4} + r_{15}) + c^L_{j+2}(\frac{3}{4} + r_{23}) & c^L_{j+1}(\frac{3}{20} + r_{16}) + c^L_{j+3}(-\frac{3}{20} + r_{32}) \\ c^L_{j+1}(-\frac{3}{4} + r_{15}) + c^L_{j+2}(\frac{3}{4} + r_{23}) & 2c^L_{j+2}r_{24} & c^L_{j+2}(-\frac{3}{4} + r_{25}) + c^L_{j+3}(\frac{3}{4} + r_{33}) \\ c^L_{j+1}(\frac{3}{20} + r_{16}) + c^L_{j+3}(-\frac{3}{20} + r_{32}) & c^L_{j+2}(-\frac{3}{4} + r_{25}) + c^L_{j+3}(\frac{3}{4} + r_{33}) & 2c^L_{j+3}r_{34} \\ c^L_{j+1}(-\frac{1}{60} + r_{17}) + c^L_{j+4}(\frac{1}{60} + r_{41}) & c^L_{j+2}(\frac{3}{20} + r_{26}) + c^L_{j+4}(-\frac{3}{20} + r_{42}) & c^L_{j+3}(-\frac{3}{4} + r_{35}) + c^L_{j+4}(\frac{3}{4} + r_{43}) \\ \tau_R l_1 & \tau_R l_2 & \tau_R l_3 \end{bmatrix}$$

$$\begin{bmatrix} c^L_{j+1}(-\frac{1}{60} + r_{17}) + c^L_{j+4}(\frac{1}{60} + r_{41}) & \tau_R l_1 \\ c^L_{j+2}(\frac{3}{20} + r_{26}) + c^L_{j+4}(-\frac{3}{20} + r_{42}) & \tau_R l_2 \\ c^L_{j+3}(-\frac{3}{4} + r_{35}) + c^L_{j+4}(\frac{3}{4} + r_{43}) & \tau_R l_3 \\ 2c^L_{j+4}r_{44} & \tau_R l_4 \\ \tau_R l_4 & \beta_R - 2\tau_R \end{bmatrix}.$$

An accuracy of third-order at the donor grid points for the first derivative approximation $\tilde{D}_L\mathbf{u} = (-P_L^{-1}Q_L + \Upsilon_L)\mathbf{u}$ yields

$r_{14} = -2(10r_{11}+5r_{12}+2r_{13})$, $r_{15} = 45r_{11}+20r_{12}+6r_{13}$, $r_{16} = -36r_{11}-15r_{12}-4r_{13}$, $r_{17} = 10r_{11}+4r_{12}+r_{13}$,

$r_{23} = -10r_{21}-4r_{22}+r_{27}$, $r_{24} = 20r_{21}+6r_{22}-4r_{27}$, $r_{25} = -15r_{21}-4r_{22}+6r_{27}$, $r_{26} = 4r_{21}+r_{22}-4r_{27}$,

$r_{32} = -4r_{31}+r_{36}+4r_{37}$, $r_{33} = 6r_{31}-4r_{36}-15r_{37}$, $r_{34} = -4r_{31}+6r_{36}+20r_{37}$, $r_{35} = r_{31}-4r_{36}-10r_{37}$,

$r_{41} = r_{45}+4r_{46}+10r_{47}$, $r_{42} = -4r_{45}-15r_{46}-36r_{47}$, $r_{43} = 6r_{45}+20r_{46}+45r_{47}$, $r_{44} = -4r_{45}-10r_{46}-20r_{47}$.

Its substitution in K with Eqs. (5.67-5.69) provides,

$$K = \begin{bmatrix} \frac{11(c^L_{j+1}-\lambda)}{3} & \frac{1}{60}(-180c^L_{j+1} + 20c^L_{j+2} + 161\lambda - \mu) & \frac{1}{12}(18c^L_{j+1} - 2c^L_{j+3} - 17\lambda + \mu) \\ \frac{1}{60}(-180c^L_{j+1} + 20c^L_{j+2} + 161\lambda - \mu) & c^L_{j+2} + \frac{1}{15}(-17\lambda + 2\mu) & -c^L_{j+2} + c^L_{j+3} + \frac{9(\lambda-\mu)}{20} \\ \frac{1}{12}(18c^L_{j+1} - 2c^L_{j+3} - 17\lambda + \mu) & -c^L_{j+2} + c^L_{j+3} + \frac{9(\lambda-\mu)}{20} & \frac{1}{15}(-15c^L_{j+3} - 2\lambda + 17\mu) \\ \frac{1}{60}(-20c^L_{j+1} + 20c^L_{j+4} + 19(\lambda - \mu)) & \frac{1}{12}(2c^L_{j+2} - 18c^L_{j+4} - \lambda + 17\mu) & \frac{1}{60}(-20c^L_{j+3} + 180c^L_{j+4} - \lambda - 161\mu) \\ \tau_R l_1 & \tau_R l_2 & \tau_R l_3 \end{bmatrix}$$

$$\begin{bmatrix} \frac{1}{60}(-20c_{j+1}^L + 20c_{j+4}^L + 19(\lambda-\mu)) & \tau_R l_1 \\ \frac{1}{12}(2c_{j+2}^L - 18c_{j+4}^L - \lambda + 17\mu) & \tau_R l_2 \\ \frac{1}{60}(-20c_{j+3}^L + 180c_{j+4}^L - \lambda - 161\mu) & \tau_R l_3 \\ -\frac{11}{3}(c_{j+4}^L - \mu) & \tau_R l_4 \\ \tau_R l_4 & \beta_R - 2\tau_R \end{bmatrix}.$$

To prove $\frac{d}{dt}||\mathbf{w}||_H^2 \leq 0$, we need to show that the above symmetric matrix K is negative semidefinite. Substituting,

$$c_{j+2}^L = \frac{1}{20}(180c_{j+1}^L - 161\lambda + \mu), \quad c_{j+3}^L = \frac{1}{2}(18c_{j+1}^L - 17\lambda + \mu), \quad c_{j+4}^L = \frac{1}{20}(20c_{j+1}^L - 19\lambda + 19\mu),$$

in K simplifies the matrix to,

$$K = \begin{bmatrix} \frac{11(c_{j+1}^L - \lambda)}{3} & 0 & 0 & 0 & \tau_R l_1 \\ 0 & 9c_{j+1}^L + \frac{1}{60}(-551\lambda + 11\mu) & 0 & 0 & \tau_R l_2 \\ 0 & 0 & -9c_{j+1}^L + \frac{1}{30}(251\lambda + 19\mu) & 0 & \tau_R l_3 \\ 0 & 0 & 0 & -\frac{11}{60}(20c_{j+1}^L - 19\lambda - \mu) & \tau_R l_4 \\ \tau_R l_1 & \tau_R l_2 & \tau_R l_3 & \tau_R l_4 & \beta_R - 2\tau_R \end{bmatrix}. \tag{5.70}$$

From Eq. (5.57) for $\alpha_L \in [0,1]$ we have,

$$l_1,\, l_4 \,\in\, [-\tfrac{1}{9\sqrt{3}}, 0], \qquad l_2,\, l_3 \,\in\, [0,1], \qquad (\sum_{i=1}^{4}|l_i|)_{max} = \tfrac{5}{4}.$$

Use of Gershgorin circle theorem on matrix K provides all the admissible values of c_{j+1}^L, λ, μ, β_R and τ_R for $\alpha_L \in [0,1]$. One such set of values used in this report is,

$$\lambda = \frac{2143}{1440}, \quad \mu = \frac{1439}{1440}, \quad c_{j+1}^L = \frac{659}{450}, \quad \beta_R = \frac{11\sqrt{3}}{640}, \quad \tau_R = \frac{11\sqrt{3}}{480}.$$

5.2 Numerical Results

In this section, we discuss the numerical results for the overset method (4.19)–(4.20) and its extension to solve the Euler equations.

5.2.1 Scalar Advection Problem

We solve the advection problem discussed in section 4.3.1. The domain $x \in [-1,1]$ is split into the left and the right overlapping subdomains, $x_L \in [-1,0]$ and $x_R \in [-\frac{15}{2}h_L, 1]$, where h_L denotes the grid spacing on

the left subdomain. Figure 5.6 shows the solution at different times to the above problem with the $2-4-2$ SBP first derivative approximation using $\lambda = \frac{61}{20}$, $\mu = \frac{1}{20}$, $\beta_R = \frac{3}{4}$ and $\tau_R = 1$ in (5.59). Figure 5.7 shows the eigenvalues of the system matrix. Table 5.1 shows the error (ε) and the convergence rate with the $1-2-1$, $2-4-2$ and the $3-6-3$ SBP first derivative approximation. $p = \frac{1}{4}$ and $y = \frac{1}{20}$ in (5.30) was used for the computation with the $1-2-1$ operators, $\lambda = \frac{61}{20}$, $\mu = \frac{1}{20}$, $\beta_R = \frac{3}{4}$ and $\tau_R = 1$ in (5.59) was used for the computation with the $2-4-2$ operators and $\lambda = \frac{2143}{1440}$, $\mu = \frac{1439}{1440}$, $c^L_{j+1} = \frac{659}{450}$, $\beta_R = \frac{11\sqrt{3}}{640}$ and $\tau_R = \frac{11\sqrt{3}}{480}$ in (5.66) was used for the computation with the $3-6-3$ operators. For all calculations, the classical fourth-order Runge-Kutta (RK4) method was used for the temporal integration. The convergence rate in each case asymptotes to a value one order higher than the order of accuracy of the boundary stencils, consistent with the theory in Gustafsson (1975).

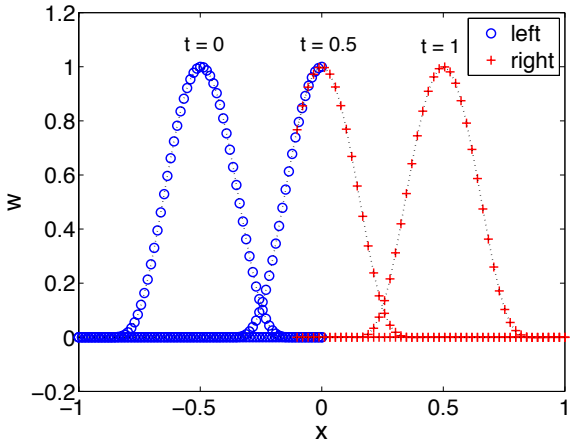

Figure 5.6: Solution to problem (4.29) at times t = 0, 0.5 and 1. Blue circles show the solution on the left domain and red pluses on the right domain.

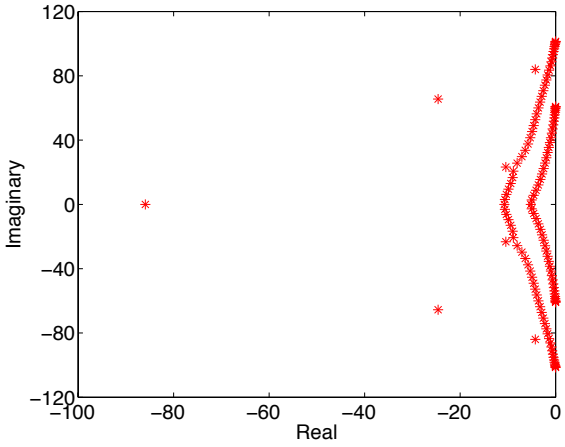

Figure 5.7: Eigenvalues of the system matrix M with 75 grid points on the left domain and 50 grid points on the right domain.

	$1-2-1$		$2-4-2$		$3-6-3$	
N	$\log_{10}\|\varepsilon\|_H$	Rate	$\log_{10}\|\varepsilon\|_H$	Rate	$\log_{10}\|\varepsilon\|_H$	Rate
20	-1.393317		-1.890376		-1.834638	
40	-2.096629	2.294	-3.076089	3.868	-3.320550	4.847
80	-2.767374	2.208	-4.329113	4.125	-4.766798	4.760
160	-3.408065	2.119	-5.580261	4.137	-6.146200	4.562
320	-4.030452	2.063	-6.762682	3.919	-7.464454	4.369
640	-4.642814	2.032	-7.846195	3.595	-8.740561	4.234

Table 5.1: Log_{10}(error) and the convergence rate with the $1-2-1$, $2-4-2$ and $3-6-3$ SBP first derivative approximation. Error calculations performed at $t_f = 0.5$ with $2N$ grid points on the left domain and N on the right domain.

5.2.2 Inviscid Burgers' Equation

We solve the inviscid Burgers' equation with an initial Gaussian pulse, as discussed in Section 4.3.2. Figure 5.8 shows the solution at different times on a domain $x \in [-1, 1]$ with the overlapping subdomains, $x_L \in [-1, 0]$ and $x_R \in [-\frac{15}{2}h_L, 1]$. Table 5.2 shows the convergence of the method with the $1-2-1$, $2-4-2$ and the $3-6-3$ SBP first derivative approximations. t_f denotes the time at which the error was computed for each refinement.

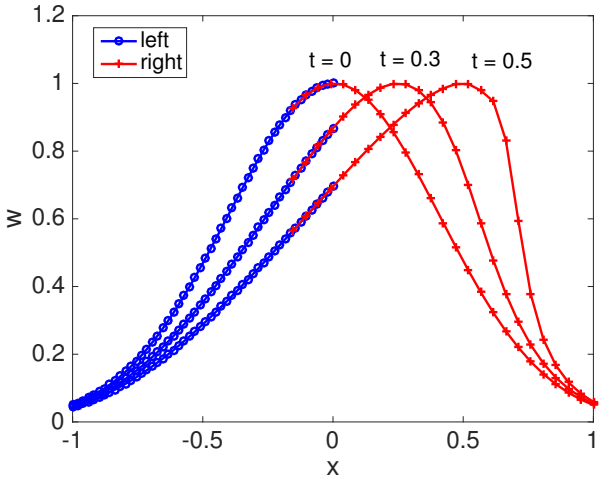

Figure 5.8: Solution to the problem (4.32).

	$1-2-1$		$2-4-2$		$3-6-3$	
N	$\log_{10}\|\|\boldsymbol{\varepsilon}\|\|_2$	Rate	$\log_{10}\|\|\boldsymbol{\varepsilon}\|\|_2$	Rate	$\log_{10}\|\|\boldsymbol{\varepsilon}\|\|_2$	Rate
20	-2.541474		-3.621003		-3.762557	
40	-3.203759	2.160	-4.884568	4.122	-5.289465	4.981
80	-3.831964	2.068	-5.996491	3.660	-6.699774	4.643
160	-4.447700	2.036	-6.995166	3.303	-8.031767	4.385
320	-5.056985	2.019	-7.954203	3.172	-9.297876	4.187

Table 5.2: $\log_{10}(L^2$-error) and the convergence rate with the $1-2-1$, $2-4-2$ and the $3-6-3$ SBP first derivative approximation. Error calculations performed at $t_f = 0.25$ with $2N$ grid points on the left domain and N on the right domain.

5.3 Extension to the two-dimensional Euler Equations

In this section, we discuss the extension of the method (4.19)-(4.20) to solve the two-dimensional Euler equations. The extension to three-dimensions follows a similar approach. The two-dimensional Euler equations in generalized coordinates are given by

$$\frac{\partial Q}{\partial \tau} + \frac{\partial F}{\partial \xi} + \frac{\partial G}{\partial \eta} = 0, \tag{5.71}$$

$$Q = \frac{1}{J}\begin{bmatrix} \rho \\ \rho u \\ \rho v \\ \rho E \end{bmatrix}, \qquad F = \frac{1}{J}\begin{bmatrix} \rho U \\ \rho u U + \xi_x p \\ \rho v U + \xi_y p \\ \rho E U + \xi_{x_i} u_i p \end{bmatrix}, \qquad G = \frac{1}{J}\begin{bmatrix} \rho V \\ \rho u V + \eta_x p \\ \rho v V + \eta_y p \\ \rho E V + \eta_{x_i} u_i p \end{bmatrix}, \tag{5.72}$$

$$U = \xi_t + \xi_x u + \xi_y v, \qquad V = \eta_t + \eta_x u + \eta_y v,$$

$$\rho E = \frac{p}{\gamma - 1} + \rho\left(\frac{u^2 + v^2}{2}\right).$$

The coordinate transformation between the physical domain $\mathbf{x} = (x, y)$ and the computational domain $\boldsymbol{\xi} = (\xi, \eta)$ is $\boldsymbol{\xi} = \boldsymbol{\Xi}(\mathbf{x}, t)$ with the inverse transformation $\mathbf{x} = \mathbf{X}(\boldsymbol{\xi}, \tau)$ and the metric Jacobian $J = \det(\partial\boldsymbol{\xi}/\partial\mathbf{x})$ $= (x_\xi y_\eta - x_\eta y_\xi)^{-1}$. We assume the time to be invariant, therefore, $\tau = t$. Here, u, v are the Cartesian velocity components, ρ denotes the density, p the pressure and E is the total energy per unit mass.

5.3.1 Numerical Discretization

To make this discussion concrete, we consider the two-grid overset configuration on the rectangular domain $[-1,1]\times[-0.5,0.5]$ shown in Figure 5.9. The left domain $[-1,0]\times[-0.5,0.5]$ (shown in blue) and the right domain $[-0.13,1]\times[-0.5,0.5]$ (shown in green) overlap. A numerical boundary condition (via interpolation) needs to be imposed at the grid points on the right boundary ($x=0$) of the left domain and the left boundary ($x=-0.13$) of the right domain. The region in red denotes the donor grid points for interpolation of solution from left to the right grid and, similarly, the region in orange denotes the donor grid points for interpolation from right to the left grid. Following the notation used in Nordström *et al.* (2009); Svärd *et al.* (2007), the solution field is denoted by $q_{ijl}^{L,R}$, where the first two subscripts i and j denote the ξ and η index of the grid point and the last index $0\leq l\leq 3$ denotes the elements (different fields) of the vector Q. The superscript L,R denotes the domain (left or right) to which the grid function belongs. With this convention, we define a composite vector $\mathbf{Q}^{L,R}=(q_{000}^{L,R},\, q_{001}^{L,R},\, ...,\, q_{N_\xi N_\eta 3}^{L,R})^T$, where $N_\xi^{L,R}+1$ and $N_\eta^{L,R}+1$ are the number of grid points in the ξ and η direction of the left and the right grid, respectively. The difference operators are given by,

$$\mathbf{D}_\xi^{L,R}=D_\xi^{L,R}\otimes I_\eta^{L,R}\otimes I_4,\qquad \mathbf{D}_\eta^{L,R}=I_\xi^{L,R}\otimes D_\eta^{L,R}\otimes I_4,$$

where the matrix in the first position in the Kronecker product is of size $(N_\xi^{L,R}+1)\times(N_\xi^{L,R}+1)$, the one in the second position is of size $(N_\eta^{L,R}+1)\times(N_\eta^{L,R}+1)$, and the one in the third position is 4×4. I denotes an identity matrix with a size consistent with its position in the Kronecker product. D_ξ and D_η denote the SBP first derivative approximation. The norm matrices are denoted as,

$$\mathbf{P}_\xi^{L,R}=P_\xi^{L,R}\otimes I_\eta^{L,R}\otimes I_4,\qquad \mathbf{P}_\eta^{L,R}=I_\xi^{L,R}\otimes P_\eta^{L,R}\otimes I_4,$$

$$\mathbf{H}_\xi^{L,R}=H_\xi^{L,R}\otimes I_\eta^{L,R}\otimes I_4,\qquad \mathbf{H}_\eta^{L,R}=I_\xi^{L,R}\otimes H_\eta^{L,R}\otimes I_4,$$

and define,

$$\mathbf{E}_{0_\xi}^{L,R}=E_0^{L,R}\otimes I_\eta^{L,R}\otimes I_4,\qquad \mathbf{E}_{\mathbf{N}_\xi}^{L,R}=E_N^{L,R}\otimes I_\eta^{L,R}\otimes I_4,$$

$$\mathbf{E}_{0_\eta}^{L,R}=I_\xi^{L,R}\otimes E_0^{L,R}\otimes I_4,\qquad \mathbf{E}_{\mathbf{N}_\eta}^{L,R}=I_\xi^{L,R}\otimes E_N^{L,R}\otimes I_4,$$

where $E_0^{L,R}=\mathrm{diag}(1,\,0\,,\,....\,,\,0)$ and $E_N^{L,R}=\mathrm{diag}(0,\,....\,,\,0,\,1)$ are of appropriate sizes based on their position in the Kronecker product. The numerical boundary condition can then be written as,

$$\hat{\mathbf{Q}}^L=\mathbf{T}^R\mathbf{Q}^R\qquad\text{and}\qquad\hat{\mathbf{Q}}^R=\mathbf{T}^L\mathbf{Q}^L,$$

where $\mathbf{T}^R$ is of size $4(N_\xi^L+1)(N_\eta^L+1)\times 4(N_\xi^R+1)(N_\eta^R+1)$ and $\mathbf{T}^L$ is of size $4(N_\xi^R+1)(N_\eta^R+1)\times 4(N_\xi^L+1)(N_\eta^L+1)$, and their rows contain the interpolation coefficients for the respective grid points.

The semi-discretization for the left and the right domain in Figure 5.9, including the interpolation in the overlapping region but not considering the physical boundary conditions, is given by

$$\frac{d\mathbf{Q}^L}{d\tau} = -\mathbf{D}_\xi^L\mathbf{F}^L - \mathbf{D}_\eta^L\mathbf{G}^L - \tau_{_L}(\mathbf{H}_\xi^L)^{-1}\mathbf{E}_{\mathbf{N}_\xi}^L\mathbf{K}_\xi^{L-}(\mathbf{Q}^L-\hat{\mathbf{Q}}^L) + \mathbf{K}_\xi^{L+}\boldsymbol{\Upsilon}^L\mathbf{Q}^L, \tag{5.73}$$

$$\frac{d\mathbf{Q}^R}{d\tau} = -\mathbf{D}_\xi^R\mathbf{F}^R - \mathbf{D}_\eta^R\mathbf{G}^R - \tau_R(\mathbf{H}_\xi^R)^{-1}\mathbf{E}_{\mathbf{0}_\xi}^R\mathbf{K}_\xi^{R+}(\mathbf{Q}^R-\hat{\mathbf{Q}}^R) + \mathbf{K}_\xi^{R-}\boldsymbol{\Upsilon}^R\mathbf{Q}^R. \tag{5.74}$$

For discussions hereafter, we shall refer to the method (5.73)–(5.74) as the SAT method with dissipation. The SAT method without the dissipation term was discussed in Section 4.3.3. $\mathbf{K}_\kappa^{L,R}$ ($\kappa=\xi$ or η) denotes the similarity transform of the flux Jacobian matrix (see Pulliam & Chaussee, 1981) and,

$$\mathbf{K}_\kappa^{L,R\pm} = (\mathbf{S}_\kappa^{L,R})\left(\frac{\left|\boldsymbol{\Lambda}_\kappa^{L,R}\right| \pm \boldsymbol{\Lambda}_\kappa^{L,R}}{2}\right)(\mathbf{S}_\kappa^{L,R})^{-1}$$

ensures that only the incoming characteristics are penalized at the interface and only the outgoing characteristics are subjected to numerical dissipation, consistent with the one-dimensional semi-discretization (4.6)-(4.7). The eigenvalue and the eigenvector matrices are given by,

$$\boldsymbol{\Lambda}_\kappa^{L,R} = I_\xi^{L,R}\otimes I_\eta^{L,R}\otimes\Lambda_\kappa, \qquad \mathbf{S}_\kappa^{L,R} = I_\xi^{L,R}\otimes I_\eta^{L,R}\otimes S_\kappa,$$

where the expressions for Λ_κ and S_κ can be found in Pulliam & Chaussee (1981). In all our calculations, we use the Roe-averaged quantities that satisfy $\mathbf{F}(\mathbf{Q})-\mathbf{F}(\hat{\mathbf{Q}}) = \mathbf{K}_\xi(\mathbf{Q},\hat{\mathbf{Q}})(\mathbf{Q}-\hat{\mathbf{Q}})$, to compute the eigenvectors and the eigenvalues, which may be beneficial in an extension of the method to accommodate for discontinuous solutions. For the grid configuration shown in Fig. 5.9, the operators in the dissipation term of the SAT method is given by $\boldsymbol{\Upsilon}^{L,R} = \Upsilon^{L,R}\otimes I_\eta^{L,R}\otimes I_4$, where the structure of the matrix $\Upsilon^{L,R}$ is shown in Eqs. (5.8), (5.58) and (5.65) for the interior overlap configuration of the second, third and the fourth-order method, respectively. The one-dimensional analysis in Sec. 5.1.1 showed that for time-stability the non-zero rows in $\Upsilon^{L,R}$ should correspond to the donor grid points used for interpolation at the interface. Using that as a guideline for the overset configuration in Fig. 5.9, the dissipation should be added to the region shown in red/orange in the figure. The red/orange band is two-points wide for the second-order (bilinear interpolation) and four-points wide for the third- and the fourth-order (bicubic interpolation) methods. In all our calculations, we use the skew-symmetric split form of the convective derivatives (Pirozzoli, 2011).

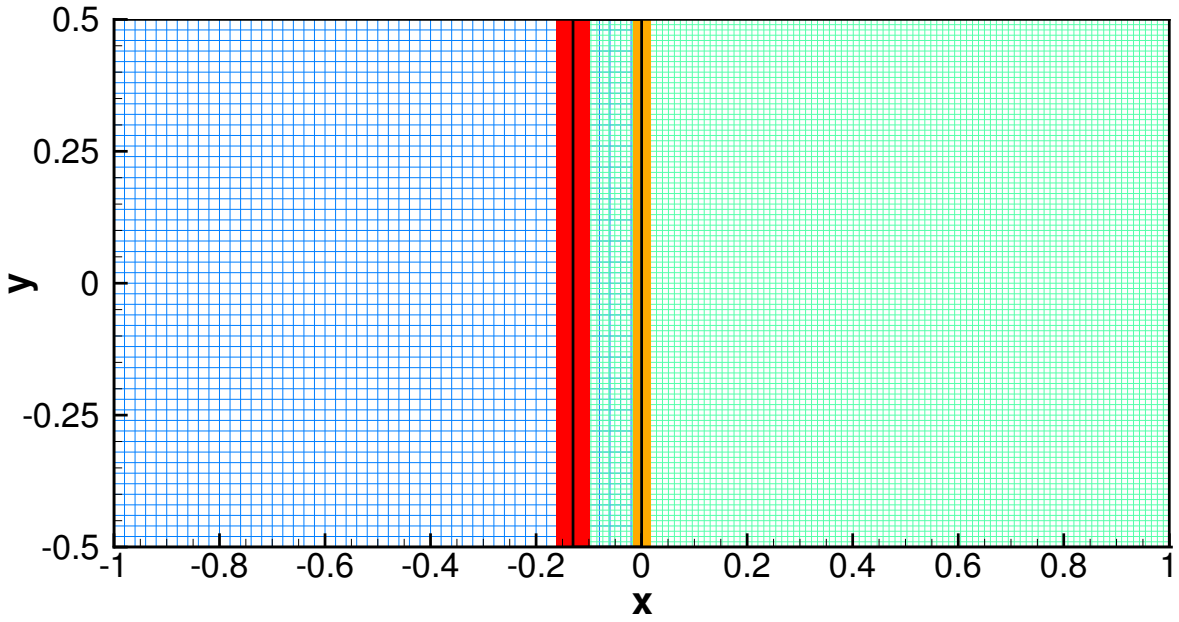

Figure 5.9: Two-grid overset configuration with 51×51 grid points on the left domain and 101×101 grid points on the right domain. The red and orange bands denote the donor grid points on the left and right grid, respectively.

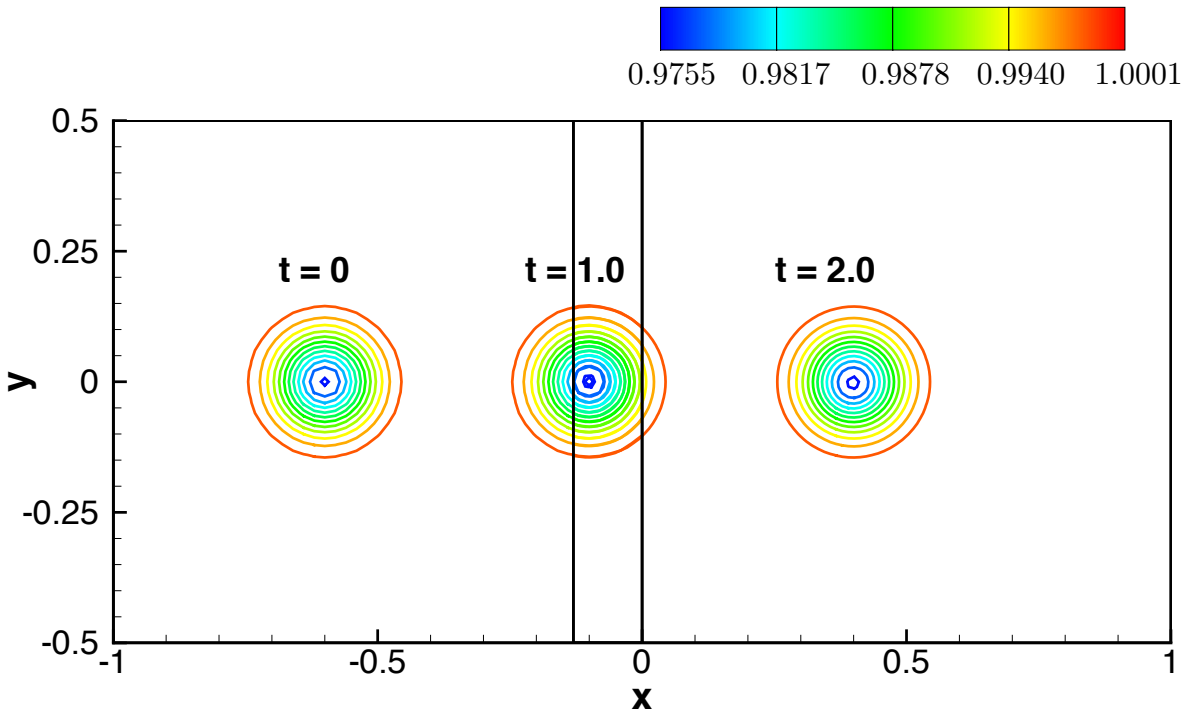

Figure 5.10: Density contours for the convection of vortex over time obtained from the third order version of the SAT method with 51×51 grid points on the left domain and 101×101 grid points on the right.

5.3.2 Isentropic Vortex Convection

To demonstrate the performance of the method, we solve the two-dimensional Euler equations (Eq. (5.71)) for the propagation of a compressible isentropic vortex with the exact solution given by Eq. (4.33). Figure 5.10 shows the density contours at different times for the grid configuration shown in Figure 5.9 for $u_0 = 0.5$. The third-order version of the SAT method with dissipation, using operators corresponding to $\beta_R = \frac{3}{4}$, $\tau_R = 1$, $\lambda = \frac{61}{20}$ and $\mu = \frac{1}{20}$ in Theorem 5.4, was used with the classical fourth-order Runge-Kutta (RK4) method with a CFL of 0.25 for time integration. Figure 5.11 shows the density and the entropy error on the centerline ($y = 0$) at $t = 2$ for the "injection method" and the SAT method with and without the dissipation term. When the vortex crosses over from the left domain to the right it generates numerical reflections that travel leftward from the right boundary of the left domain. These reflections are subsequently weakened by the dissipative term in (5.73) and therefore we see lower error on the left domain in Figure 5.11 for the SAT method with dissipation. The error on the right domain, where the vortex resides at $t = 2$, is dominated by the truncation error of the convection terms in the bulk of the domain and therefore the error profiles for different methods are similar to each other and it is harder to distinguish the interface treatment errors between the methods. For this short-time simulation, the errors from the "injection method" are similar to those of the SAT method without dissipation. Next, we examine the long-time performance of the methods.

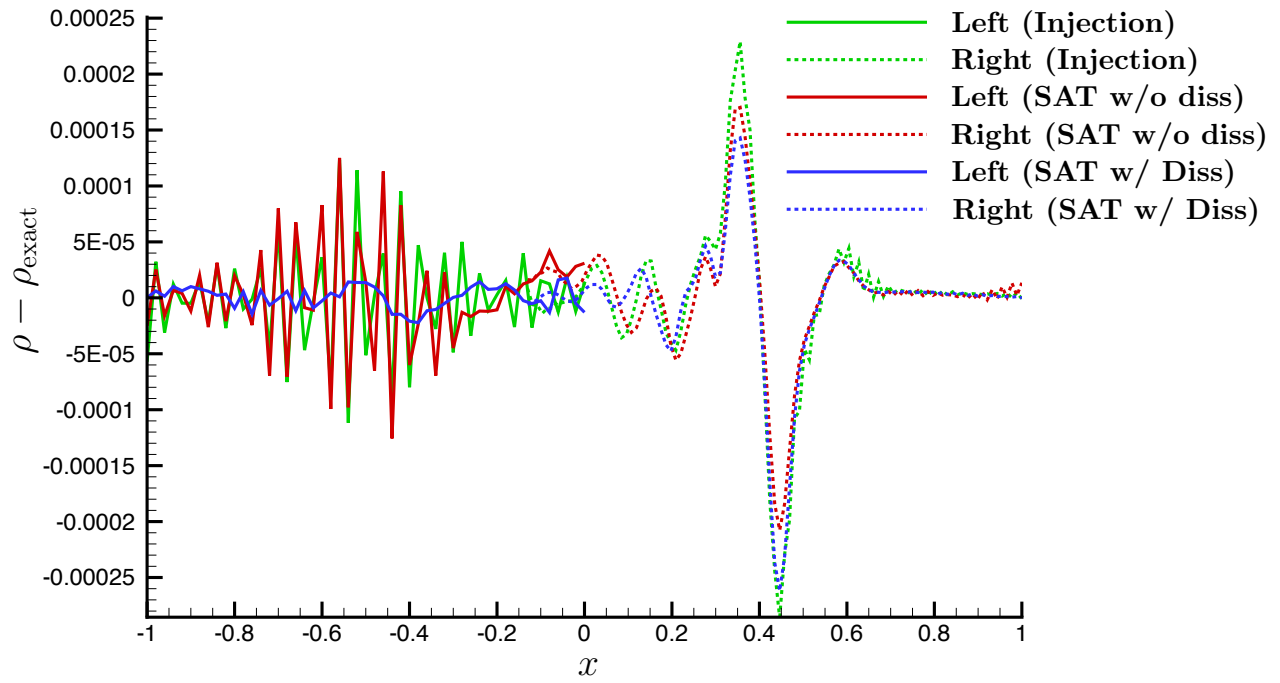

(a)

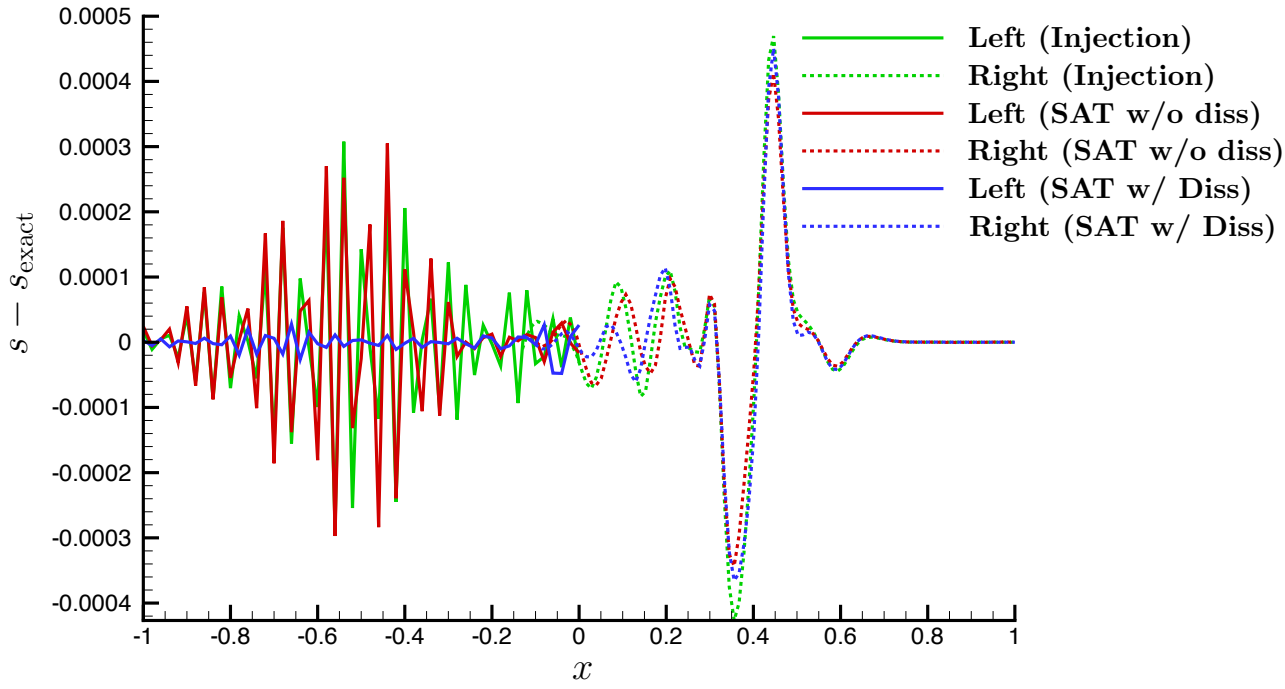

(b)

Figure 5.11: Centerline error comparison of the "injection method" and the SAT method with and without the dissipative term at $t = 2.0$. (a) Density error, (b) Entropy error.

A common difficulty with overset grid methods is their inability to prevent repeated numerical reflections

off sub-domain boundaries from growing unboundedly in time and therefore we need to assess the long-time behavior of the overset methods. In Section 4.3.3, the long-time performance of the method (5.73)–(5.74) without the dissipation term was examined. We consider the same overset configuration as shown in Figure 4.15 with $\theta = \frac{\pi}{4}$ and a base Cartesian grid of size 201×201 covered by a square patch (rotated Cartesian grid) of size 101×101. Figure 5.12 shows the donor grid points for interpolation, where the dissipation is added, on each grid. Figures 5.13 and 5.14 show density, entropy, velocity magnitude and pressure error comparisons between the "injection method" of interface treatment and the SAT method with and without the dissipation for advection at a supersonic ($u_0 = 2.0$, $M_0 \approx 1.69$) and subsonic ($u_0 = 0.5$, $M_0 \approx 0.42$) velocity, respectively. See Appendix C for comments on the performance of the SAT method with dissipation in Figures 5.13 and 5.14.

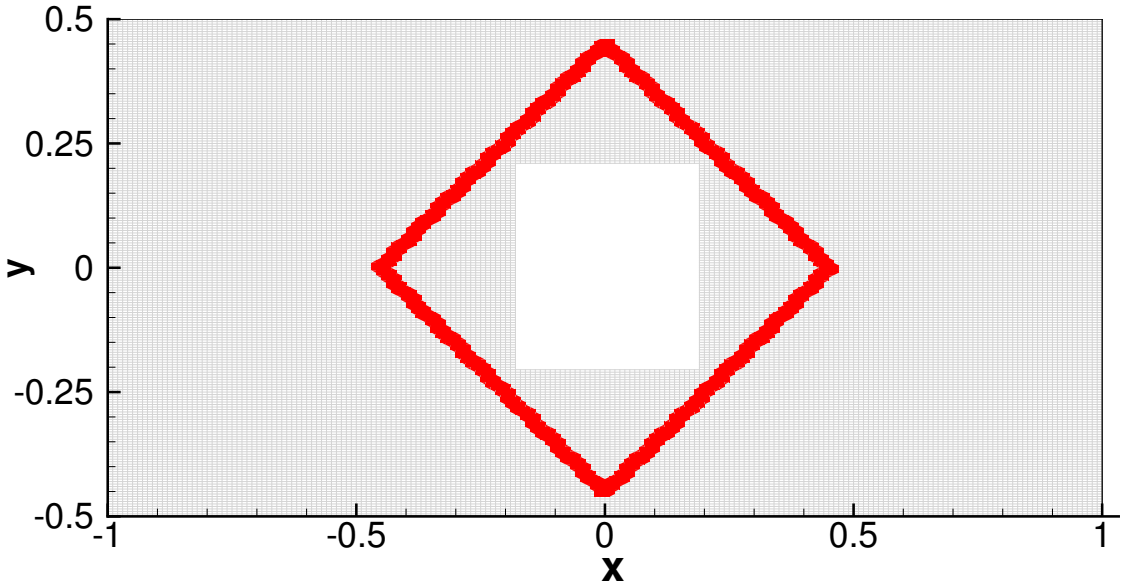

(a)

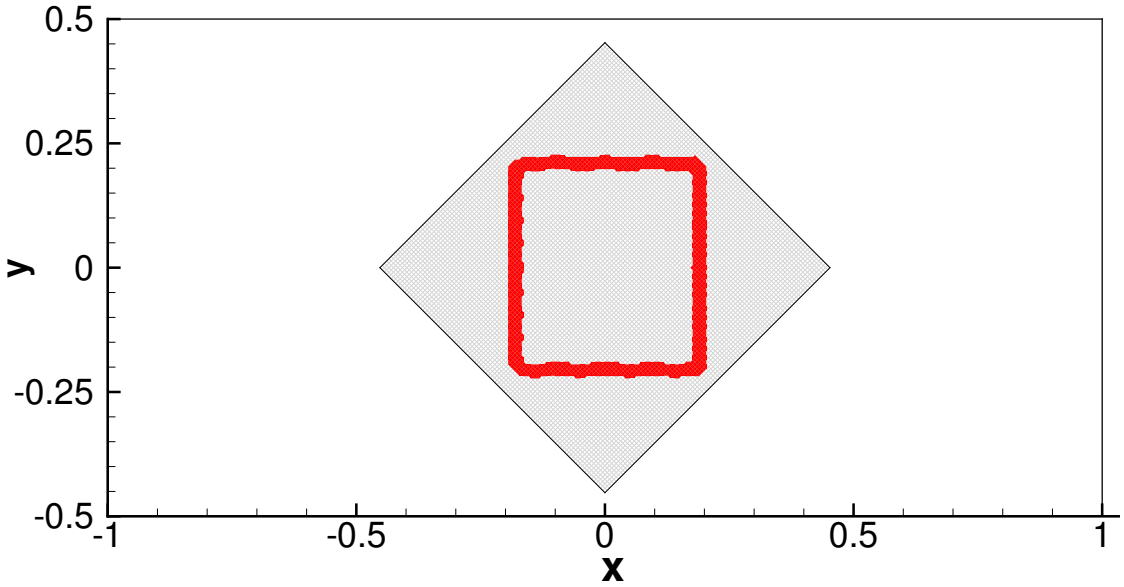

(b)

Figure 5.12: Red bands denote the grid points where dissipation is added. (a) Base grid, (b) Patch grid.

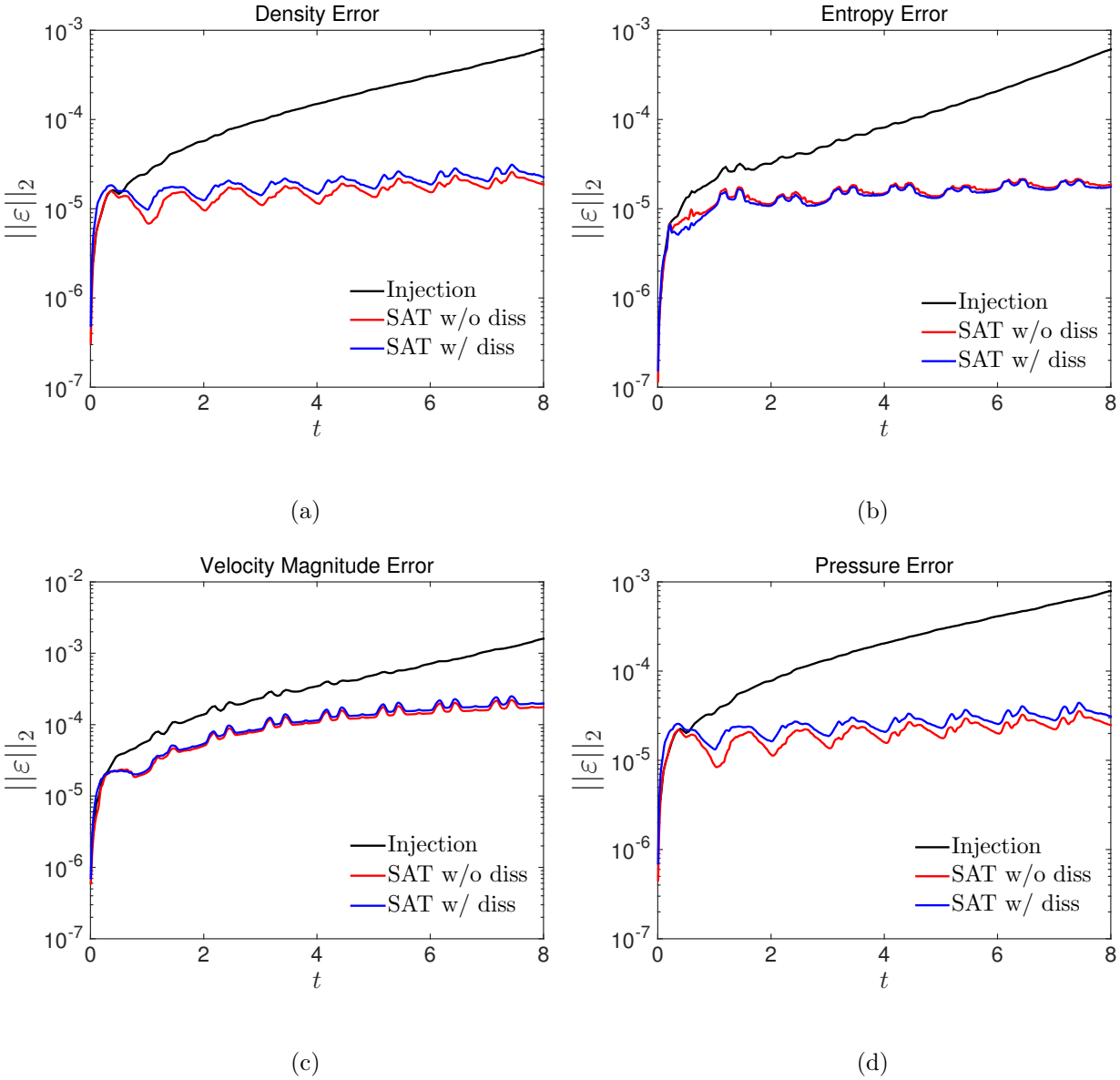

Figure 5.13: Error comparison of the injection method against the SAT method with and without dissipation for $u_0 = 2.0$. (a) Density error, (b) Entropy error, (c) Velocity magnitude error, (d) Pressure error.

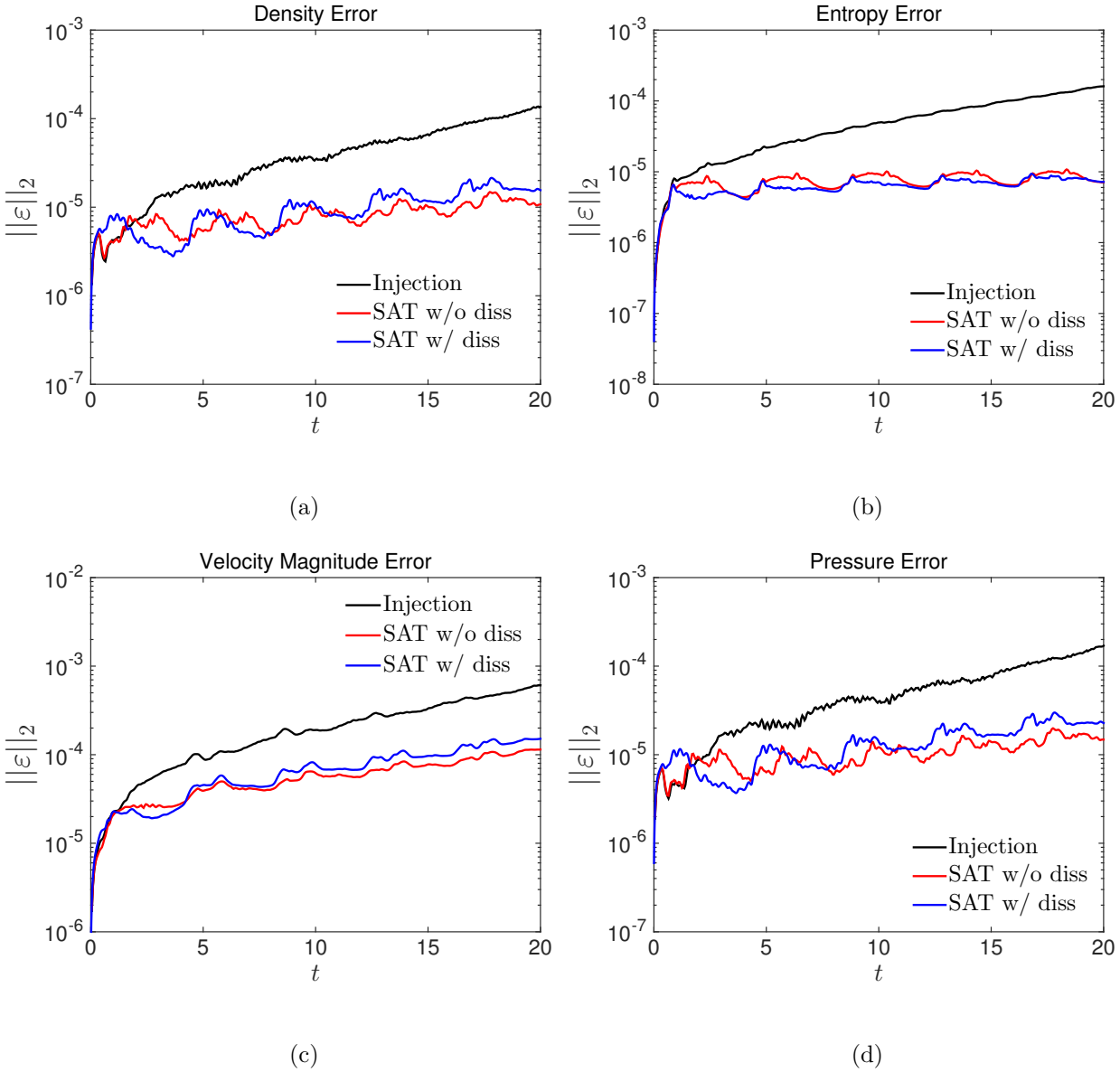

Figure 5.14: Error comparison of the injection method against the SAT method with and without dissipation for $u_0 = 0.5$. (a) Density error, (b) Entropy error, (c) Velocity magnitude error, (d) Pressure error.

5.3.3 Acoustic Scattering

To examine the performance of the methods on a curvilinear grid, we determine the scattered sound field generated from a time-periodic acoustic source reflecting off a circular cylinder. The Euler equations (5.71) are solved with a source term given by

$$\frac{\partial Q}{\partial \tau} + \frac{\partial F}{\partial \xi} + \frac{\partial G}{\partial \eta} = S,$$

where

$$S = \begin{bmatrix} 0 & 0 & 0 & \frac{1}{4}e^{-\ln 2\left(\frac{(x-4)^2+y^2}{(0.2)^2}\right)} \sin \omega t \end{bmatrix}^T . \tag{5.75}$$

Dimensionless variables with respect to the length scale = cylinder diameter, D^*, velocity scale = speed of sound, c_0^*, density scale = undisturbed density, ρ_0^*, and pressure scale = $\rho_0^* c_0^{*2}$ are used, where $*$ denotes the dimensional quantities. We consider a two-grid overset domain as shown in Figure 5.15. The Cartesian grid, on the domain $[-10, 10] \times [-10, 10]$, has 401×401 grid points whereas the polar grid, with an outer radius of 2, has 51 and 301 grid points in the radial and the azimuthal direction, respectively. The acoustic source is located at $(x_s, y_s) = (4, 0)$ and the solution of the resulting scattering problem, governed by the linearized Euler equations, is discussed in Tam & Hardin (1997) as Problem 1 of Category 1. The solution for pressure, with the source term (5.75), is given by

$$p(x, y, t) = (\gamma - 1)\ \mathrm{Im}(\hat{p}(x, y)e^{-i\omega t}),$$

where

$$\hat{p}(x, y) = p_i(x, y) + p_r(x, y).$$

p_i denotes the incident wave generated by the acoustic source, given by

$$p_i(x, y) = -\int_0^\infty \frac{i\omega}{4} e^{-b\xi^2} G(r_s, \xi) d\xi,$$

where $r_s = \sqrt{(x - x_s)^2 + (y - y_s)^2}$, $b = \frac{\ln 2}{(0.2)^2}$ and the Green's function is,

$$G(r_s, \xi) = \begin{cases} -\frac{\pi i}{2} \xi J_0(\omega\xi) H_0^{(1)}(\omega r_s), & 0 \le \xi \le r_s, \\ -\frac{\pi i}{2} \xi J_0(\omega r_s) H_0^{(1)}(\omega\xi), & r_s \le \xi \le \infty. \end{cases}$$

J_0 and $H_0^{(1)}$ denote the zeroth order Bessel and Hankel functions of the first kind, respectively. The reflected wave from the cylinder, p_r, is given by

$$p_r(r, \theta) = \sum_{k=0}^{\infty} C_k H_k^{(1)}(r\omega)\cos(k\theta),$$

where $H_k^{(1)}$ is the Hankel function of the first kind of order k and,

$$C_k = \frac{\epsilon_k}{\pi\omega[\frac{2k}{\omega}H_k^{(1)}(\omega/2) - H_{k+1}^{(1)}(\omega/2)]} \int_0^\pi B(\phi)\cos(k\phi)\,d\phi,$$

$\epsilon_0 = 1$ and $\epsilon_k = 2$ for $k \neq 0$. $B(\phi)$ denotes the boundary condition at the cylinder surface given by

$$B(\phi) = -\left.\frac{\partial p_i}{\partial r}\right|_{r=0.5} = \int_0^\infty \frac{i\omega}{4} e^{-b\xi^2} \left.\frac{\partial G}{\partial r}\right|_{r=0.5} d\xi.$$

For $(x_s, y_s) = (4, 0)$,

$$\left.\frac{\partial G}{\partial r}\right|_{r=0.5} = \begin{cases} \frac{\pi i}{2}\xi\omega J_0(\omega\xi)H_1^{(1)}(\omega r_{s0})\frac{1-8\cos(\phi)}{2r_{s0}}, & 0 \leq \xi \leq r_{s0} \\ \frac{\pi i}{2}\xi\omega J_1(\omega r_{s0})H_0^{(1)}(\omega\xi)\frac{1-8\cos(\phi)}{2r_{s0}}, & r_{s0} \leq \xi \leq \infty \end{cases}$$

where $r_{s0} = \sqrt{16.25 - 4\cos(\phi)}$.

Figures 5.16 and 5.17 show the surface plot of pressure perturbation from simulations performed using the injection method and the SAT method without dissipation term, respectively, at $t = t^* c_0^*/D^* \approx 30$ with $\omega = \omega^* D^*/c_0^* = \pi$ and the globally third-order accurate spatial discretization. The plots from injection method simulations clearly show non-physical perturbations at the inner boundary, where the overset interface treatment is applied. In contrast, the SAT method ensures smooth transfer of pressure perturbations from one domain to the other. Figure 5.18 shows the pressure perturbation with time at $x = 2$, $y = 0$ (an inner boundary point of polar grid) using the injection method as well as the SAT method with and without dissipation. Figure 5.19 shows the grid points where dissipation is added for the SAT method with dissipation. There is no noticeable difference between the results from the SAT methods, with/without dissipation, for this problem and they both match very well with the exact solution but the results from the injection method diverge for long-time simulations.

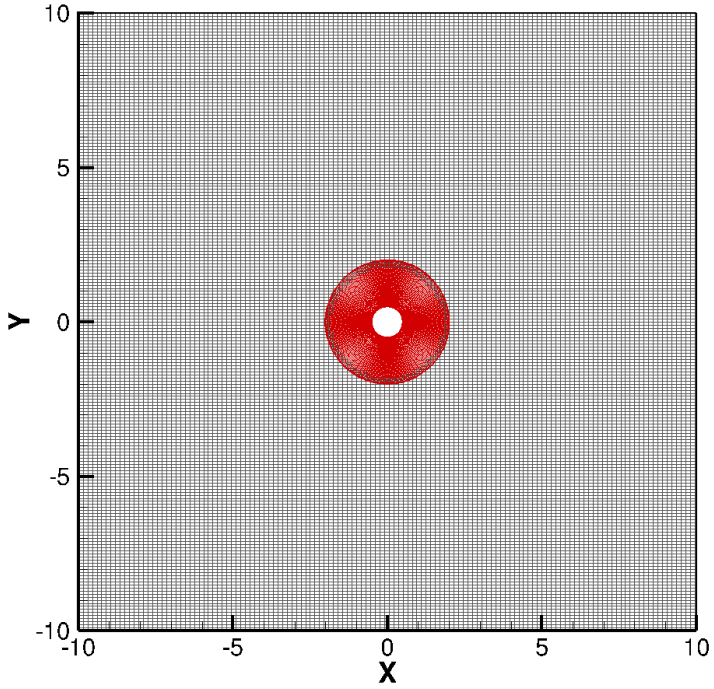

(a)

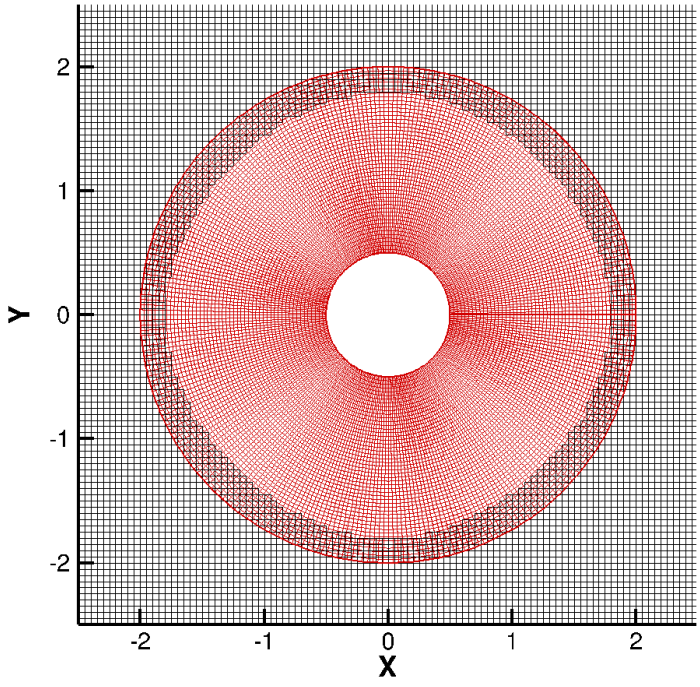

(b)

Figure 5.15: Overset domain for the acoustic scattering problem. (a) Circular cylinder with a body conforming polar grid (shown in red) overlapping on a Cartesian square grid (shown in gray), (b) Overlapping region showing the hole (inner boundary) on the Cartesian grid and the amount of overlap.

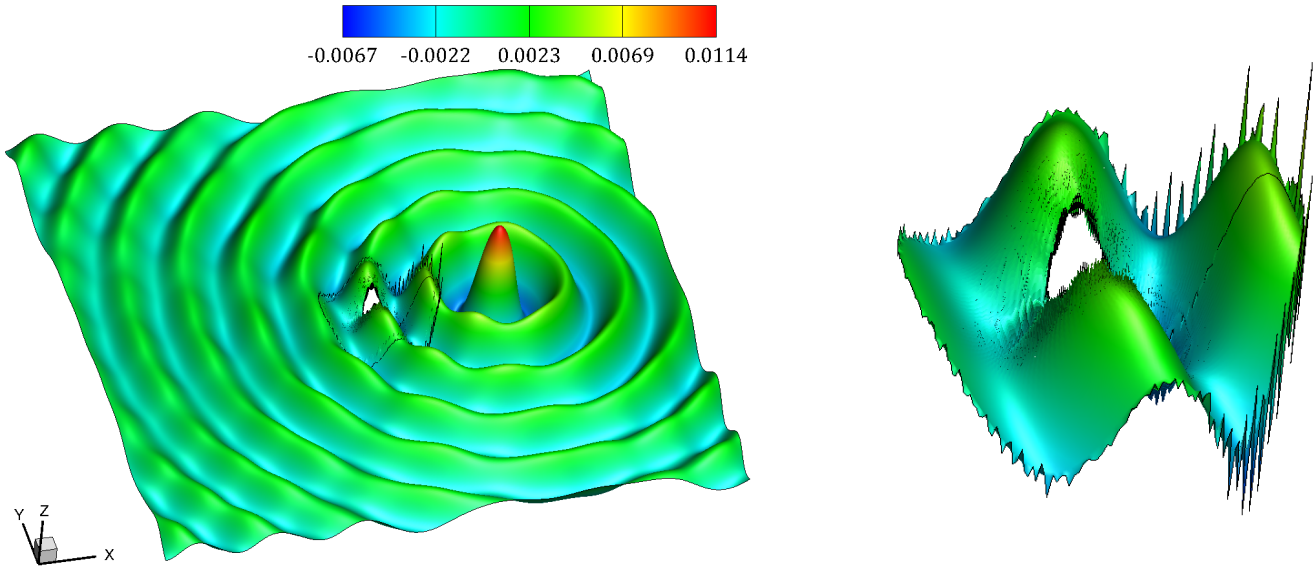

(a) (b)

Figure 5.16: Surface plot of pressure perturbation, p', using the injection method for overlapping interface treatment at $t \approx 30$. (a) Pressure perturbation on both domains, (b) Pressure perturbation on the polar grid.

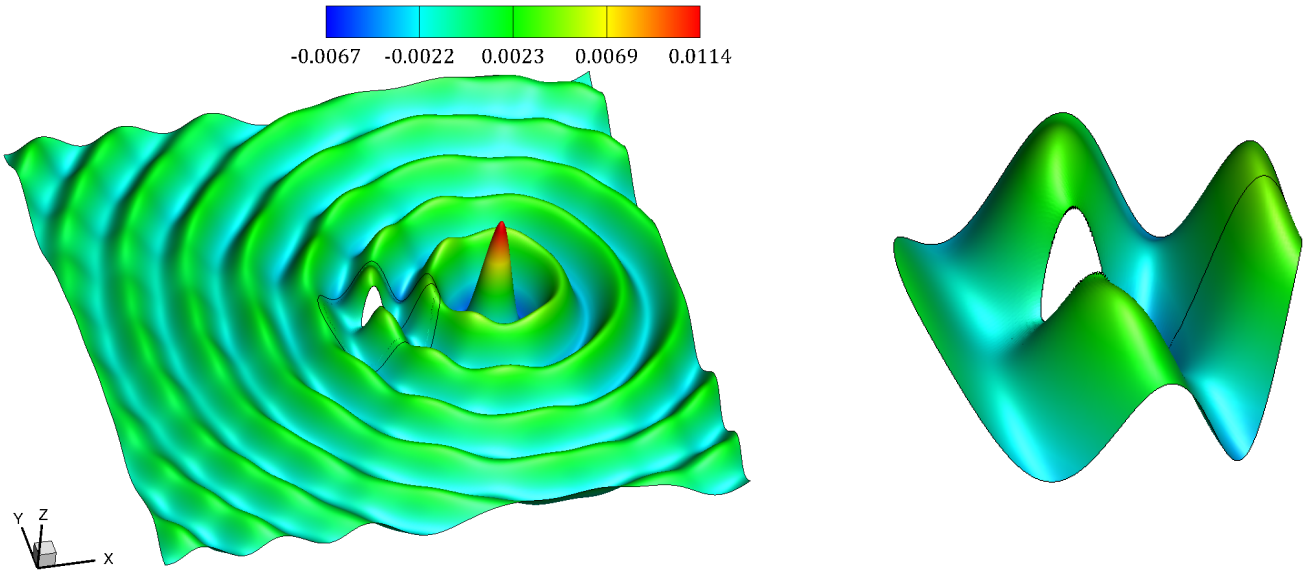

(a) (b)

Figure 5.17: Surface plot of pressure perturbation, p', using the SAT method without dissipation for overlapping interface treatment at $t \approx 30$. (a) Pressure perturbation on both domains, (b) Pressure perturbation on the polar grid.

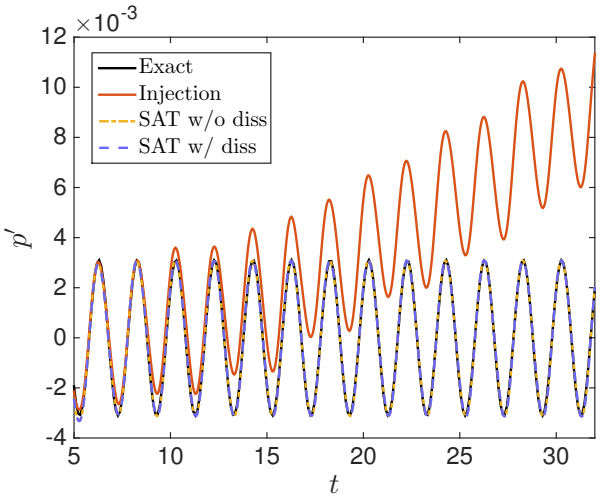

Figure 5.18: Time history of pressure perturbation at $x = 2$, $y = 0$ using different methods for overset interface treatment.

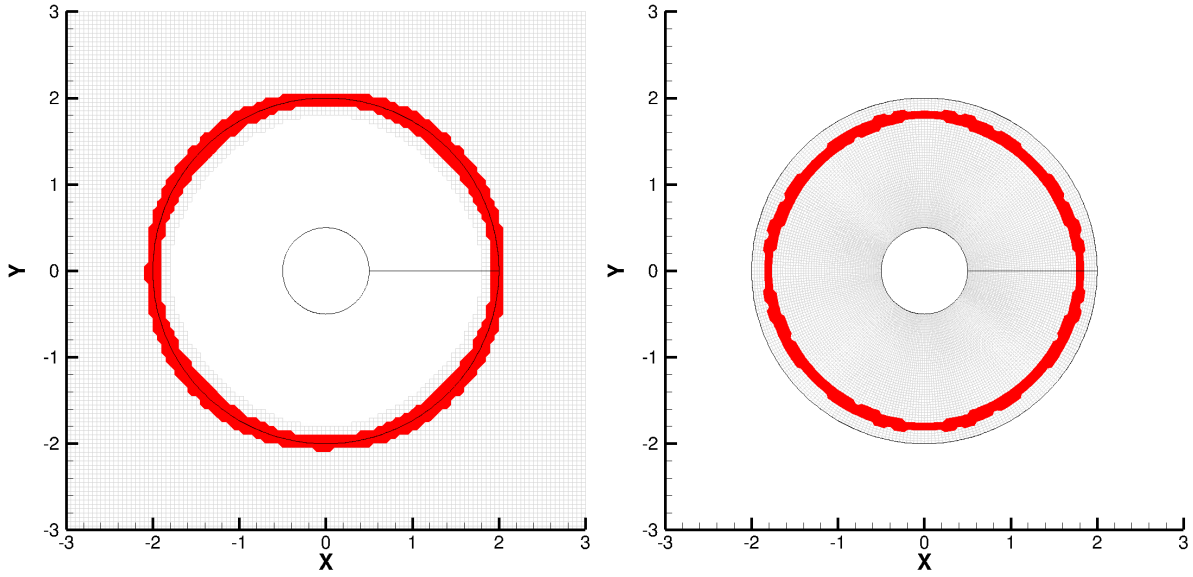

(a) (b)

Figure 5.19: Red-colored band denotes the interpolation donor grid points where dissipation is added for the SAT method with dissipation. (a) Cartesian grid, (b) Polar grid.

Chapter 6

Conservation Analysis

In this chapter, we discuss the conservation properties of the overset method presented in the previous chapter. More generally, let us consider a hyperbolic system given by

$$\frac{\partial q}{\partial t} + \nabla \cdot F = 0, \qquad \text{on} \qquad \mathbf{x} \in \Omega \subset \mathbb{R}^d, \;\; t \geq 0. \tag{6.1}$$

where $q : \Omega \times \mathbb{R} \to \mathbb{R}^k$ such that $q = \begin{bmatrix} q^1 & \cdots & q^k \end{bmatrix}^T$ and $F_j = \begin{bmatrix} F_j^1 & \cdots & F_j^k \end{bmatrix}^T$ for $1 \leq j \leq d$. If F_j^i are non-linear functions of q, for example the Euler equations, the solution of the conservation equations can develop discontinuities such as shocks. In such a case one seeks weak (or generalized) solutions to (6.1) that satisfy the integral form of the conservation law

$$\frac{d}{dt}\int_{\Omega} q \; dx + \int_{\partial\Omega} F \cdot n \; dS = 0. \tag{6.2}$$

It can be shown that if q is a weak solution across a discontinuity then the speed s of the discontinuity is given by the Rankine-Hugoniot condition (see Lax, 1973)

$$s = \frac{[\![F^i]\!] \cdot n}{[\![q^i]\!]},$$

where the bracket $[\![\cdot]\!]$ denotes the jump in the quantity across the discontinuity and n denotes the direction of propagation of the discontinuity. Therefore, for a numerical scheme to correctly estimate the speed of propagation of the discontinuity it must discretely satisfy Eq. (6.2).

For a one-dimensional version of Eq. (6.1),

$$q_t + f_x = 0, \tag{6.3}$$

on a single domain $x \in [a, b]$ as shown in Figure 6.1, Eq. (6.2) becomes,

$$\frac{d}{dt} \int_a^b q \; dx = f(a) - f(b), \tag{6.4}$$

i.e., the time rate of change of the conserved quantity $S_1 = \int_a^b q \; dx$ equals the difference of flux entering and leaving the domain.

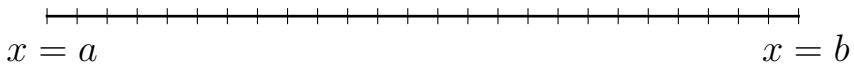

Figure 6.1: One-dimensional single grid on a domain $x \in [a, b]$.

In case of an overlapping domain as shown in Figure 6.2 for $\frac{\partial f}{\partial q} > 0$, the flux enters the computational domain at $x = a_L$ and exits at $x = b_L$ and $x = b_R$. At $x = a_R$, the flux is duplicated from the left sub-domain to the right. We introduce the integral quantities

$$U_a = \int_{a_L}^{a_R} u \; dx, \qquad U_b = \int_{a_R}^{b_L} u \; dx, \qquad V = \int_{a_R}^{b_R} v \; dx, \tag{6.5}$$

where $u(x, t)$ and $v(x, t)$ denote the solution of (6.3) on the left and the right sub-domain respectively. Let us denote the flux on the left and the right sub-domain by $f_u(x, t) = f(u(x, t))$ and $f_v(x, t) = f(v(x, t))$ respectively. The time rate of change of the integral quantities in (6.5) is given by

$$\frac{dU_a}{dt} = f_u(a_L, t) - f_u(a_R, t), \qquad \frac{dU_b}{dt} = f_u(a_R, t) - f_u(b_L, t), \qquad \frac{dV}{dt} = f_v(a_R, t) - f_v(b_R, t).$$

If we consider a quantity $S_2 = \eta_1 U_a + \eta_2 U_b + \eta_3 V$ where $\eta_{1,2,3}$ are non-negative constants such that $\eta_1 = \eta_2 + \eta_3$ then

$$\frac{dS_2}{dt} = \eta_1 f_u(a_L, t) - \eta_2 f_u(b_L, t) - \eta_3 f_v(b_R, t), \tag{6.6}$$

using $f_u(a_R, t) = f_v(a_R, t)$ since the flux is duplicated at a_R. Eq. (6.6) shows that the quantity S_2 is conserved except for the fluxes at the physical boundaries of the domain in Figure 6.1.

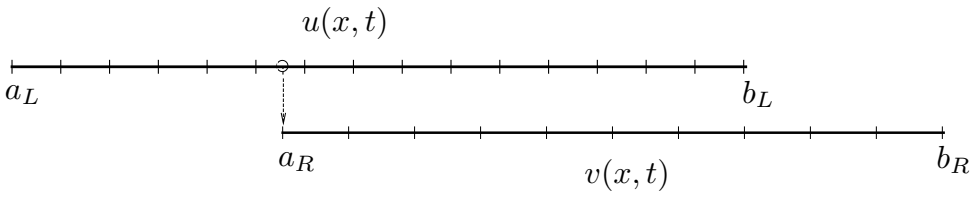

Figure 6.2: Overlapping grid setup with the left domain $x \in [a_L, b_L]$ and the right domain $x \in [a_R, b_R]$. Downward pointing arrow denotes the interpolation.

It is important to highlight that, in practice, the overlapping grid configuration shown in Figure 6.2 is a substitute for the physical domain shown in Figure 6.1 with $a = a_L$ and $b = b_R$. The conservation statement for the physical domain is given by Eq. (6.4), and for the overlapping grid conservation statement (6.6) to mimic (6.4) we must use $\eta_1 = \eta_3 = 1$ and $\eta_2 = 0$, which implies $S_2 = U_a + V$.

The conservation statement for the overlapping domain, Eq. (6.6), does not equal Eq. (6.4) because of an extra physical boundary at $x = b_L$ on the left domain, see Figure 6.2, which loses or gains flux. If, instead, $x = b_L$ on the left domain was an internal boundary, like $x = a_R$ on the right domain where numerical boundary condition (via interpolation) is imposed, the two conservation statements would match as we show below. When the interpolated data is imposed on both the domains, i.e., at $x = a_R$ on the right domain and at $x = b_L$ on the left domain in Figure 6.1, the flux enters the computational domain at $x = a_L$ and leaves at $x = b_R$ for $\frac{\partial f}{\partial q} > 0$. If we split the the integral V in (6.5) as

$$V_a = \int_{a_R}^{b_L} v \; dx, \qquad V_b = \int_{b_L}^{b_R} v \; dx,$$

then

$$\frac{dV_a}{dt} = f_v(a_R, t) - f_v(b_L, t), \qquad \frac{dV_b}{dt} = f_v(b_L, t) - f_v(b_R, t).$$

For a quantity $S = U_a + \alpha U_b + \beta V_a + V_b$ such that $\alpha + \beta = 1$,

$$\frac{dS}{dt} = f_u(a_L, t) - f_v(b_R, t), \tag{6.7}$$

using $f_u(a_R, t) = f_v(a_R, t)$ and $f_u(b_L, t) = f_v(b_L, t)$ since the flux is duplicated at $x = a_R$ and $x = b_L$. Eq. (6.7) is equivalent to the conservation statement for the single domain, Eq. (6.4). In the SAT method, discussed here, the interpolated data is applied only to the downwind domain based on the characteristic direction as shown in Figure 6.2, whereas in references that use the injection method, for e.g., Berger (1987, Figure 4.1) and Chesshire & Henshaw (1994, Figure 5), it is applied to both the domains.

6.1 Boundary Overlap

In this section, we derive the values of the free parameters in the method (5.1)–(5.2) that make it conservative for a boundary overlap configuration.

6.1.1 Second-Order Method

In Theorem 5.1, we provided the values of τ_L, τ_R, C_L, Υ_L and β_R in the method (5.1)–(5.2) that made it time-stable. The parameter values were expressed in terms of $q > 0$ and $0 \leq \epsilon < 1$. The following theorem derives a single fixed value of q and ϵ that makes the method time-stable and conservative.

Theorem 6.1 *The method (5.1)–(5.2) for the overlapping grid configuration shown in Figure 5.1 with the* $1-2-1$ *SBP first derivative approximation, linear Lagrangian interpolation given by Eq. (5.10) and the dissipative operator given by Eq. (5.8) is time-stable and conservative if* $q = \frac{1}{2}$ *and* $\epsilon = 0$ *in (5.12).*

Proof. A discrete approximation of (6.5) can be written as

$$U_a \approx \sum_{i=0}^{m} w_i^a u_i h_L, \qquad U_b \approx \sum_{i=0}^{m} w_i^b u_i h_L, \qquad V \approx \sum_{i=0}^{n} w_i^v v_i h_R, \tag{6.8}$$

where $w_i^{a,b,v}$ denotes the quadrature weights that are determined by assuming

$$u(x,t) \approx \sum_{i=0}^{m} \phi_i^L(x) u_i(t), \qquad v(x,t) \approx \sum_{i=0}^{n} \phi_i^R(x) v_i(t), \tag{6.9}$$

in (6.5) and matching the coefficients with (6.8). h_L and h_R denote the grid spacing on the left and the right sub-domain, respectively, and $\phi_i^{L,R}(x)$ denotes the piecewise linear interpolants

$$\phi_i^{L,R}(x) = \begin{cases} \frac{x - x_{i-1}}{x_i - x_{i-1}}, & x \in [x_{i-1},\ x_i], \\ \frac{x_{i+1} - x}{x_{i+1} - x_i}, & x \in [x_i,\ x_{i+1}], \\ 0, & \text{otherwise.} \end{cases} \tag{6.10}$$

The quadrature weights, so obtained, are

$$w_0^a = \frac{1}{2}, \qquad w_1^a = \cdots = w_{m-2}^a = 1, \qquad w_{m-1}^a = 1 - \frac{\alpha_L^2}{2}, \qquad w_m^a = \frac{(1-\alpha_L)^2}{2},$$

$$w_0^b = \cdots = w_{m-2}^b = 0, \qquad w_{m-1}^b = \frac{\alpha_L^2}{2}, \qquad w_m^b = \alpha_L - \frac{\alpha_L^2}{2},$$

$$w_0^v = \frac{1}{2}, \qquad w_1^v = \cdots = w_{n-1}^v = 1, \qquad w_n^v = \frac{1}{2}.$$

The semidiscrete approximation to (6.3) with a homogeneous BC can be written as $\mathbf{q}_t = M\mathbf{f}$, where $\mathbf{q} = \begin{bmatrix} \mathbf{u} & \mathbf{v} \end{bmatrix}^T$, $\mathbf{f} = \begin{bmatrix} \mathbf{f}_u & \mathbf{f}_v \end{bmatrix}^T$ and M is the system matrix of the method (5.1)-(5.2). For $\eta_1 = \eta_3 = 1$ and $\eta_2 = 0$ in (6.6), the discrete approximation of dS_2/dt, where $S_2 = U_a + V$, can be written as

$$\frac{dS_2}{dt} \approx \sum_{i=0}^{m} w_i^a \left(M\mathbf{f}\right)_i h_L + \sum_{i=0}^{n} w_i^v \left(M\mathbf{f}\right)_{i+m+1} h_R. \tag{6.11}$$

Substituting the quadrature weights and the values of τ_L, β_R, τ_R, C_L and Υ_L given by (5.12) in (6.11) requires $k = 0$, $q = \frac{1}{2}$ and $\epsilon = 0$ to eliminate the interface terms. This completes the proof. □

Using the derived values of the parameters, a modified derivative operator can be defined as $\widetilde{P}_L^{-1}\widetilde{Q}_L = P_L^{-1}Q_L - \Upsilon_L$, where

$$\widetilde{P}_L = H_L = h_L \begin{bmatrix} \frac{1}{2} & & & & & \\ & 1 & & & & \\ & & \ddots & & & \\ & & & 1 & & \\ & & & & 1 - \frac{\alpha_L^2}{2} & \\ & & & & & \frac{(1-\alpha_L)^2}{2} \end{bmatrix}, \qquad \widetilde{Q}_L = \begin{bmatrix} -\frac{1}{2} & \frac{1}{2} & 0 & .. & .. & 0 \\ -\frac{1}{2} & 0 & \frac{1}{2} & .. & .. & 0 \\ . & .. & .. & .. & .. & . \\ . & .. & -\frac{1}{2} & 0 & \frac{1}{2} & \\ 0 & .. & .. & -\frac{1}{2} & \frac{\alpha_L^2}{2} & \frac{1}{2} - \frac{\alpha_L^2}{2} \\ 0 & .. & .. & & -\frac{(1-\alpha_L)^2}{2} & \frac{(1-\alpha_L)^2}{2} \end{bmatrix}. \tag{6.12}$$

For $\alpha_L = 0$, i.e. a multiblock grid, the above operators become the traditional SBP P and Q operators for the first derivative approximation $D = P^{-1}Q$ of second-order accuracy. For $\alpha_L = 1$, they again are the SBP operators where the last grid point is ignored.

An important observation from the above result is that the norm matrix H, used for the SAT implementation and for proving time-stability in Section 5.1.1, is a quadrature for discrete approximation of integral S_2 in order for the method to be conservative. In the above result, the norm matrix

$$H = \begin{bmatrix} \widetilde{P}_L & \\ & P_R \end{bmatrix},$$

is a quadrature for an approximation of the integral $S_2 = U_a + V$. See Hicken & Zingg (2013) for the implications of H being a quadrature on SBP-based discretizations.

6.1.2 Third-Order Method

In theorem 5.3, we provided the values of the parameters that make the method (5.1)–(5.2) time-stable for a boundary overlap configuration with the $2-4-2$ first derivative approximation and cubic Lagrange interpolation. In this section, we discuss the conservation properties of the method.

Lemma 6.1 *The method (5.1)–(5.2) for the overlapping grid configuration shown in Figure 5.4 with the* $2-4-2$ *SBP first derivative approximation, cubic Lagrangian interpolation given by Eqs. (5.40)-(5.43) and the dissipative operator given by Eq. (5.44), is conservative if*

$$\tau_L \geq \frac{1}{2}, \qquad c_0^L = ... = c_{m-4}^L = 1, \qquad \lambda = \beta_R = \tau_R = 1,$$

$$r_{16} = \frac{-3c_{m-3}^L + c_m^L(3+34r_{44})}{98c_{m-3}^L}, \qquad r_{25} = -\frac{4c_{m-2}^L - c_m^L(4-51r_{44})}{43c_{m-2}^L}, \qquad r_{34} = -\frac{40-49c_{m-3}^L + c_m^L(9+102r_{44})}{708c_{m-1}^L},$$

$$r_{11} = \frac{4(c_{m-3}^L-1)}{49c_{m-3}^L}, \quad r_{12} = -\frac{32(c_{m-3}^L-\lambda)}{49c_{m-3}^L}, \quad r_{13} = -6r_{11}-3r_{12}-r_{16}, \quad r_{14} = 8r_{11}+3r_{12}+3r_{16},$$

$$r_{15} = -3r_{11}-r_{12}-3r_{16}, \quad r_{21} = \frac{4(c_{m-2}^L-1)}{43c_{m-2}^L}, \quad r_{22} = -3r_{21}-r_{25}, \quad r_{23} = 3(r_{21}+r_{25}), \quad r_{24} = -r_{21}-3r_{25},$$

$$r_{31} = -r_{34}, \qquad r_{32} = 3r_{34}, \qquad r_{33} = -3r_{34}, \qquad r_{41} = -r_{44}, \qquad r_{42} = 3r_{44}, \qquad r_{43} = -3r_{44},$$

where

$$c_{m-2}^L = \frac{148-98c_{m-3}^L+17c_m^L-24\alpha_L^2}{43}, \qquad c_{m-1}^L = \frac{-28+49c_{m-3}^L-34c_m^L+24\alpha_L(-2+\alpha_L)}{59},$$

$$r_{44} = \frac{-3(1+c_m^L)+2\alpha_L(2+\alpha_L(3-2\alpha_L))}{34c_m^L},$$

for

$$\frac{2371+946\alpha_L-768\alpha_L^2}{2276} < c_{m-3}^L < \frac{13367-374\alpha_L-2016\alpha_L^2}{8572}, \qquad c_m^L = \frac{2276c_{m-3}^L+768\alpha_L^2-946\alpha_L-2371}{4156}.$$

Proof. For $\eta_1 = \eta_3 = 1$ *and* $\eta_2 = 0$ *in (6.6), the discrete approximation of* dS_2/dt *is given by (6.11) where, assuming the diagonal norm matrix* $H = \text{diag}(C_L P_L,\, \beta_R P_R)$ *as quadrature with* C_L *given by (5.48), the quadrature weights are,*

$$\begin{gathered} w_0^a = \tfrac{17}{48}\lambda, \quad w_1^a = \tfrac{59}{48}\lambda, \quad w_2^a = \tfrac{43}{48}\lambda, \quad w_3^a = \tfrac{49}{48}\lambda, \quad w_4^a = \cdots = w_{m-4}^a = \lambda, \\ w_{m-3}^a = \tfrac{49}{48}c_{m-3}^L, \quad w_{m-2}^a = \tfrac{43}{48}c_{m-2}^L, \quad w_{m-1}^a = \tfrac{59}{48}c_{m-1}^L, \quad w_m^a = \tfrac{17}{48}c_m^L, \end{gathered} \tag{6.13}$$

and, similarly, for the right subdomain,

$$w_0^v = \tfrac{17}{48}\beta_R, \quad w_1^v = \tfrac{59}{48}\beta_R, \quad w_2^v = \tfrac{43}{48}\beta_R, \quad w_3^v = \tfrac{49}{48}\beta_R, \quad w_4^v = \cdots = w_{m-4}^v = \beta_R,$$
$$w_{n-3}^v = \tfrac{49}{48}\beta_R, \quad w_{n-2}^v = \tfrac{43}{48}\beta_R, \quad w_{n-1}^v = \tfrac{59}{48}\beta_R, \quad w_n^v = \tfrac{17}{48}\beta_R. \tag{6.14}$$

For (6.14) to provide a quadrature for calculating V (see (6.5)), β_R must equal 1 and (6.13) provides a quadrature for U_a if $\lambda = 1$ and $\frac{49}{48}c_{m-3}^L + \frac{43}{48}c_{m-2}^L + \frac{59}{48}c_{m-1}^L + \frac{17}{48}c_m^L = \frac{5}{2} - \alpha_L$. Substituting the quadrature weights and the values of τ_L, C_L and Υ_L given by (5.48)-(5.50) in the system matrix M of (6.11) with

$$r_{16} = \frac{-3c_{m-3}^L + c_m^L(3 + 34r_{44})}{98c_{m-3}^L}, \qquad r_{25} = -\frac{4c_{m-2}^L - c_m^L(4 - 51r_{44})}{43c_{m-2}^L},$$
$$r_{34} = -\frac{40 - 49c_{m-3}^L + c_m^L(9 + 102r_{44})}{118c_{m-1}^L},$$

requires

$$\tau_R = 1,$$
$$\frac{1}{96}(-136 + 98c_{m-3}^L + 43c_{m-2}^L - c_m^L(5 - 136r_{44})) + \tau_R l_1 = 0,$$
$$\frac{1}{96}(-49c_{m-3}^L + 59c_{m-1}^L - 2(4 + c_m^L(1 + 204r_{44}))) + \tau_R l_2 = 0,$$
$$\frac{1}{96}(88 - 98c_{m-3}^L - 43c_{m-2}^L + c_m^L(53 + 408r_{44})) + \tau_R l_3 = 0,$$
$$\frac{1}{96}(49c_{m-3}^L - 59c_{m-1}^L - 2(20 + c_m^L(23 + 68r_{44})) + \tau_R l_4 = 0,$$

with $\lambda = \beta_R = 1$ to cancel out the interface terms. Solving the above equations with interpolation coefficients for cubic Lagrangian interpolation, Eq. (5.43), yields

$$c_{m-2}^L = \frac{148 - 98c_{m-3}^L + 17c_m^L - 24\alpha_L^2}{43}, \qquad c_{m-1}^L = \frac{-28 + 49c_{m-3}^L - 34c_m^L + 24\alpha_L(-2 + \alpha_L)}{59},$$
$$r_{44} = \frac{-3(1 + c_m^L) + 2\alpha_L(2 + \alpha_L(3 - 2\alpha_L))}{34c_m^L}.$$

Imposing the constraint of c_{j+1}^L, c_{j+2}^L, c_{j+3}^L, $c_{j+4}^L > 0$ for $\alpha_L \in [0, 1]$ requires,

$$\frac{2371 + 946\alpha_L - 768\alpha_L^2}{2276} < c_{m-3}^L < \frac{13367 - 374\alpha_L - 2016\alpha_L^2}{8572}, \qquad c_m^L = \frac{2276c_{m-3}^L + 768\alpha_L^2 - 946\alpha_L - 2371}{4156}.$$

This completes the proof. □

6.2 Interior Overlap

In this section, we analyze the conservation properties of the method (5.1)–(5.2) for overset configurations where the donor grid points for interpolation lie in the interior of the domain. We stated in the previous section that the norm matrix H provides a quadrature for approximating the integral S_2 which, for the boundary overlap case, was taken to equal $U_a + V$ while ignoring U_b. It was possible to ignore U_b because the quadrature weights for approximating U_a, w_i^a for $0 \leq i \leq m$, were sufficient to provide a positive-definite $H_L = C_L P_L$. This is not the case in an interior overlap configuration where ignoring U_b results in H_L having zero diagonal entries. It amounts to blanking out the overlapping grid points on the left subdomain, thus, reducing the configurations in Figures 5.3 and 5.5 to boundary overlap configurations of Figures 5.1 and 5.4 respectively. In practice, however, overset grids with interior overlap are commonly used and, so, they must be independently analyzed.

As discussed, we cannot ignore U_b for the interior overlap configurations therefore the quantity conserved in this case would be $S_2 = \eta_1 U_a + \eta_2 U_b + \eta_3 V$ such that $\eta_1 = \eta_2 + \eta_3$, see Eq. (6.6), and, therefore, the parameter values will depend on the choice of $\eta_{1,2,3}$.

6.2.1 Second-Order Method

In theorem 5.2, we provided the range of parameter values that make the method (5.1)–(5.2) time-stable. The following theorem provides a fixed value of the parameters required to make it time-stable and conservative.

Theorem 6.2 *The method (5.1)–(5.2) for the overlapping grid configuration shown in Figure 5.3 with the* $1-2-1$ *SBP first derivative approximation, linear Lagrangian interpolation given by Eq. (5.28) and the dissipative operator given by Eq. (5.8) is time-stable and conservative for* $0 \leq \alpha_L \leq 1$ *if*

$$p = \frac{1}{2}(1-\eta_2)\alpha_L, \qquad y = \frac{1}{2}(1-\eta_2)(1-\alpha_L), \qquad z = \eta_2, \qquad q = \frac{1}{2}, \qquad \beta_R = \eta_3 \tag{6.15}$$

in (5.30).

Proof. Following Eq. (6.11), the discrete approximation of dS_2/dt for $S_2 = \eta_1 U_a + \eta_2 U_b + \eta_3 V$ can be written as

$$\frac{dS_2}{dt} \approx \sum_{i=0}^{m} w_i^a \left(M\mathbf{f}\right)_i h_L + \sum_{i=0}^{m} w_i^b \left(M\mathbf{f}\right)_i h_L + \sum_{i=0}^{n} w_i^v \left(M\mathbf{f}\right)_{i+m+1} h_R. \tag{6.16}$$

where, assuming the diagonal norm matrix $H = \mathrm{diag}(C_L P_L,\, \beta_R P_R)$ as quadrature with C_L given by (5.30),

the quadrature weights are assumed as

$$w_0^a = \tfrac{1}{2}, \qquad w_1^a = \cdots = w_j^a = 1, \qquad w_{j+1}^a = k_1 c_{j+1}^L, \qquad w_{j+2}^a = k_2 c_{j+2}^L, \qquad w_{j+3}^a = \cdots = w_m^a = 0, \tag{6.17}$$

$$w_0^b = \cdots = w_j^b = 0, \quad w_{j+1}^b = (1-k_1)c_{j+1}^L, \quad w_{j+2}^b = (1-k_2)c_{j+2}^L, \quad w_{j+3}^b = \cdots = w_{m-1}^b = z, \quad w_m^b = \frac{z}{2}, \tag{6.18}$$

where $k_1,\, k_2 > 0$. The weights are such that $C_L P_L = h_L \,\mathrm{diag}(w_0^a + w_0^b, \cdots, w_m^a + w_m^b)$. Similarly for the right subdomain,

$$w_0^v = \frac{\beta_R}{2}, \qquad w_1^v = \cdots = w_{n-1}^v = \beta_R, \qquad w_n^v = \frac{\beta_R}{2}. \tag{6.19}$$

(6.19) provides a quadrature for calculating $\eta_3 V$, see (6.5), if $\beta_R = \eta_3$, and (6.17) and (6.18) provide a quadrature for $\eta_1 U_a$ and $\eta_2 U_b$, respectively, if $z = \eta_2$, $\eta_1 = 1$ and $c_{j+1}^L + c_{j+2}^L = \left(\frac{3}{2} - \alpha_L\right) + z\left(\frac{1}{2} + \alpha_L\right)$. h_L denotes the grid spacing on the left domain.

We substitute the quadrature weights (6.17)–(6.19) in (6.16) with system matrix M formed from the $1-2-1$ SBP first derivative approximation, linear Lagrange interpolation and a dissipative operator given by Eq. (5.8), as discussed in Section (5.1.2). Substituting $\Gamma_L = \mathrm{diag}\left(0, \ldots.., 0, \frac{1-c_{j+1}^L}{2c_{j+1}^L}, \frac{c_{j+2}^L - c_m^L}{2c_{j+2}^L}, 0, \ldots.., 0\right)$ and change of variables (5.34) requires

$$y = \frac{1}{2} + p - \frac{\eta_2}{2} - (1-\eta_2)\alpha_L, \qquad q = \frac{1}{2}, \tag{6.20}$$

to eliminate the interface terms, thus conserving $S_2 = \eta_1 U_a + \eta_2 U_b + \eta_3 V$ for $\eta_1 = \eta_2 + \eta_3 = 1$. Using (6.20) in the matrix K, given by (5.35), with $p = \frac{1}{2}(1-\eta_2)\alpha_L$ makes it negative semidefinite establishing time-stability. This completes the proof. $\square$

The modified derivative operator, $\widetilde{P}_L^{-1}\widetilde{Q}_L = P_L^{-1}Q_L - \Upsilon_L$, in this case is given by

$$\widetilde{P}_L = H_L = h_L \,\mathrm{diag}\left(\frac{1}{2}, 1, \cdots, 1, \widetilde{p}_{j+1}, \widetilde{p}_{j+2}, \eta_2, \cdots, \eta_2, \frac{\eta_2}{2}\right), \tag{6.21}$$

where $\widetilde{p}^L_{j+1} = 1 - \frac{1}{2}(1-\eta_2)\alpha_L$ and $\widetilde{p}^L_{j+2} = \eta_2 + \frac{1}{2}(1-\eta_2)(1-\alpha_L)$, and $\widetilde{Q}_L$ equals

$$\begin{bmatrix}
-\frac{1}{2} & \frac{1}{2} & & & & & & & & & \\
-\frac{1}{2} & 0 & \frac{1}{2} & & & & & & & & \\
 & \ddots & \ddots & & \ddots & & & & & & \\
 & -\frac{1}{2} & 0 & & \frac{1}{2} & & & & & & \\
 & & -\frac{1}{2+(-1+\eta_2)\alpha_L} & -1+\frac{2}{2+(-1+\eta_2)\alpha_L} & 1-\frac{1}{2+(-1+\eta_2)\alpha_L} & & & & & & \\
 & & & -1+\frac{\eta_2}{1+\eta_2+(-1+\eta_2)\alpha_L} & 1-\frac{2\eta_2}{1+\eta_2+(-1+\eta_2)\alpha_L} & \frac{\eta_2}{1+\eta_2+(-1+\eta_2)\alpha_L} & & & & & \\
 & & & & -\frac{1}{2} & 0 & \frac{1}{2} & & & & \\
 & & & & & \ddots & \ddots & \ddots & & & \\
 & & & & & & -\frac{1}{2} & 0 & \frac{1}{2} & & \\
 & & & & & & & -\frac{1}{2} & \frac{1}{2} & &
\end{bmatrix}.$$

If η_2 is assumed to be zero, i.e., if U_b is ignored in S_2, the entries corresponding to the overlapping grid points of the left domain become zero in $\widetilde{P}_L$, and the norm matrix H_L ceases to be positive-definite. Hence U_b cannot be ignored for an interior overlap configuration. One can discard the trailing zero entries of H_L to keep it positive-definite by blanking out the grid points corresponding to the zero entries which results in a boundary overlap configuration. Note that (6.15) is not a unique solution, additional solutions could be obtained by considering $p \neq \frac{1}{2}(1-\eta_2)\alpha_L$.

6.2.2 Third-Order Method

In theorem 5.4, we provided the values of the parameters that make the method (5.1)–(5.2) time-stable for an interior overlap configuration with the $2-4-2$ first derivative approximation and cubic Lagrange interpolation. In this section, we discuss the conservation properties of the method. Theorem 5.4 applied an accuracy of $2-3-3-2$ for the first-derivative approximation at the donor grid points, see Eq. (5.63). In the following results, we assume an accuracy of $2-2-2-2$ to allow for extra free parameters to satisfy both the stability and conservation constraints.

Lemma 6.2 *The method (5.1)-(5.2) for the overlapping grid configuration shown in Figure 5.4 with the* $2-4-2$ *SBP first derivative approximation, cubic Lagrangian interpolation given by Eqs. (5.54)-(5.57) and the dissipative operator given by Eq. (5.58) is conservative if*

$$\tau_L \geq \frac{\eta_1}{2}, \qquad \beta_R = \tau_R = \eta_1 - \eta_2,$$

$$r_{11} = \frac{c^L_{j+1} - \eta_1}{12c^L_{j+1}}, \quad r_{12} = -\frac{2(c^L_{j+1} - \eta_1)}{3c^L_{j+1}}, \quad r_{13} = -6r_{11} - 3r_{12}, \quad r_{14} = 8r_{11} + 3r_{12}, \quad r_{15} = -3r_{11} - r_{12},$$

$$r_{21} = \frac{c^L_{j+2} - \eta_1}{12c^L_{j+2}}, \quad r_{25} = \frac{-24c^L_{j+1} + 5c^L_{j+2} + 19\eta_1}{12c^L_{j+2}}, \quad r_{22} = -3r_{21} - r_{25}, \quad r_{23} = 3(r_{21} + r_{25}), \tag{6.22}$$

$$r_{24} = -r_{21} - 3r_{25}, \qquad r_{31} = \frac{-6c^L_{j+1} + c^L_{j+3} + 5\eta_1}{12c^L_{j+3}}, \qquad r_{35} = \frac{-c^L_{j+3} + \eta_2}{12c^L_{j+3}},$$

$$r_{32} = -3r_{31} - r_{35}, \qquad r_{33} = 3(r_{31} + r_{35}), \qquad r_{34} = -r_{31} - 3r_{35}, \quad r_{44} = \frac{2(c^L_{j+4} - \eta_2)}{3c^L_{j+4}},$$

$$r_{45} = \frac{-c^L_{j+4} + \eta_2}{12c^L_{j+4}}, \quad r_{41} = -r_{44} - 3r_{45}, \quad r_{42} = 3r_{44} + 8r_{45}, \quad r_{43} = -3r_{44} - 6r_{45},$$

$$c^L_0 = \text{.....} = c^L_j = \eta_1, \qquad c^L_{j+1} = \eta_1 - \frac{\tau_R}{3} l_1, \qquad c^L_{j+2} = c^L_{j+4} + \frac{7}{12}(\eta_1 - \eta_2) + \frac{\tau_R}{12}(-10l_1 + 6l_3),$$

$$c^L_{j+3} = -2c^L_{j+4} + \frac{1}{12}(23\eta_1 + 13\eta_2 - 2\tau_R(11l_1 + 12l_2 + 9l_3)), \qquad c^L_{j+5} = \text{.....} = c^L_m = \eta_2,$$

where l_i for $1 \le i \le 4$ is given by Eq. (5.57) and

$$0 < c^L_{j+4} < \frac{1}{72}(15\eta_1 + 93\eta_2 - 2\tau_R\alpha_L(17 + (-9 + \alpha_L)\alpha_L),$$

for $0 < \eta_2 < \eta_1 < 37\eta_2$.

Proof. The discrete approximation of dS_2/dt for $S_2 = \eta_1 U_a + \eta_2 U_b + \eta_3 V$ is given by (6.16), where using the diagonal norm matrix $H = \text{diag}(C_L P_L, \beta_R P_R)$ as quadrature with C_L given by (5.60), the quadrature weights are assumed as

$$w^a_0 = \tfrac{17}{48}\lambda, \quad w^a_1 = \tfrac{59}{48}\lambda, \quad w^a_2 = \tfrac{43}{48}\lambda, \quad w^a_3 = \tfrac{49}{48}\lambda, \quad w^a_4 = \cdots = w^a_j = \lambda,$$

$$w^a_{j+1} = k_1 c^L_{j+1}, \quad w^a_{j+2} = k_2 c^L_{j+2}, \quad w^a_{j+3} = k_3 c^L_{j+3}, \quad w^a_{j+4} = k_4 c^L_{j+4}, \qquad w^a_{j+5} = \cdots = w^a_m = 0, \tag{6.23}$$

$$w^b_0 = \cdots = w^b_j = 0, \quad w^b_{j+1} = (1 - k_1)c^L_{j+1}, \quad w^b_{j+2} = (1 - k_2)c^L_{j+2}, \quad w^b_{j+3} = (1 - k_3)c^L_{j+3},$$

$$w^b_{j+4} = (1 - k_4)c^L_{j+4}, \quad w^a_{j+5} = \cdots = w^a_{m-4} = \mu, \tag{6.24}$$

$$w^b_{m-3} = \tfrac{49}{48}\mu, \quad w^b_{m-2} = \tfrac{43}{48}\mu, \quad w^b_{m-1} = \tfrac{59}{48}\mu, \quad w^b_m = \tfrac{17}{48}\mu,$$

for k_1, k_2, k_3, $k_4 > 0$. The weights are such that $C_L P_L = h_L \,\text{diag}(w^a_0 + w^b_0, \cdots, w^a_m + w^b_m)$. Similarly for the right subdomain,

$$w_0^v = \tfrac{17}{48}\beta_R, \quad w_1^v = \tfrac{59}{48}\beta_R, \quad w_2^v = \tfrac{43}{48}\beta_R, \quad w_3^v = \tfrac{49}{48}\beta_R, \quad w_4^v = \cdots = w_{m-4}^v = \beta_R,$$

$$w_{n-3}^v = \tfrac{49}{48}\beta_R, \quad w_{n-2}^v = \tfrac{43}{48}\beta_R, \quad w_{n-1}^v = \tfrac{59}{48}\beta_R, \quad w_n^v = \tfrac{17}{48}\beta_R. \tag{6.25}$$

(6.25) provides a quadrature for calculating $\eta_3 V$, see (6.5), if $\beta_R = \eta_3$, and (6.23) and (6.24) provide a quadrature for $\eta_1 U_a$ and $\eta_2 U_b$, respectively, if $\lambda = \eta_1$, $\mu = \eta_2$, and $c_{j+1}^L + c_{j+2}^L + c_{j+3}^L + c_{j+4}^L = \left(\frac{5}{2} - \alpha_L\right)\lambda + \left(\frac{3}{2} + \alpha_L\right)\mu$.

We substitute the quadrature weights (6.23)–(6.25) in (6.16), where the system matrix M is formed using the $2-4-2$ SBP first derivative approximation, the dissipative operator given by Eq. (5.58) and the interpolation vector (5.55). An accuracy of $2-2-2-2$ for the first-derivative approximation $\tilde{D}_L \mathbf{u} = (P_L^{-1} Q_L - \Upsilon_L)\mathbf{u}$ at the donor grid points is imposed which required

$$\begin{aligned}
&r_{13} = -6r_{11} - 3r_{12}, \qquad r_{14} = 8r_{11} + 3r_{12}, \qquad r_{15} = -3r_{11} - r_{12},\\
&r_{22} = -3r_{21} - r_{25}, \qquad r_{23} = 3(r_{21} + r_{25}), \qquad r_{24} = -r_{21} - 3r_{25},\\
&r_{32} = -3r_{31} - r_{35}, \qquad r_{33} = 3(r_{31} + r_{35}), \qquad r_{34} = -r_{31} - 3r_{35},\\
&r_{41} = -r_{44} - 3r_{45}, \qquad r_{42} = 3r_{44} + 8r_{45}, \qquad r_{43} = -3r_{44} - 6r_{45},
\end{aligned} \tag{6.26}$$

and we choose

$$r_{25} = \frac{-24c_{j+1}^L + 5c_{j+2}^L + 19\lambda}{12c_{j+2}^L}, \qquad r_{31} = \frac{-6c_{j+1}^L + c_{j+3}^L + 5\lambda}{12c_{j+3}^L},$$

to simplify the stability analysis, discussed in the next theorem. Further, substituting (5.60)–(5.62) in M with $\beta_R = \eta_3 = \eta_1 - \eta_2 = \lambda - \mu$ requires

$$\begin{aligned}
&\tau_R = \lambda - \mu,\\
&3(c_{j+1}^L - \lambda) + \tau_R l_1 = 0,\\
&\frac{1}{6}(-39c_{j+1}^L + 9c_{j+2}^L + 3c_{j+3}^L - 3c_{j+4}^L + 28\lambda + 2\mu) + \tau_R l_2 = 0,\\
&5c_{j+1}^L - 2c_{j+2}^L + 2c_{j+4}^L - \frac{23}{6}\lambda - \frac{7}{6}\mu + \tau_R l_3 = 0,\\
&\frac{1}{6}(-9c_{j+1}^L + 3c_{j+2}^L - 3c_{j+3}^L - 9c_{j+4}^L + 7\lambda + 11\mu) + \tau_R l_4 = 0
\end{aligned} \tag{6.27}$$

to eliminate the interface terms. Solving for c_{j+1}^L, c_{j+2}^L, c_{j+3}^L and c_{j+4}^L from (6.27) we get

$$c_{j+1}^L = \lambda - \frac{\tau_R}{3} l_1, \qquad c_{j+2}^L = c_{j+4}^L + \frac{7}{12}(\lambda - \mu) + \frac{\tau_R}{12}(-10l_1 + 6l_3),$$

$$c_{j+3}^L = -2c_{j+4}^L + \frac{1}{12}(23\lambda + 13\mu - 2\tau_R(11l_1 + 12l_2 + 9l_3)). \tag{6.28}$$

Substituting the interpolation coefficients for cubic Lagrangian interpolation from (5.57) provides the admissible values of c_{j+1}^L, c_{j+2}^L and c_{j+3}^L in terms of c_{j+4}^L. Imposing the constraint of λ, μ, β_R, c_{j+1}^L, c_{j+2}^L, c_{j+3}^L, $c_{j+4}^L > 0$ for $\alpha_L \in [0, 1]$ requires

$$0 < c_{j+4}^L < \frac{1}{72}(15\lambda + 93\mu - 2\tau_R\alpha_L(17 + (-9 + \alpha_L)\alpha_L),$$

for $0 < \mu < \lambda < 37\mu$. Substituting $\lambda = \eta_1$ and $\mu = \eta_2$ completes the proof. □

Note that the parameter values provided in this section for the third-order scheme ensure conservation but not time-stability. The parameter values that ensure both conservation and time-stability were found for certain overlapping configurations, for example when the receiver point is at the center of a donor cell, but no general solutions applicable to all overlapping scenarios, such as the one provided for the second-order scheme, was found.

Chapter 7

Application to the Compressible Navier-Stokes Equations

In this chapter, we discuss the extension of the overset SAT method, analyzed in Chapters 4, 5 and 6, to solve the viscous fluid flow problems governed by the Navier-Stokes equations. Our focus in the previous three chapters was on hyperbolic equations but, since, the unsteady compressible Navier-Stokes equations are of mixed hyperbolic-parabolic (or incompletely parabolic) nature we first discuss the interface treatment for the simplest parabolic equation, the heat equation. Section 7.1 proposes a SBP-SAT based method to solve the heat equation on overlapping grids that is shown to be time-stable for the second-order accurate operators. The approach is general in that it allows proving stability for higher-order versions but we have had limited success in extending this approach of proof of stability to incompletely parabolic problems. Therefore for the three-dimensional turbulent flow simulation discussed in Section 7.3, we use viscous interface treatment analogous to those derived by Nordström *et al.* (2009) for multiblock grids with inviscid treatment discussed in Chapter 4. The detailed formulation is provided in Section 7.2.

7.1 The Heat Equation

Consider the IBVP,

$$\frac{\partial u}{\partial t} = \frac{\partial^2 u}{\partial x^2}, \qquad a \leq x \leq b,\ t \geq 0, \tag{7.1}$$

with Dirichlet boundary conditions and initial condition given by,

$$u(a,t) = g_1(t), \qquad u(b,t) = g_2(t),$$

$$u(x,0) = f(x), \tag{7.2}$$

on an overlapping domain as shown in Figure 7.1. The left and the right domain contain equally spaced $m+1$ and $n+1$ grid points respectively. Let the grid functions on the left and the right domain be denoted by $\mathbf{u}(t) = [u_0(t), \ldots, u_m(t)]^T$ and $\mathbf{v}(t) = [v_0(t), \ldots, v_n(t)]^T$ respectively.

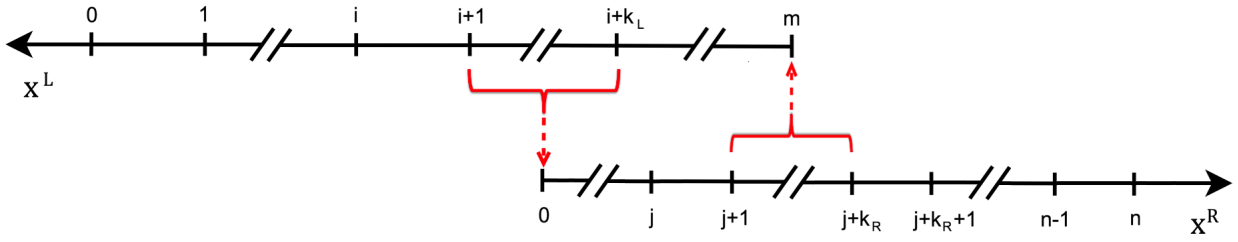

Figure 7.1: Schematic diagram of overlapping grids on which Eq. (7.1) is solved. The red arrow denotes the interpolation.

For the grid configuration shown in Figure 7.1, the interface treatment for a parabolic problem differs from the one for a hyperbolic problem in that it requires a bi-directional coupling. We saw for a hyperbolic problem in sections 4.1.2 and 5.1.1 that the interpolation was needed only for the right grid to advance the solution. The left domain was decoupled in the sense that the solution on it advanced independent of the right domain. This is consistent with the character of the hyperbolic equations, where information propagates along the characteristic directions at a finite speed. For parabolic equations, the information travels at infinite speed to all spatial points and, therefore, interpolation is needed at each grid interface to advance the solution. The numerical boundary condition is, therefore, given by

$$\hat{u}_m = T_R^T \mathbf{v}, \qquad \hat{v}_0 = T_L^T \mathbf{u}, \tag{7.3}$$

$$T_R = [0 \,....\, 0 \; l_{j+1} \cdots l_{j+k_R} \; 0 \,....\, 0]^T, \qquad T_L = [0 \,....\, 0 \; l_{i+1} \cdots l_{i+k_L} \; 0 \,....\, 0]^T, \tag{7.4}$$

where T_L and T_R are vectors of sizes $m+1$ and $n+1$, respectively, and $l_{i+1}, \cdots, l_{i+k_L}$ and $l_{j+1}, \cdots, l_{j+k_R}$ denote the corresponding interpolation coefficients.

The semidiscrete approximation to the IBVP (4.1)-(7.2) on the two sub-domains of Figure 7.1 can be written, using the SBP-SAT methodology, as

$$\frac{d\mathbf{u}}{dt} = D_2^L \mathbf{u} + \sigma_1 H_L^{-1} S_L^T e_0^L (u_0 - g_1) + \sigma_2 H_L^{-1} S_L^T e_m^L (u_m - T_R^T \mathbf{v}) + \sigma_3 H_L^{-1} w_L \{(S_R \mathbf{v})_0 - T_L^T (S_L \mathbf{u})\} \tag{7.5}$$

$$\frac{d\mathbf{v}}{dt} = D_2^R \mathbf{v} + \tau_1 H_R^{-1} S_R^T e_0^R (v_0 - T_L^T \mathbf{u}) + \tau_2 H_R^{-1} S_R^T e_n^R (v_n - g_2) + \tau_3 H_R^{-1} w_R \{(S_L \mathbf{u})_m - T_R^T (S_R \mathbf{v})\} \tag{7.6}$$

where,

$$w_L = T_L, \qquad w_R = T_R, \qquad e_0^{L,R} = [1\, 0 \,\ldots\, 0]^T. \tag{7.7}$$

The vectors w_L, e_0^L and e_m^L are of size $(m+1)$, and, similarly w_R, e_0^R and e_n^R are vectors of size $(n+1)$. $D_2^{L,R}$ denotes the SBP second derivative approximation, derived by Mattsson & Nordström (2004), which

mimics the integration by parts formula,

$$\left(u, \frac{\partial^2 u}{\partial x^2}\right) + \left(\frac{\partial^2 u}{\partial x^2}, u\right) = 2u\frac{\partial u}{\partial x}\bigg|_a^b - 2\left\|\frac{\partial u}{\partial x}\right\|^2,$$

where the scalar product $(\cdot,\cdot)$ and the norm $\|\cdot\|$ is defined by Eq. (3.1). Mattsson & Nordström (2004) proposed an operator of the form $D_2 = P^{-1}(-A + BS)$ where S is an approximation of the first derivative and $B = \text{diag}(-1, 0, \ldots\ldots, 0, 1)$. H_L and H_R constitute a norm matrix H given by

$$H = \begin{bmatrix} H_L & \\ & H_R \end{bmatrix}, \quad H_L = C_L P_L, \quad H_R = C_R P_R, \tag{7.8}$$

where $C_L = \text{diag}(c_0^L, \ldots\ldots, c_m^L)$ and $C_R = \text{diag}(c_0^R, \ldots\ldots, c_n^R)$ with $c_i^{L,R} > 0$ for all i.

7.1.1 Stability Analysis

For the proof of time-stability it is sufficient to consider the case of homogeneous BC: $g_1(t) = 0$ and $g_2(t) = 0$. Applying the energy method to (7.5) and (7.6) gives

$$\frac{d}{dt}||\mathbf{u}||_{H_L}^2 = -\mathbf{u}^T(\widetilde{A}_L + \widetilde{A}_L^T)\mathbf{u} + 2(\sigma_1 - c_0^L)u_0(S_L\mathbf{u})_0 + 2(\sigma_2 + c_m^L)u_m(S_L\mathbf{u})_m - 2\sigma_2(S_L\mathbf{u})_m(T_R^T\mathbf{v})$$

$$+ 2\sigma_3(S_R\mathbf{v})_0(T_L^T\mathbf{u}) - \sigma_3\{\mathbf{u}^T[T_L T_L^T S_L + (T_L T_L^T S_L)^T]\mathbf{u}\}, \tag{7.9}$$

$$\frac{d}{dt}||\mathbf{v}||_{H_R}^2 = -\mathbf{v}^T(\widetilde{A}_R + \widetilde{A}_R^T)\mathbf{v} + 2(\tau_1 - c_0^R)\mathbf{v}_0(S_R\mathbf{v})_0 + 2(\tau_2 + c_n^R)\mathbf{v}_n(S_R\mathbf{v})_n - 2\tau_1(S_R\mathbf{v})_0(T_L^T\mathbf{u})$$

$$+ 2\tau_3(S_L\mathbf{u})_m(T_R^T\mathbf{v}) - \tau_3\{\mathbf{v}^T[T_R T_R^T S_R + (T_R T_R^T S_R)^T]\mathbf{v}\}. \tag{7.10}$$

where $\widetilde{A}_{L,R} = C_{L,R}A_{L,R}$. Assuming,

$$\sigma_1 = c_0^L, \quad \sigma_2 = -c_m^L = \tau_3, \tag{7.11}$$

$$\tau_1 = c_0^R = \sigma_3, \quad \tau_2 = -c_n^R, \tag{7.12}$$

and adding Eqs. (7.9) and (7.10), we get

$$\frac{d}{dt}||\mathbf{w}||_H^2 = -\mathbf{u}^T\{\widetilde{A}_L + c_0^R T_L T_L^T S_L + (\widetilde{A}_L + c_0^R T_L T_L^T S_L)^T\}\mathbf{u} - \mathbf{v}^T\{\widetilde{A}_R - c_m^L T_R T_R^T S_R + (\widetilde{A}_R - c_m^L T_R T_R^T S_R)^T\}\mathbf{v}, \tag{7.13}$$

where $\mathbf{w} = \begin{bmatrix} \mathbf{u} & \mathbf{v} \end{bmatrix}^T$. To prove time-stability, we need to determine the coefficients of the matrix $C_{L,R}$ such

that $R_L = \widetilde{A}_L + c_0^R T_L T_L^T S_L + (\widetilde{A}_L + c_0^R T_L T_L^T S_L)^T \geq 0$ and $R_R = \widetilde{A}_R - c_m^L T_R T_R^T S_R + (\widetilde{A}_R - c_m^L T_R T_R^T S_R)^T \geq 0$. We determine that next for the second-order scheme on a boundary overlap grid configuration as shown in Figure 7.2.

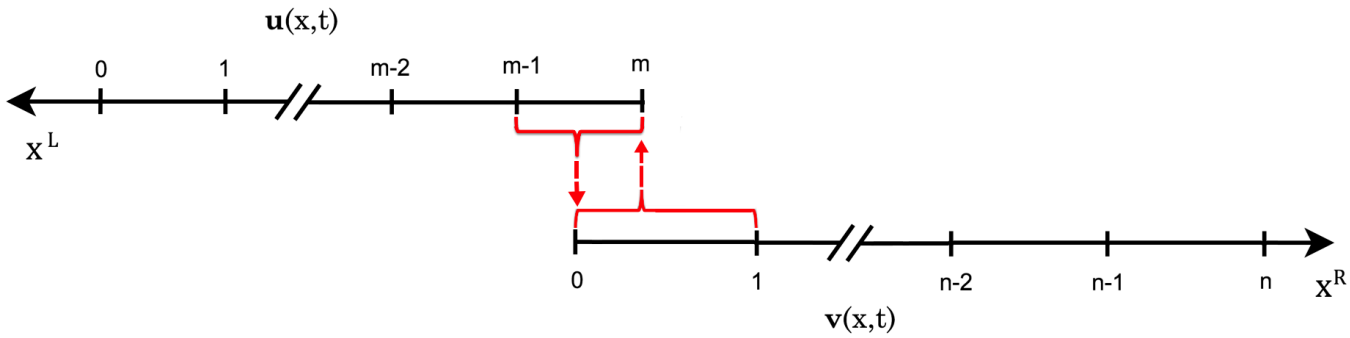

Figure 7.2: Schematic diagram of overlapping grids on which Eq.(7.1) is solved .

The operators in (7.13) for the second order scheme and the overlapping grid configuration shown in Figure 7.2 is given by

$$T_L = [0 \cdots 0 \;\; \alpha_L \;\; (1-\alpha_L)]^T, \qquad T_R = [0 \cdots 0 \;\; \alpha_R \;\; (1-\alpha_R)]^T,$$

$$A_{L,R} = \tfrac{1}{h_{L,R}} \begin{bmatrix} 1 & -1 & & & \\ -1 & 2 & -1 & & \\ & \ddots & \ddots & \ddots & \\ & & -1 & 2 & -1 \\ & & & -1 & 1 \end{bmatrix}, \qquad S_{L,R} = \tfrac{1}{h_{L,R}} \begin{bmatrix} -\frac{3}{2} & 2 & -\frac{1}{2} & & \\ -\frac{1}{2} & 0 & \frac{1}{2} & & \\ & \ddots & \ddots & \ddots & \\ & & -\frac{1}{2} & 0 & \frac{1}{2} \\ & & \frac{1}{2} & -2 & \frac{3}{2} \end{bmatrix}.$$

The R_L matrix then comprises of (the subscript 'L' has been dropped from 'α_L' to simplify notation),

$$T_L T_L^T = \begin{bmatrix} 0 & .. & .. & .. & .. & 0 \\ 0 & .. & .. & .. & .. & 0 \\ . & .. & .. & .. & .. & . \\ . & .. & .. & .. & .. & . \\ 0 & .. & .. & 0 & \alpha^2 & \alpha(1-\alpha) \\ 0 & .. & .. & 0 & \alpha(1-\alpha) & (1-\alpha)^2 \end{bmatrix},$$

$\widetilde{A}_L + c_0^R I_L I_L^T S_L =$

$$\frac{1}{h_L}\begin{bmatrix} c_0^L & -c_0^L & & & & & \\ -c_1^L & 2c_1^L & -c_1^L & & & & \\ & \ddots & \ddots & \ddots & & & \\ . & .. & -c_{m-2}^L & 2c_{m-2}^L & -c_{m-2}^L & . \\ 0 & .. & .. & -c_{m-1}^L - c_0^R\frac{\alpha^2}{2} + c_0^R\frac{\alpha(1-\alpha)}{2} & 2c_{m-1}^L - 2c_0^R\alpha(1-\alpha) & -c_{m-1}^L + c_0^R\frac{\alpha^2}{2} + \frac{3c_0^R\alpha(1-\alpha)}{2} \\ 0 & .. & .. & \frac{c_0^R(1-\alpha)^2}{2} - c_0^R\frac{\alpha(1-\alpha)}{2} & -c_m^L - 2c_0^R(1-\alpha)^2 & c_m^L + \frac{3c_0^R(1-\alpha)^2}{2} + c_0^R\frac{\alpha(1-\alpha)}{2} \end{bmatrix},$$

$$R_L = \widetilde{A}_L + c_0^R I_L I_L^T S_L + (\widetilde{A}_L + c_0^R I_L I_L^T S_L)^T.$$

Similarly we obtain the R_R matrix. For R_L and R_R to be positive semidefinite all its eigenvalues must be greater than or equal to zero. Using the Gershgorin circle theorem, all eigenvalues of R_L and R_R are greater than or equal to zero, if the coefficients of the matrices C_L and C_R are chosen as

$$r_1,\ r_2 \in \mathbb{R}^+, \qquad c_m^L = k_1, \qquad c_0^R = k_2,$$

$$c_0^L = c_1^L = c_2^L = ... = c_{m-2}^L = k_1 + k_2, \qquad c_{m-1}^L = k_1 + k_2(\frac{3}{2} - \alpha_L), \tag{7.14}$$

$$c_1^R = k_1(\tfrac{1}{2} + \alpha_R) + k_2, \qquad c_2^R = ... = c_n^R = k_1 + k_2.$$

7.1.2 Numerical Results

We solve the heat equation (7.1)–(7.2) with homogeneous Dirichlet boundary conditions and initial condition $f(x) = \sin(\pi x)$. Figure 7.3 shows the solution at different times which compares well with the exact solution shown as dotted black line in the figure. Figure 7.4 shows the eigenvalue spectrum of the system matrix for method (7.5)-(7.6). As desired for time-stability, all eigenvalues lie in the left half of the complex plane. Figure 7.5 shows the convergence result for the second-order scheme discussed in the previous section. The classical fourth-order Runge-Kutta (RK4) method was used for the temporal integration with a constant CFL of 0.25 in error calculations. The refinements carried out for the convergence analysis maintained a grid point ratio of $3:2$ between the left and the right domain.

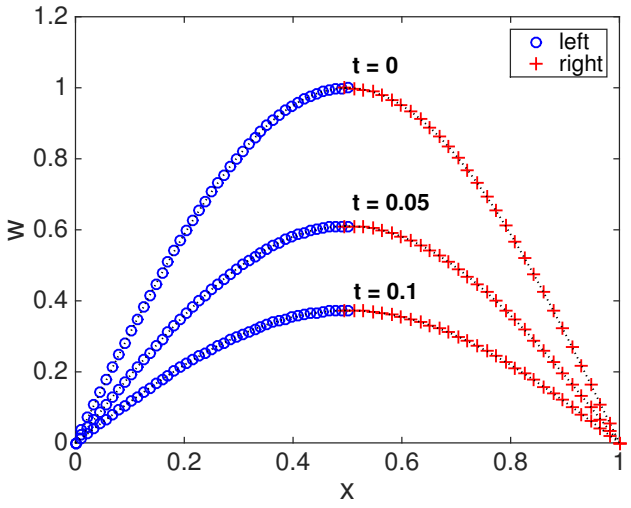

Figure 7.3: Solution to the heat equation with an initial sine profile. Blue circles show the solution on the left domain and red pluses on the right domain. Dotted black line shows the exact solution.

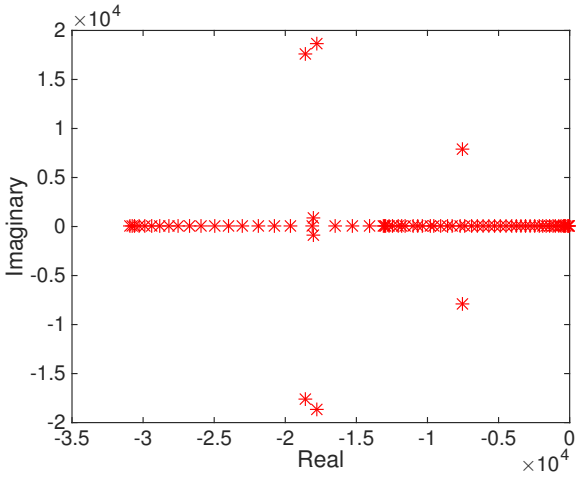

Figure 7.4: Eigenvalues of the system matrix M with 45 grid points on the left domain and 30 grid points on the right domain.

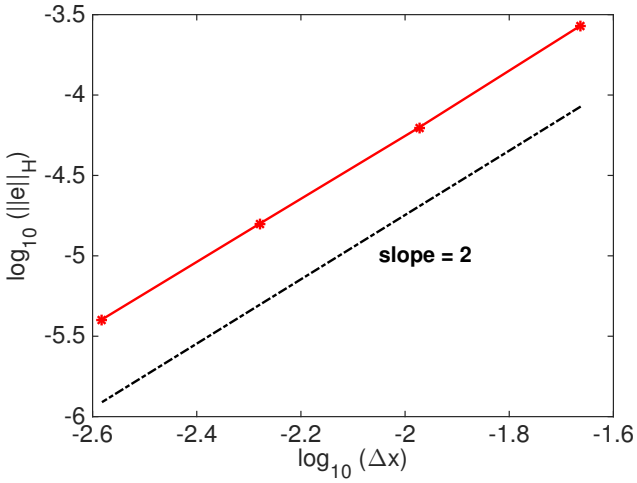

Figure 7.5: Convergence plot for the method (7.5)-(7.6) for the second-order accurate scheme. $\triangle x$ denotes the grid spacing on the left domain.

7.2 Overset Interface Treatment for the Compressible Navier-Stokes Equations

The three-dimensional Navier-Stokes equations for compressible fluid flow is solved in generalized coordinates. The coordinate transformation between the physical domain $\mathbf{x} = (x, y, z)$ and the computational

domain $\boldsymbol{\xi} = (\xi, \eta, \zeta)$ is $\boldsymbol{\xi} = \boldsymbol{\Xi}(\mathbf{x}, t)$ with the inverse transformation $\mathbf{x} = \mathbf{X}(\boldsymbol{\xi}, \tau)$ and the metric Jacobian $J = \det(\partial\boldsymbol{\xi}/\partial\mathbf{x})$. We assume the time to be invariant, therefore, $\tau = t$. The transformed governing equations are then given by

$$\frac{\partial Q}{\partial \tau} + \frac{\partial}{\partial \xi_i}(F_i^I - F_i^V) = 0, \tag{7.15}$$

where $Q = J^{-1}\begin{bmatrix}\rho & \rho u & \rho v & \rho w & \rho E\end{bmatrix}^T$. Additionally, ρ denotes the density, $\mathbf{u} = (u_1, u_2, u_3) = (u, v, w)$ are the Cartesian velocity components, p denotes the pressure and E is the total energy per unit mass given by

$$E = \frac{p}{\rho(\gamma - 1)} + \frac{1}{2}(u^2 + v^2 + w^2).$$

The flow variables are non-dimensionalized by a reference length scale L^*, velocity scale c^*_∞ (ambient speed of sound), density scale ρ^*_∞, pressure scale $\rho^*_\infty {c^*_\infty}^2$, temperature scale ${c^*_\infty}^2/C^*_{p,\infty} = (\gamma - 1)T^*_\infty$ and viscosity μ^*_∞. A dimensional variable is denoted by $*$ whereas ∞ denotes a ambient quantity. $\gamma = C^*_p/C^*_v$ is the ratio of the specific heat at a constant pressure to the specific heat at a constant volume. Reynolds number and the Prandtl number are defined as $Re = \rho^*_\infty c^*_\infty L^*/\mu^*_\infty$ and $Pr = \mu^* C^*_p/k^*$, respectively, where k^* denotes the thermal conductivity. The inviscid fluxes are given by

$$F_1^I = \frac{1}{J}\begin{bmatrix}\rho U \\ \rho u U + p\xi_x \\ \rho v U + p\xi_y \\ \rho w U + p\xi_z \\ (\rho E + p)U - \xi_t p\end{bmatrix}, \quad F_2^I = \frac{1}{J}\begin{bmatrix}\rho V \\ \rho u V + p\eta_x \\ \rho v V + p\eta_y \\ \rho w V + p\eta_z \\ (\rho E + p)V - \eta_t p\end{bmatrix}, \quad F_3^I = \frac{1}{J}\begin{bmatrix}\rho W \\ \rho u W + p\zeta_x \\ \rho v W + p\zeta_y \\ \rho w W + p\zeta_z \\ (\rho E + p)W - \zeta_t p\end{bmatrix},$$

where the contravariant velocities are

$$U = \xi_t + \xi_x u + \xi_y v + \xi_z w, \qquad V = \eta_t + \eta_x u + \eta_y v + \eta_z w, \qquad W = \zeta_t + \zeta_x u + \zeta_y v + \zeta_z w,$$

and the viscous fluxes are $F_1^V = J^{-1}(\xi_{x_i}\hat{F}_i^V)$, $F_2^V = J^{-1}(\eta_{x_i}\hat{F}_i^V)$ and $F_3^V = J^{-1}(\zeta_{x_i}\hat{F}_i^V)$ where

$$\hat{F}_1^V = \begin{bmatrix}0 \\ \tau_{11} \\ \tau_{12} \\ \tau_{13} \\ u_j\tau_{1j} - q_1\end{bmatrix}, \quad \hat{F}_2^V = \begin{bmatrix}0 \\ \tau_{21} \\ \tau_{22} \\ \tau_{23} \\ u_j\tau_{2j} - q_2\end{bmatrix}, \quad \hat{F}_3^V = \begin{bmatrix}0 \\ \tau_{31} \\ \tau_{32} \\ \tau_{33} \\ u_j\tau_{3j} - q_3\end{bmatrix}.$$

The stress tensor and the heat flux is given by

$$\tau_{ij} = \frac{\mu}{Re}\left(\frac{\partial u_i}{\partial x_j} + \frac{\partial u_j}{\partial x_i}\right) + \frac{\lambda}{Re}\frac{\partial u_k}{\partial x_k}\delta_{ij}, \qquad q_i = -\frac{\mu}{Re\,Pr}\frac{\partial T}{\partial x_i},$$

where the viscosity is modeled as a power law $\mu = [(\gamma-1)T]^n$ with $n = 0.666$ to model air and the second coefficient of viscosity is $\lambda = \mu_B - \frac{2}{3}\mu$ where $\mu_B = 0.6\mu$ is chosen as a model for bulk viscosity of air. The non-dimensional ideal gas law is

$$p = \frac{\gamma-1}{\gamma}\rho T.$$

For more details on the governing equations used in the solver employed to perform the simulation discussed in the next section, see Kim (2012, Section 3.1).

In order to simplify the presentation, let us consider a single grid point on an overlapping interface, say a $\kappa^{\pm}$ boundary where $\kappa = \xi, \eta$ or ζ. κ is the direction normal to the face on which the interface point lies and $\pm$ indicates an inflow $(+)$ or an outflow $(-)$ boundary. If the interface point lies on an edge or a corner then the interface terms for each normal direction (2 for an edge and 3 for a corner) must be added. Let the solution at the grid point be denoted by $\mathbf{q}_{ijk}$ and the interpolated value at the grid point, from the donor grid, be given by $\hat{\mathbf{q}}_{ijk}$. For the viscous interface treatment, we also need the interpolated viscous flux given by $\hat{F}^V_\kappa = \kappa_x\hat{F}^V_1 + \kappa_y\hat{F}^V_2 + \kappa_z\hat{F}^V_3$, where $\hat{F}^V_1$, $\hat{F}^V_2$ and $\hat{F}^V_3$ are the interpolated values from the underlying grid. The discretization at the interface point can then be written as

$$\frac{d\mathbf{q}_{ijk}}{dt} = -\left(D_{\xi_m}\mathbf{F}_m\right)_{ijk} - p_0^{-1}(\sigma^I K^{\pm}_\kappa + \sigma^V_1 I_5)\left(\mathbf{q}_{ijk} - \hat{\mathbf{q}}_{ijk}\right) + \sigma^V_2\left((F^V_\kappa)_{ijk} - (\hat{F}^V_\kappa)_{ijk}\right),$$

where $\left(D_{\xi_m}\mathbf{F}_m\right)_{ijk}$ denotes the derivatives of the fluxes, $\mathbf{F}_m = \mathbf{F}^I_m - \mathbf{F}^V_m$, at the interface point, p_0 is the $(1,1)$ element of the P matrix (see A), I_5 is an identity matrix of size 5×5 and $K^{\pm}_\kappa = S_\kappa\left(\frac{|\Lambda_\kappa|\pm\Lambda_\kappa}{2}\right)S^{-1}_\kappa$. The expressions for Λ_κ and S_κ can be found in Pulliam & Chaussee (1981). $(F^V_\kappa)_{ijk}$ denotes the viscous flux at the interface point; $F^V_\kappa = F^V_1$ if $\kappa = \xi$; $F^V_\kappa = F^V_2$ if $\kappa = \eta$; $F^V_\kappa = F^V_3$ if $\kappa = \zeta$. The penalty parameters, assuming that the same derivative approximation is used on both the donor and the receiver grid, are given by $\sigma^I \geq \frac{1}{2}$, $\sigma^V_1 = \frac{1}{2\,Re}(\kappa_x^2 + \kappa_y^2 + \kappa_z^2)$ and $\sigma^V_2 = \pm\frac{1}{2}$ for an inflow$(+)$/outflow $(-)$ interface point. For an inviscid flow, the above method reduces to the SAT method of Section 5.3.1 without the dissipation term.

7.3 LES of Flow Over a Hill

In order to test the interface treatment discussed in the previous section, we perform a numerical simulation of the flow over a cosine-shaped hill with geometry as described in Bell *et al.* (2012). The flow has several

interesting features such as a three-dimensional boundary layer separation, reattachment of a turbulent shear layer and recirculating flow which are critical to the design and analysis of aircraft wings, fuselage, fan, turbine and compressor blades, among other applications.

7.3.1 Computational Domain

The overset domain used for the simulation is shown in Figure 7.6. Since most of the interesting flow behavior occurs in the wake of the hill, we use a small block shown in red in Figure 7.6 with a fine grid and a relatively coarser base block, shown in black. The base domain extends from $-8H$ to $14H$ in the x-direction, $-4H$ to $4H$ in the y-direction and upto $4H$ in the $z-$direction, whereas the finer domain extends from $-0.4H$ to $6H$ in the x-direction, $-2H$ to $2H$ in the y-direction and upto $3H$ in the $z-$direction. H denotes the height of the hill, centered at the origin. $401 \times 151 \times 151$ grid points are used on the base grid, whereas $201 \times 101 \times 201$ grid points are used on the finer grid. Figure 7.7 shows the grid on a slice near centerline. The overlapping grid points on the coarser grid are blanked out, which shows up as a hole in Figure 7.7 on the base grid.

7.3.2 Flow Parameters and Numerical Simulation

We perform a large-eddy simulation with Reynolds number based on the hill height $Re = Hc_\infty/\nu = 500,000$ and free stream Mach number $M_\infty = U_\infty/c_\infty = 0.145$. The dynamic Smagorinsky eddy viscosity model for compressible turbulence (Moin *et al.*, 1991) with Lilly's improvement (Lilly, 1992) is used to determine the subgrid scale contributions. The detailed formulation implemented in the solver, used for the simulation, can be found in Kim (2012, Section 4.1.7). In order to prevent the denominator in the calculation of the model coefficients from being zero, both the numerator and the denominator are often averaged in the direction(s) of flow homogeneity. But the flow over the hill lacks homogeneity in all directions, therefore we perform a local Gaussian averaging in directions parallel to the wall. See Appendix B for the stencils used for averaging.

The flow is initialized using uniform density $\rho/\rho_\infty = 1$ and pressure $p/\rho_\infty c_\infty^2 = 1/\gamma$, and a Polhausen boundary layer velocity profile

$$\frac{u}{U_\infty} = \begin{cases} 1 & z - z_0 \geq \delta \\ \frac{3}{2}\eta - \frac{1}{2}\eta^3 & z - z_0 < \delta \end{cases},$$

where $\eta = (z - z_0)/\delta$ and $\delta = H/4$. z_0 is the hill elevation at the (x, y) location given by

$$z_0(x, y) = \begin{cases} \frac{H}{2}\left(\cos\left(\frac{\pi}{R}r\right) + 1\right) & r \leq R \\ 0 & r > R \end{cases},$$

where $R = \frac{3H}{2}$ and $r = \sqrt{x^2 + y^2}$.

Figure 7.8 shows the streamwise momentum and the vorticity magnitude contours at different times on a slice with an overset interface. In order to validate the overset interface treatment, we performed a single grid simulation with $501 \times 181 \times 201$ grid points on the domain shown with black outline in Figure 7.6. Figure 7.9 shows the pressure coefficient comparison along the wall on the centerline $y = 0$ between the time-averaged results from the single grid and the overset grid simulation.

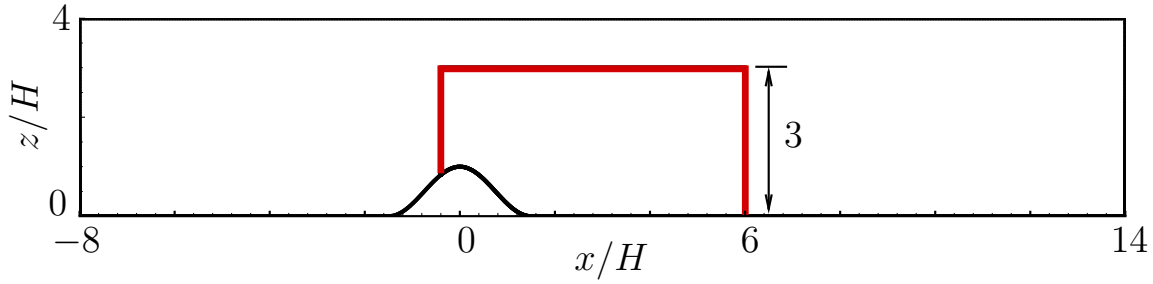

(a)

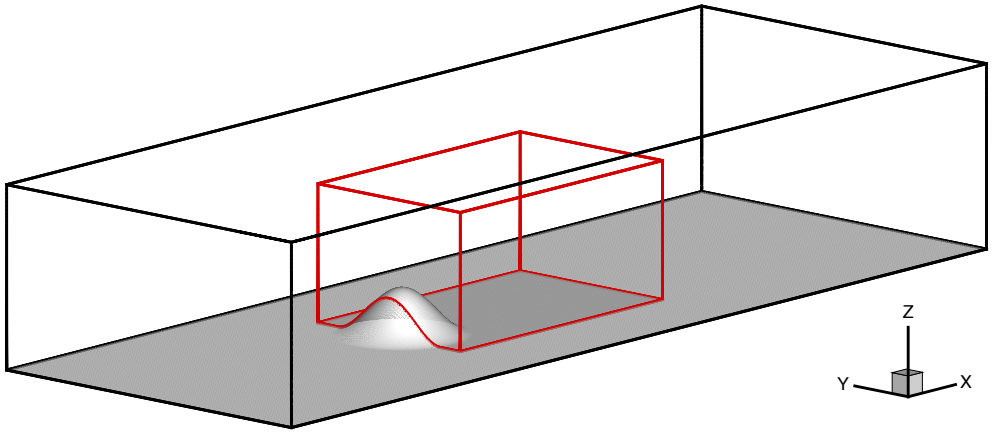

(b)

Figure 7.6: Overlapping domain for the hill simulation. Red outline shows the domain with finer grid downstream of the hill. (a) $x - z$ view at the centerline $y = 0$. (b) 3-D view.

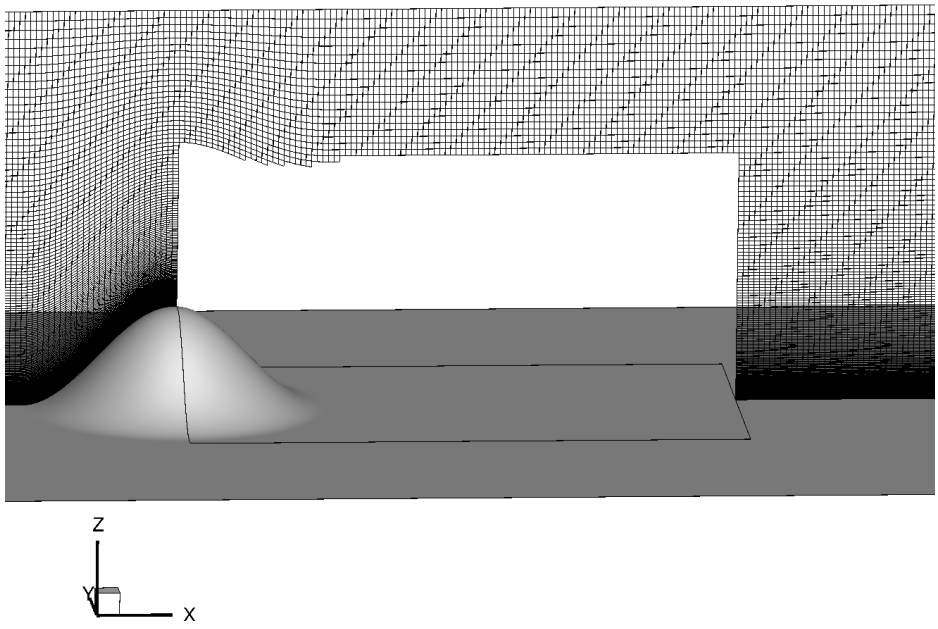

(a)

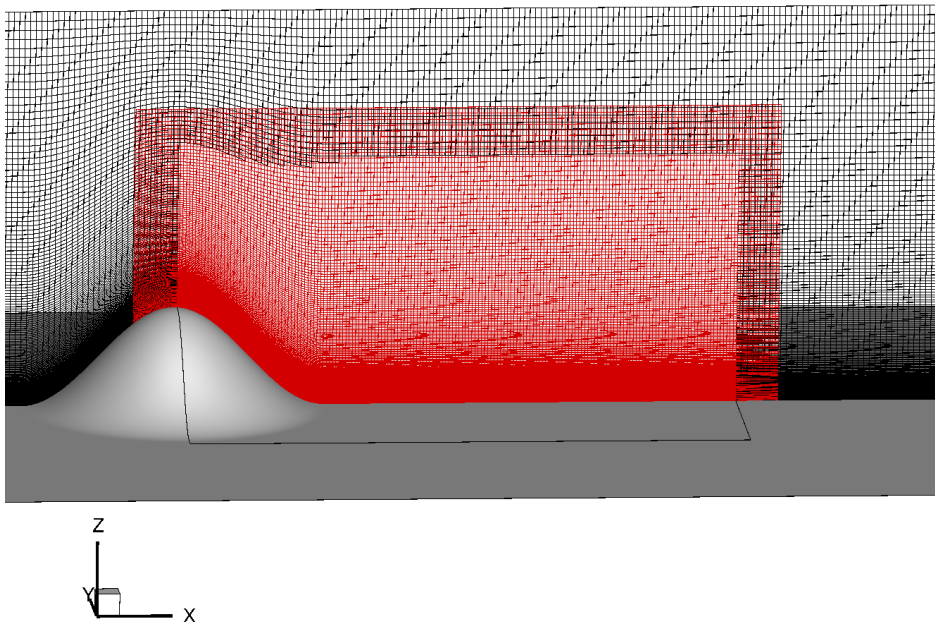

(b)

Figure 7.7: Grid on a slice near the centerline $y = 0$. (a) Coarser base grid. (b) Overset grid.

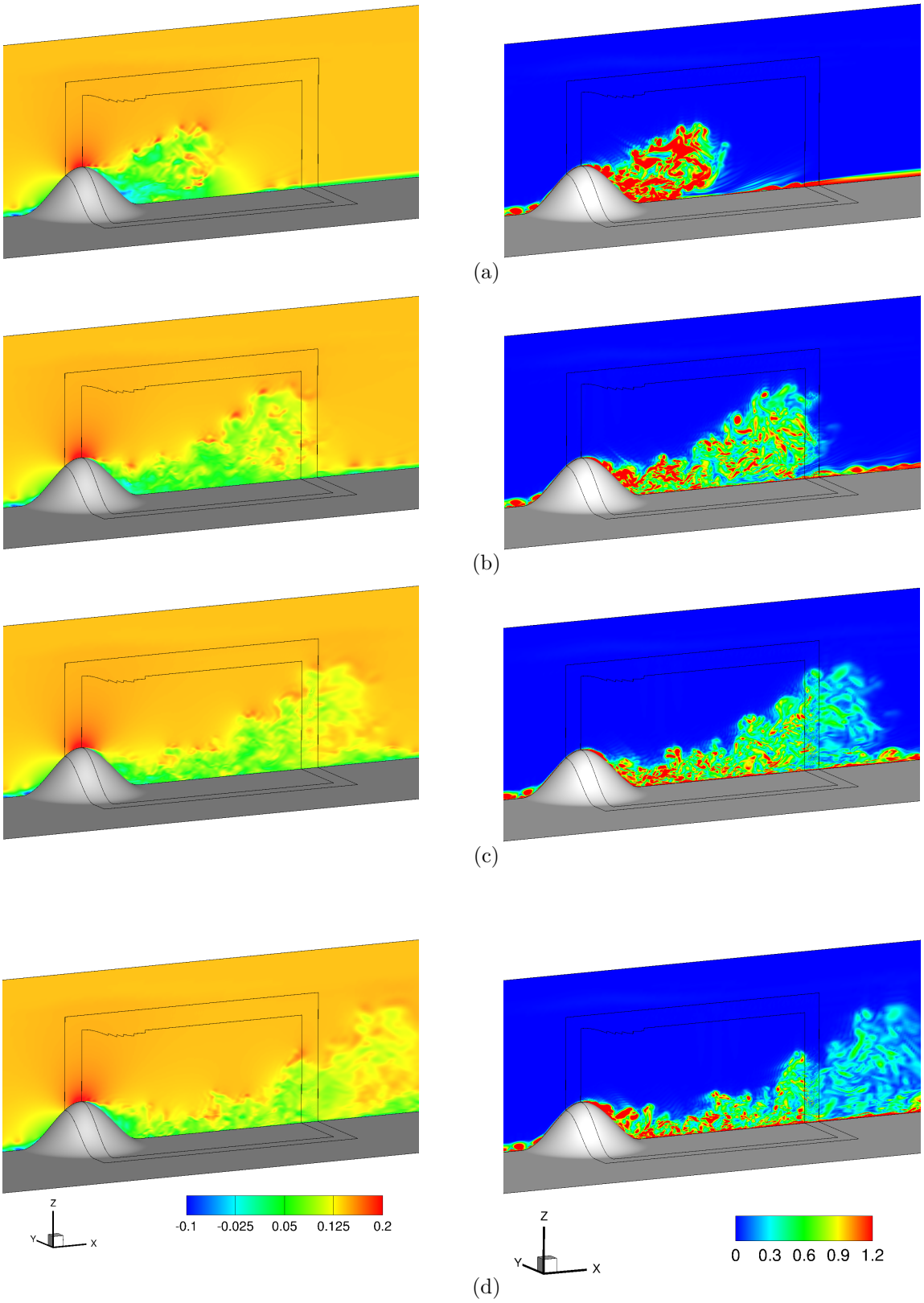

Figure 7.8: Contours of streamwise momentum ($\rho u/\rho_\infty c_\infty$) on the left column and vorticity magnitude ($|\boldsymbol{\omega} H/c_\infty|$) on the right column at different times: a) $tc_\infty/H = 43$, b) $tc_\infty/H = 62.4$, c) $tc_\infty/H = 73$, d) $tc_\infty/H = 82.9$.

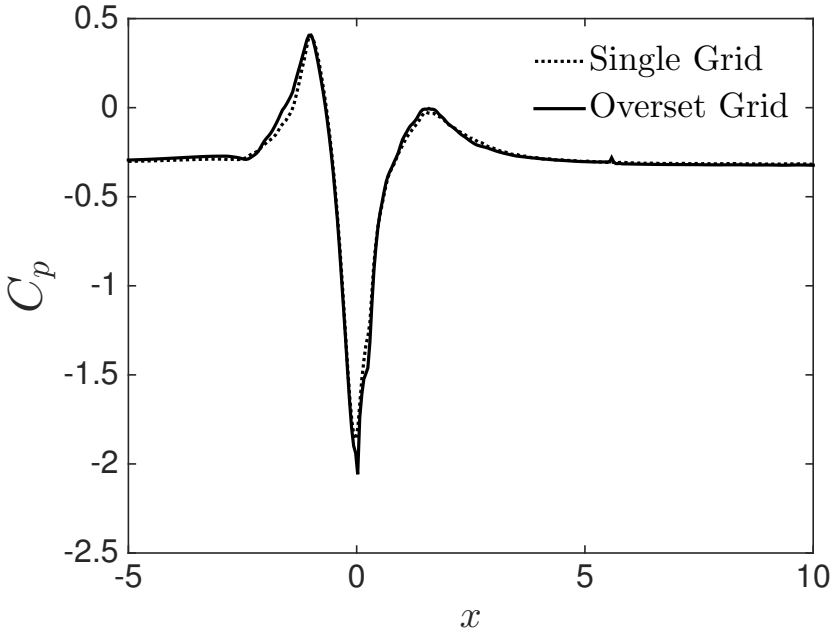

Figure 7.9: Comparison of pressure coefficient along the hill surface at the center plane.

Chapter 8

Conclusions and Perspectives

Time-stable overset methods based on the SBP-SAT methodology were developed for hyperbolic problems. We looked at the sufficient conditions for time-stability and discussed two cases of the SAT method for interface treatment on overset grids. In the first case, we proved stability by analyzing the eigenvalues of the system matrix. This approach was successful for the hyperbolic problems since they have a characteristic direction of propagation which yielded system matrices whose eigenvalues could be estimated. As discussed in section 4.3.4, the system matrix may not always be in a form amenable to the eigenvalue analysis and therefore a more general treatment using the energy method was needed where a dissipative operator was used to locally upwind the derivative stencils at a few grid points on the donor grid to ensure stability. The solution error comparison between the injection method and the SAT methods showed a superior performance of the SAT-based approach, and the convergence tests confirmed that the interface treatment with the appropriate order of interpolation does not lower the accuracy of the spatial finite difference operator. It is also extremely straightforward to incorporate the SAT method of interface treatment in an existing SBP-SAT based solver.

The SAT method without dissipation, discussed in Chapter 4, was proven time-stable regardless of the interpolation method used and the location of the donor points and therefore one can choose appropriate interpolation coefficients to ensure global conservation. The proof of stability was also independent of the order of accuracy of the derivative operators, provided they satisfied the SBP property. Therefore, the SAT method without dissipation permits the use of different orders of approximation in different subdomains of the computational domain.

The proof of stability for the SAT method with the dissipation term, discussed in Chapter 5, depends on the interpolation details and the derivative approximation used. Therefore, the analysis was categorized into the boundary overlap and the interior overlap scenarios for each order of the scheme. We showed time-stability for a boundary overlap case of the second- and the third-order accurate scheme and for the interior overlap case of the second-, third- and the fourth-order accurate schemes. Using the same procedure, stability for the remaining boundary overlap cases and for the fifth or higher-order schemes could also be shown. This case-by-case approach for overset grids differs from the analysis of the SBP-SAT methods for

the single and the multiblock grids where one proof of stability, conveniently, worked for all orders of the schemes. It is a consequence of the fact that in imposing the boundary conditions (physical or numerical) for a single or a multiblock domain only the boundary points of each (sub-)domain are involved and the SBP property of the derivative operators on each (sub-)domain provides the quadratic terms for the boundary points, required to obtain an energy estimate. In contrast, on overlapping domains, the interior points are involved in imposing the numerical boundary conditions (via interpolation), and the quadratic terms for the interior points can only be obtained by altering the derivative stencils since the central difference first derivative approximation does not generate quadratic terms, in stability analysis using the energy method, owing to a zero entry on the diagonal. In this work, a dissipation term was used to alter the stencils of the interior points. No general criterion, like the SBP property, yields a quadratic term of the interior points for all orders and therefore a case-by-case analysis becomes unavoidable for obtaining an energy estimate.

The energy bound for the SAT method in Chapter 5 was shown in the H-norm which provides a quadrature, as discussed in Chapter 6, for approximating the conserved quantity of the domain. All proofs in this work were for one-dimensional domains. Though the performance benefits were observed in the proposed extension to higher dimensions, it is tempting to attempt a two-dimensional proof. The 2-D space offers a much wider range of overlapping scenarios than 1-D. The one-dimensional results of Chapters 4-6 may readily apply to simpler 2-D overlapping configurations, for example, when the grids are aligned such that a 1-D interpolation suffices. But for arbitrary overlaps, the complete analysis may have to be redone. The biggest challenge in proving stability in Chapter 5 was the complexity of the algebraic equation that had to be analyzed to ensure the negative semi-definiteness of the matrix $HM + M^T H$. For the third- and the fourth-order scheme with cubic interpolation, a 5×5 matrix (see Eqs. (5.64) and (5.70)) had to analyzed. Fortunately, we had enough free parameters in the problem that allowed us to make most of the off-diagonal terms zero to simplify the analysis. In the process it provided a single set of values that work for all overlapping configurations. But when additional constraints from the conservation analysis in Chapter 6 was imposed, the cancellation of the off-diagonal terms was no longer possible for the third-order scheme and hence a closed-form expression for the parameter values could not be obtained. Similar, if not greater, challenges of algebraic complexity should be expected in the analysis of the 2-D overlapping configurations.

Future work in the increasing order of perceived difficulty may include the following tasks:

1. *Analyze and show conservation for the SAT method without dissipation.* The framework for analyzing the conservation was provided in Chapter 6, where it was highlighted how the characteristic direction based interface treatment of the SAT method differs from the injection method, and its influence on the conserved quantity of the domain. The first step in establishing conservation would be to

identify the quantity that must be conserved followed by determining a quadrature for the domain. The interpolation coefficients then will have to be determined such that the interface terms cancel out. Since the SAT method without dissipation was proven time-stable regardless of the interpolation method used, the interpolation coefficients act as free parameters in the analysis. The conservation analysis in two- and three-dimensions for this method is a much more feasible proposition than the stability analysis since conservation requires solving a set of linear equations as compared to non-linear algebraic equations for stability.

2. *Show 1-D stability for incompletely parabolic equations on overlapping grids.* In this work, we showed the time-stability for hyperbolic (Chapters 4–5) and parabolic (Section 7.1) equations but the norms in which the energy bound for each was shown was different which means that the time-stability of the advection equation and the heat equation individually does not guarantee the time-stability of the linear advection-diffusion equation. Sharan & Bodony (2013) discussed an approach for construction of a time-stable SBP-SAT based method for linear advection-diffusion equation but the proof there was found to depend on the cell Reynolds number.

3. *2-D stability analysis for overlapping grids.* As discussed earlier, this is a challenging task due to the algebraic complexity of examining the definiteness of the $HM + M^T H$ matrix. One can simplify the analysis by considering simpler overlapping configurations to begin with, such as a patch refined mesh as discussed in Kramer *et al.* (2009), before tackling the case of arbitrary overlaps. One approach, not investigated in this thesis, that may be helpful is the application of Sylvester's Theorem, discussed in Carpenter *et al.* (2010), to rotate a symmetric matrix into a diagonal form without changing the signs of the eigenvalues.

Appendix A

SBP First Derivative Approximations

This appendix contains the SBP operators for first derivative approximation denoted by $D = P^{-1}Q$. In this thesis, we used only the explicit operators which are based on a diagonal norm. They are referred to as $r - 2r - r$ operators, where r denotes the order of accuracy at the boundary points and $2r$ is the order of accuracy in the interior.

A.1 1 - 2 - 1 Operators

$$P = h \begin{bmatrix} \frac{1}{2} & & & & & & \\ & 1 & & & & & \\ & & \ddots & & & & \\ & & & \ddots & & & \\ & & & & 1 & & \\ & & & & & \frac{1}{2} \end{bmatrix}, \quad Q = \begin{bmatrix} -\frac{1}{2} & \frac{1}{2} & 0 & & & & \\ -\frac{1}{2} & 0 & \frac{1}{2} & & & & \\ & \ddots & \ddots & \ddots & & & \\ & & \ddots & \ddots & \ddots & & \\ & & & -\frac{1}{2} & 0 & \frac{1}{2} & \\ & & & & -\frac{1}{2} & \frac{1}{2} \end{bmatrix}. \tag{A.1}$$

A.2 2 - 4 - 2 Operators

For $2-4-2$ and $3-6-3$ operators, we show the stencil for one side of the boundary. The other boundary will be the mirror-opposite for the norm matrix P and negative of the mirror-opposite for the operator Q.

$$P = h \begin{bmatrix} \frac{17}{48} & & & & & & \\ & \frac{59}{48} & & & & & \\ & & \frac{43}{48} & & & & \\ & & & \frac{49}{48} & & & \\ & & & & 1 & & \\ & & & & & \ddots & \end{bmatrix},$$

$$Q = \begin{bmatrix} -\frac{1}{2} & \frac{59}{96} & -\frac{1}{12} & -\frac{1}{32} & & & & \\ -\frac{59}{96} & 0 & \frac{59}{96} & 0 & & & & \\ \frac{1}{12} & -\frac{59}{96} & 0 & \frac{59}{96} & -\frac{1}{12} & & & \\ \frac{1}{32} & 0 & -\frac{59}{96} & 0 & \frac{2}{3} & -\frac{1}{12} & & \\ & & \frac{1}{12} & -\frac{2}{3} & 0 & \frac{2}{3} & -\frac{1}{12} & \\ & & & \ddots & \ddots & \ddots & \ddots & \ddots \end{bmatrix}.$$

A.3 3-6-3 Operators

$$P = h \begin{bmatrix} \frac{13649}{43200} & & & & & & & \\ & \frac{12013}{8640} & & & & & & \\ & & \frac{2711}{4320} & & & & & \\ & & & \frac{5359}{4320} & & & & \\ & & & & \frac{7877}{8640} & & & \\ & & & & & \frac{43801}{43200} & & \\ & & & & & & 1 & \\ & & & & & & & \ddots \end{bmatrix},$$

$$Q = \begin{bmatrix} -\frac{1}{2} & \frac{127}{211} & \frac{35}{298} & -\frac{32}{83} & \frac{89}{456} & -\frac{2}{69} & & & & \\ -\frac{127}{211} & 0 & -\frac{1}{167} & \frac{391}{334} & -\frac{50}{71} & \frac{14}{99} & & & & \\ -\frac{35}{298} & \frac{1}{167} & 0 & -\frac{34}{79} & \frac{90}{113} & -\frac{69}{271} & & & & \\ \frac{32}{83} & -\frac{391}{334} & \frac{34}{79} & 0 & \frac{6}{25} & \frac{31}{316} & \frac{1}{60} & & & \\ -\frac{89}{456} & \frac{50}{71} & -\frac{90}{113} & -\frac{6}{25} & 0 & \frac{37}{56} & -\frac{3}{20} & \frac{1}{60} & & \\ \frac{2}{69} & -\frac{14}{99} & \frac{69}{271} & -\frac{31}{316} & -\frac{37}{56} & 0 & \frac{3}{4} & -\frac{3}{20} & \frac{1}{60} & \\ & & & -\frac{1}{60} & \frac{3}{20} & -\frac{3}{4} & 0 & \frac{3}{4} & -\frac{3}{20} & \frac{1}{60} \\ & & & & \ddots & \ddots & \ddots & \ddots & \ddots & \ddots \end{bmatrix}.$$

Appendix B

Stencils for Numerical Filter and Gaussian Averaging

B.1 Tenth-Order Implicit Filter (Visbal & Gaitonde, 2002)

$$2\left(\alpha_f \hat{f}_{i-1} + \hat{f}_i + \alpha_f \hat{f}_{i+1}\right) = \frac{2(193+126\alpha_f)}{256} f_i + \frac{105+302\alpha_f}{256}(f_{i+1}+f_{i-1}) + \frac{15(-1+2\alpha_f)}{64}(f_{i+2}+f_{i-2}) + \frac{45(1-2\alpha_f)}{512}(f_{i+3}+f_{i-3}) + \frac{5(-1+2\alpha_f)}{256}(f_{i+4}+f_{i-4}) + \frac{(1-2\alpha_f)}{512}(f_{i+5}+f_{i-5})$$

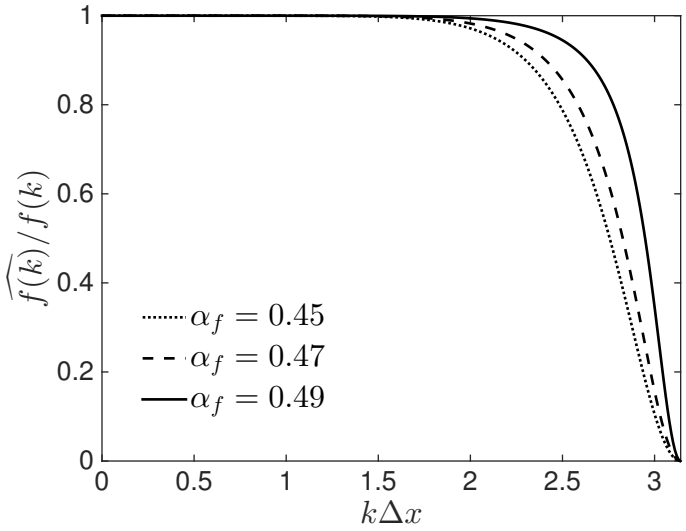

Figure B.1: Transfer function for the implicit filter.

B.2 Local Gaussian Averaging (Cook & Cabot, 2004)

$$\bar{f}_i = \frac{3565}{10368} f_i + \frac{3091}{12960}(f_{i+1}+f_{i-1}) + \frac{1997}{25920}(f_{i+2}+f_{i-2}) + \frac{149}{12960}(f_{i+3}+f_{i-3}) + \frac{107}{103680}(f_{i+4}+f_{i-4})$$

Appendix C

Comments on the SAT Method with Dissipation

In Section 5.3.2 we discussed the results of the SAT method with dissipation, where the dissipation was added to the interpolation donor points. Figures 5.13 and 5.14 show that adding dissipation to the SAT method marginally increases the L_2-norm of the error of some flow quantities for the convecting vortex flow on the grid configuration shown in Figure 4.15 with $\theta = \frac{\pi}{4}$. The introduction of dissipation to the donor grid points creates a zone that influences the error in the domain in the following two ways: a) It suppresses the numerical reflections from the internal (subdomain) boundaries, as observed in Figure 5.11 for the overset configuration of Figure 5.9; b) It emits radiated waves on interaction with an incident wave. Trefethen (1985) and the references therein discuss the numerical reflections from interfaces of similar kind.

In general we have observed that when the dissipation is added along grid lines, as in the case of grid configuration shown in Figure 5.9, the radiated waves from the dissipation zone are minimal and therefore a considerable reduction of error was observed in Figure 5.11 for the SAT method with dissipation. In contrast when the donor grid points criss-cross through the grid lines, for e.g. in Figure 5.12, the errors due to the radiated waves tend to exceed the reduction in error from suppression of the numerical reflections from internal (subdomain) boundaries. Therefore a higher error was observed for some flow variables in Figures 5.13 and 5.14. To verify whether adding dissipation along the grid lines may assist in error reduction, we added dissipation to the grid points shown in red in Figure C.1 where each of the red bands are located 10 grid points away from the respective internal boundaries. Figures C.2 and C.3 show the density, entropy, velocity magnitude and pressure error comparisons between the "injection method" of interface treatment and the SAT methods, where dissipation was added to the grid points shown in red in Figure C.1, for advection at a supersonic ($u_0 = 2.0$, $M_0 \approx 1.69$) and subsonic ($u_0 = 0.5$, $M_0 \approx 0.42$) velocity, respectively. A comparison with Figures 5.13 and 5.14 shows the improvement in performance due to the reduced radiated waves from the dissipation zone when dissipation is added along the grid lines.

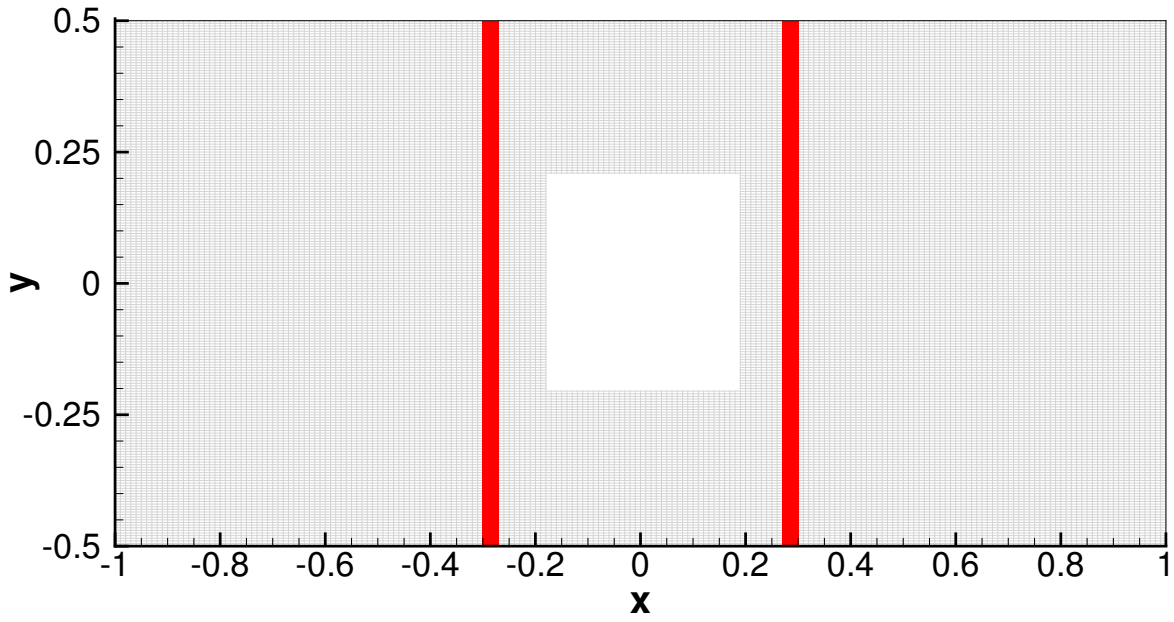

(a)

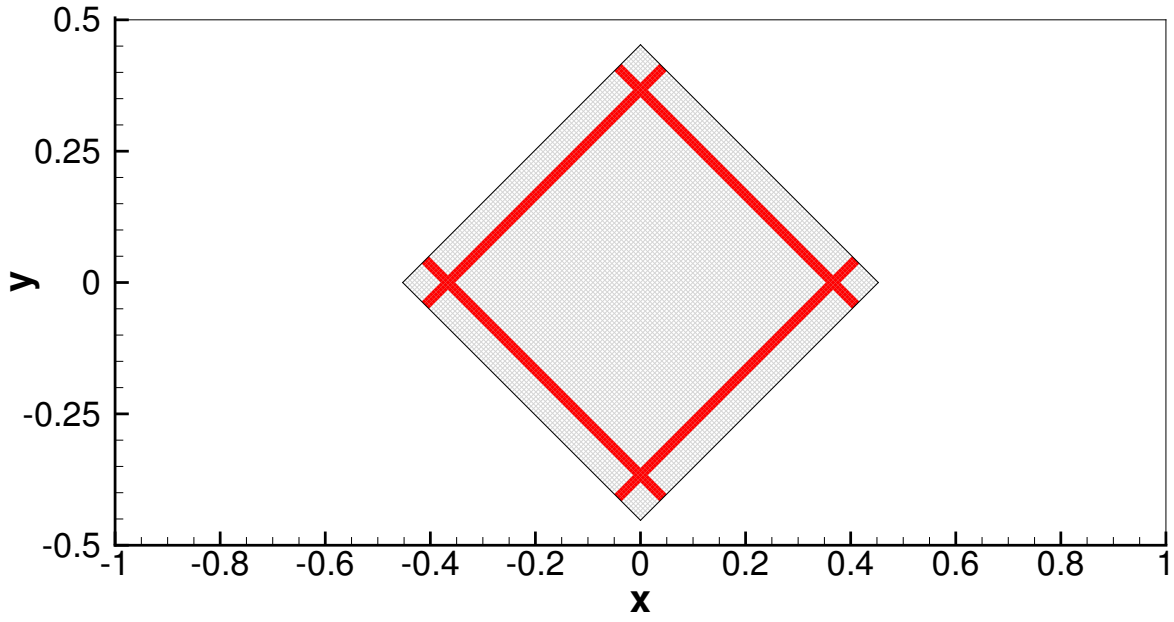

(b)

Figure C.1: Red bands denote the grid points where dissipation is added. (a) Base grid, (b) Patch grid.

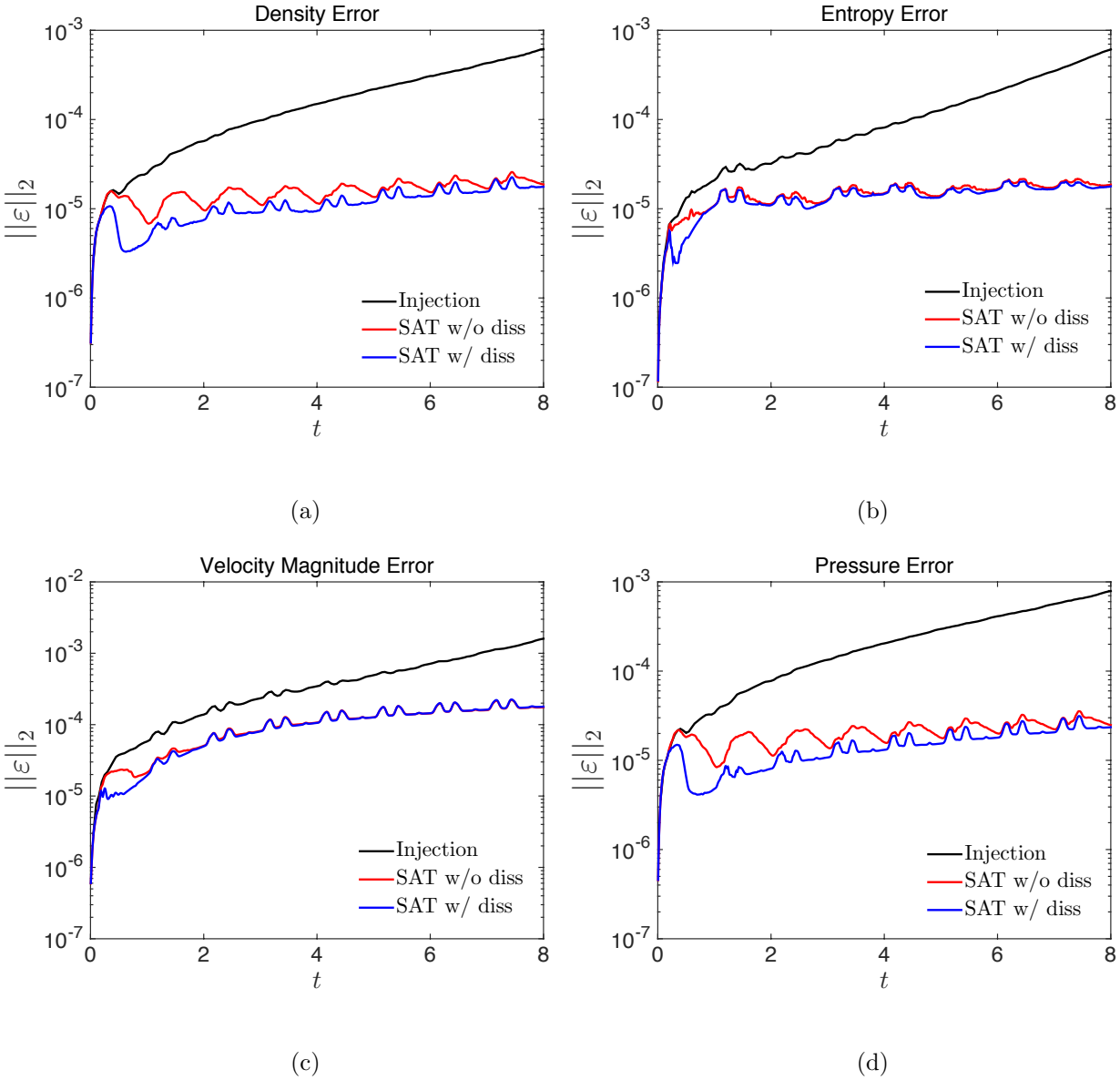

Figure C.2: Error comparison of the injection method against the SAT method with and without dissipation for $u_0 = 2.0$. (a) Density error, (b) Entropy error, (c) Velocity magnitude error, (d) Pressure error.

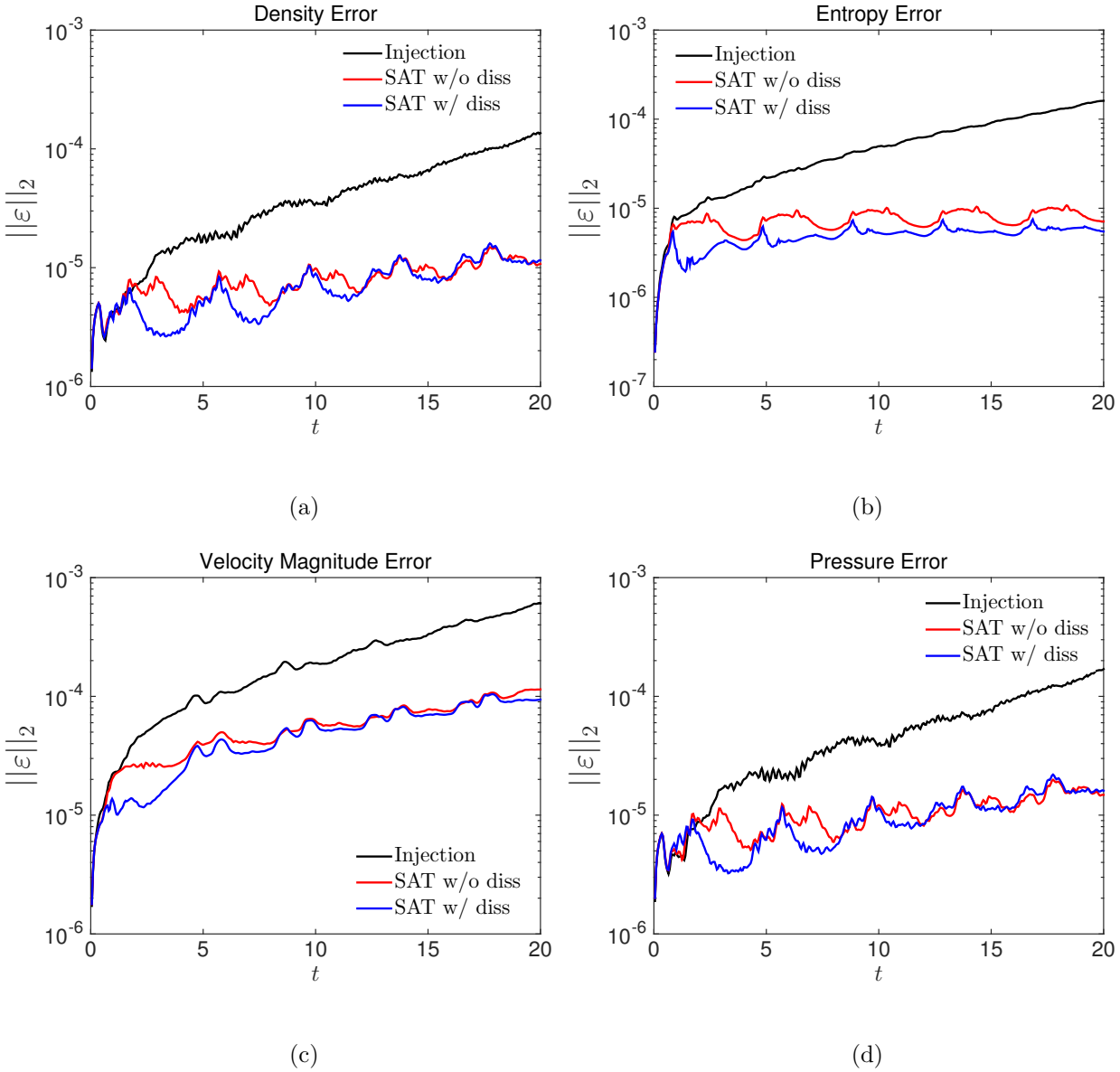

Figure C.3: Error comparison of the injection method against the SAT method with and without dissipation for $u_0 = 0.5$. (a) Density error, (b) Entropy error, (c) Velocity magnitude error, (d) Pressure error.

References

Abarbanel, Saul & Gottlieb, David 1981 Optimal time splitting for two-and three-dimensional navier-stokes equations with mixed derivatives. *Journal of Computational Physics* **41** (1), 1–33.

Abarbanel, Saul S & Chertock, Alina E 2000 Strict stability of high-order compact implicit finite-difference schemes: the role of boundary conditions for hyperbolic pdes, i. *Journal of Computational Physics* **160** (1), 42–66.

Abarbanel, Saul S, Chertock, Alina E & Yefet, Amir 2000 Strict stability of high-order compact implicit finite-difference schemes: the role of boundary conditions for hyperbolic pdes, ii. *Journal of Computational Physics* **160** (1), 67–87.

Antsaklis, Panos J & Michel, Anthony N 2006 *Linear systems*. Springer Science & Business Media.

Antsaklis, Panos J. & Michel, Anthony N. 2007 *A Linear Systems Primer*, 1st edn. Birkhäuser Basel.

Bell, James H, Heineck, James T, Zilliac, Gregory, Mehta, Rabindra D & Long, Kurtis R 2012 Surface and flow field measurements on the faith hill model. *AIAA paper* **704**, 2012.

Benek, J., Buning, P. & Steger, J. 1985 *A 3-D chimera grid embedding technique*. American Institute of Aeronautics and Astronautics.

Berger, Marsha J 1987 On conservation at grid interfaces. *SIAM Journal on Numerical Analysis* **24** (5), 967–984.

Berger, Marsha J & Colella, Phillip 1989 Local adaptive mesh refinement for shock hydrodynamics. *Journal of computational Physics* **82** (1), 64–84.

Bodony, Daniel J, Zagaris, George, Reichert, Adam & Zhang, Qi 2011 Provably stable overset grid methods for computational aeroacoustics. *Journal of Sound and Vibration* **330** (17), 4161–4179.

Brown, David L, Chesshire, Geoff & Henshaw, WD 1989 Getting started with cmpgrd, introductory user's guide and reference manual. *Report LA-UR-89-1294* .

Butcher, John C 2008 *Numerical methods for ordinary differential equations*. John Wiley & Sons.

Carpenter, Mark H, Gottlieb, David & Abarbanel, Saul 1993 The stability of numerical boundary treatments for compact high-order finite-difference schemes. *Journal of Computational Physics* **108** (2), 272–295.

Carpenter, Mark H, Gottlieb, David & Abarbanel, Saul 1994 Time-stable boundary conditions for finite-difference schemes solving hyperbolic systems: methodology and application to high-order compact schemes. *Journal of Computational Physics* **111** (2), 220–236.

Carpenter, Mark H, Nordström, Jan & Gottlieb, David 1999 A stable and conservative interface treatment of arbitrary spatial accuracy. *Journal of Computational Physics* **148** (2), 341–365.

Carpenter, Mark H, Nordström, Jan & Gottlieb, David 2010 Revisiting and extending interface penalties for multi-domain summation-by-parts operators. *Journal of Scientific Computing* **45** (1-3), 118–150.

Chesshire, G & Henshaw, WD 1994 A scheme for conservative interpolation on overlapping grids. *SIAM Journal on Scientific Computing* **15** (4), 819–845.

Chesshire, G & Henshaw, William D 1990 Composite overlapping meshes for the solution of partial differential equations. *Journal of Computational Physics* **90** (1), 1–64.

Cook, Andrew W & Cabot, William H 2004 A high-wavenumber viscosity for high-resolution numerical methods. *Journal of Computational Physics* **195** (2), 594–601.

Corless, Martin J & Frazho, Art 2003 *Linear systems and control: an operator perspective*. CRC Press.

Courant, Richard, Friedrichs, Kurt & Lewy, Hans 1928 Über die partiellen differenzengleichungen der mathematischen physik. *Mathematische Annalen* **100** (1), 32–74.

Flores, Jolen & Chaderjian, Neal M 1990 Zonal navier-stokes methodology for flow simulation about a complete aircraft. *Journal of Aircraft* **27** (7), 583–590.

Godunov, Sergei Konstantinovich & Ryabenkii, Viktor Solomonovich 1963 Spectral stability criteria for boundary-value problems for non-self-adjoint difference equations. *Russian Mathematical Surveys* **18** (3), 1–12.

Goldberg, Moshe & Tadmor, Eitan 1978 Scheme-independent stability criteria for difference approximations of hyperbolic initial-boundary value problems. i. *Mathematics of Computation* **32** (144), 1097–1107.

Goldberg, Moshe & Tadmor, Eitan 1981 Scheme-independent stability criteria for difference approximations of hyperbolic initial-boundary value problems. ii. *mathematics of computation* **36** (154), 603–626.

Goldberg, Moshe & Tadmor, Eitan 1985 Convenient stability criteria for difference approximations of hyperbolic initial-boundary value problems. *Mathematics of computation* **44** (170), 361–377.

Goldberg, Moshe & Tadmor, Eitan 1987 Convenient stability criteria for difference approximations of hyperbolic initial-boundary value problems. ii. *Mathematics of computation* **48** (178), 503–520.

Gustafsson, Bertil 1975 The convergence rate for difference approximations to mixed initial boundary value problems. *Mathematics of Computation* **29** (130), 396–406.

Gustafsson, Bertil 2001 The Godunov-Ryabenkii condition: The beginning of a new stability theory. In *Godunov Methods* (ed. E.F. Toro), pp. 425–443. Springer US.

Gustafsson, Bertil 2007 *High order difference methods for time dependent PDE*, , vol. 38. Springer Science & Business Media.

Gustafsson, Bertil, Kreiss, Heinz-Otto & Oliger, Joseph 1995 *Time dependent problems and difference methods*. John Wiley & Sons.

Gustafsson, Bertil, Kreiss, Heinz-Otto & Sundström, Arne 1972 Stability theory of difference approximations for mixed initial boundary value problems. ii. *Mathematics of Computation* pp. 649–686.

Heath, Michael T 2001 *Scientific computing*. McGraw-Hill.

Henshaw, William D 2006 A high-order accurate parallel solver for maxwell's equations on overlapping grids. *SIAM Journal on Scientific Computing* **28** (5), 1730–1765.

Henshaw, William D & Chand, Kyle K 2009 A composite grid solver for conjugate heat transfer in fluid-structure systems. *Journal of Computational Physics* **228** (10), 3708–3741.

Hicken, Jason E & Zingg, David W 2013 Summation-by-parts operators and high-order quadrature. *Journal of Computational and Applied Mathematics* **237** (1), 111–125.

Kim, Jeonglae 2012 Adjoint-based control of turbulent jet noise. PhD thesis, University of Illinois at Urbana-Champaign.

Kim, Jeonglae, Bodony, Daniel J & Freund, Jonathan B 2010 A high-order, overset-mesh algorithm for adjoint-based optimization for aeroacoustics control. *AIAA Paper* **3818**, 7–9.

Kramer, RMJ, Pantano, C & Pullin, DI 2009 Nondissipative and energy-stable high-order finite-difference interface schemes for 2-d patch-refined grids. *Journal of Computational Physics* **228** (14), 5280–5297.

Kreiss, Heinz-Otto 1963 Über implizite differenzmethoden für partielle differentialgleichungen. *Numerische Mathematik* **5** (1), 24–47.

Kreiss, Heinz-Otto & Scherer, Godela 1974 Finite element and finite difference methods for hyperbolic partial differential equations (33), 195–212.

Lax, Peter & Wendroff, Burton 1960 Systems of conservation laws. *Communications on Pure and Applied mathematics* **13** (2), 217–237.

Lax, Peter D 1973 *Hyperbolic systems of conservation laws and the mathematical theory of shock waves*, , vol. 11. SIAM.

Lax, Peter D & Richtmyer, Robert D 1956 Survey of the stability of linear finite difference equations. *Communications on Pure and Applied Mathematics* **9** (2), 267–293.

Levy, Doron & Tadmor, Eitan 1998 From semidiscrete to fully discrete: Stability of runge–kutta schemes by the energy method. *SIAM review* **40** (1), 40–73.

Lilly, Douglas K 1992 A proposed modification of the germano subgrid-scale closure method. *Physics of Fluids A: Fluid Dynamics (1989-1993)* **4** (3), 633–635.

Magnus, R & Yoshihara, Hideo 1970 Inviscid transonic flow over airfoils. *AIAA Journal* **8** (12), 2157–2162.

Mattsson, Ken & Nordström, Jan 2004 Summation by parts operators for finite difference approximations of second derivatives. *Journal of Computational Physics* **199** (2), 503–540.

Meakin, Robert L 1991 A new method for establishing intergrid communication among systems of overset grids. *AIAA paper* **1586**, 1991.

Moin, Parviz, Squires, Kyle, Cabot, W & Lee, Sangsan 1991 A dynamic subgrid-scale model for compressible turbulence and scalar transport. *Physics of Fluids A: Fluid Dynamics (1989-1993)* **3** (11), 2746–2757.

Nordström, Jan & Carpenter, Mark H 1999 Boundary and interface conditions for high-order finite-difference methods applied to the euler and navier–stokes equations. *Journal of Computational Physics* **148** (2), 621–645.

Nordström, Jan, Gong, Jing, Van der Weide, Edwin & Svärd, Magnus 2009 A stable and conservative high order multi-block method for the compressible navier–stokes equations. *Journal of Computational Physics* **228** (24), 9020–9035.

Petersson, N Anders 1999*a* An algorithm for assembling overlapping grid systems. *SIAM Journal on Scientific Computing* **20** (6), 1995–2022.

Petersson, N Anders 1999*b* Hole-cutting for three-dimensional overlapping grids. *SIAM Journal on Scientific Computing* **21** (2), 646–665.

Pirozzoli, Sergio 2011 Stabilized non-dissipative approximations of euler equations in generalized curvilinear coordinates. *Journal of Computational Physics* **230** (8), 2997–3014.

Prewitt, Nathan C, Belk, Davy M & Shyy, Wei 2000 Parallel computing of overset grids for aerodynamic problems with moving objects. *Progress in Aerospace Sciences* **36** (2), 117–172.

Pulliam, Thomas H & Chaussee, DS 1981 A diagonal form of an implicit approximate-factorization algorithm. *Journal of Computational Physics* **39** (2), 347–363.

Rai, Man Mohan 1986 A conservative treatment of zonal boundaries for euler equation calculations. *Journal of Computational Physics* **62** (2), 472–503.

Rai, Man Mohan 1987 Navier-stokes simulations of rotor/stator interaction using patched and overlaid grids. *Journal of Propulsion and Power* **3** (5), 387–396.

Reichert, Adam, Heath, Michael T & Bodony, Daniel J 2012 Energy stable numerical methods for hyperbolic partial differential equations using overlapping domain decomposition. *Journal of Computational Physics* **231** (16), 5243–5265.

Richtmyer, Robert D & Morton, Keith W 1994 Difference methods for initial-value problems. *Malabar, Fla.: Krieger Publishing Co.,— c1994, 2nd ed.* **1**.

Rizzi, Arthur, Eliasson, Peter, Lindblad, Ingemar, Hirsch, Charles, Lacor, Chris & Haeuser, Jochem 1993 The engineering of multiblock/multigrid software for navier-stokes flows on structured meshes. *Computers and Fluids* **22** (23), 341 – 367.

Rogers, Stuart E, Suhs, Norman E & Dietz, William E 2003 Pegasus 5: an automated preprocessor for overset-grid computational fluid dynamics. *AIAA journal* **41** (6), 1037–1045.

Sengupta, Tapan K, Suman, VK & Singh, Neelu 2010 Solving navier–stokes equation for flow past cylinders using single-block structured and overset grids. *Journal of Computational Physics* **229** (1), 178–199.

Sharan, Nek & Bodony, Daniel J 2013 High-order provably stable overset grid methods for block-structured adaptive mesh refinement. In *21st AIAA Computational Fluid Dynamics Conference*, p. 2872.

Sherer, Scott E & Scott, James N 2005 High-order compact finite-difference methods on general overset grids. *Journal of Computational Physics* **210** (2), 459–496.

Steger, Joseph L & Benek, John A 1987 On the use of composite grid schemes in computational aerodynamics. *Computer Methods in Applied Mechanics and Engineering* **64** (1), 301–320.

Strand, B. 1994 Summation by parts for finite difference approximations for d/dx. *Journal of Computational Physics* **110** (1), 47–67.

Strang, G. 1964 Accurate partial difference methods. ii. non-linear problems. *Numerische Mathematik* **6**, 37–46.

Strikwerda, John C 1980 Initial boundary value problems for the method of lines. *Journal of Computational Physics* **34** (1), 94–107.

Strikwerda, John C 2004 *Finite difference schemes and partial differential equations*. SIAM.

Suhs, NE & Tramel, RW 1991 Pegsus 4.0 user's manual. *Tech. Rep.*. DTIC Document.

Svärd, M. 2004 On coordinate transformations for summation-by-parts operators. *J. Sci. Comput.* **20** (1), 29–42.

Svärd, Magnus, Carpenter, Mark H & Nordström, Jan 2007 A stable high-order finite difference scheme for the compressible navier–stokes equations, far-field boundary conditions. *Journal of Computational Physics* **225** (1), 1020–1038.

Tam, Christopher KW & Hardin, JC 1997 Second computational aeroacoustics (caa) workshop on benchmark problems .

Tam, Christopher KW & Hu, Fang Q 2004 An optimized multi-dimensional interpolation scheme for computational aeroacoustics applications using overset grids. *AIAA paper* **2812**, 2004.

Trefethen, Lloyd N 1985 Stability of finite-difference models containing two boundaries or interfaces. *Mathematics of computation* **45** (172), 279–300.

Visbal, Miguel R & Gaitonde, Datta V 2002 On the use of higher-order finite-difference schemes on curvilinear and deforming meshes. *Journal of Computational Physics* **181** (1), 155–185.

Wang, ZJ 1995 A fully conservative interface algorithm for overlapped grids. *Journal of Computational Physics* **122** (1), 96–106.

Wang, ZJ, Parthasarathy, V & Hariharan, N 2000 A fully automated chimera methodology for multiple moving body problems. *International Journal for Numerical Methods in Fluids* **33** (7), 919–938.